

## APPROVAL SHEET

Title of Dissertation: Bioprocess Analysis Sensor System for Real-Time Monitoring of 'In-Vitro'  
Protein Production Variables

Name of Candidate: Neha Ravindra Sardesai  
Doctor of Philosophy, 2016

Dissertation and Abstract Approved: \_\_\_\_\_

Dr. Yordan Kostov, PhD  
Research Professor  
Computer Science and Electrical Engineering Department,  
Department of Chemical, Biochemical, and Environmental  
Engineering

Dissertation and Abstract Approved: \_\_\_\_\_

Dr. Joel M. Morris, PhD  
Professor Emeritus of Electrical Engineering  
Computer Science and Electrical Engineering Department

Date Approved: \_\_\_\_\_

## ABSTRACT

Title of Document: BIOPROCESS ANALYSIS SENSOR SYSTEM  
FOR REAL-TIME MONITORING OF ‘IN-  
VITRO’ PROTEIN PRODUCTION  
VARIABLES

Neha Ravindra Sardesai, Ph.D., 2016

Directed By: Yordan Kostov, PhD  
Research Professor  
Computer Science and Electrical Engineering  
Department

Joel M. Morris, PhD  
Professor Emeritus of Electrical Engineering  
Computer Science and Electrical Engineering  
Department

Real-time monitoring of bioprocesses enables one to track changes and correct abnormalities. Multiple arrangements for the apparatus of such bioprocesses has led to the need of universal, portable, versatile, real-time bioprocess monitoring systems. This dissertation presents a new class of opto-electronic transducers that can be used to measure multiple bioprocess variables without the need to switch the optics or hardware. This allows flexibility closer to the lab-grade devices with compact size similar to a dedicated sensor. The versatile instrumentation of the sensor system is capable of seamlessly switching between pH, Dissolved Oxygen (DO), and Green Fluorescent Protein (GFP) measurement modes, and is capable of auto recognition of the sensor type.

The pH and DO were measured using optical chemical sensors that were interrogated using the specialized opto-electronic transducer. A software visual interface was developed for control and data logging for the bioprocess analysis sensor system measurements. The principle of ratiometric fluorescence was used for pH measurements, and that of fluorescence-lifetime for DO measurements. Fluorescent emissions as a result of blue excitations were directly measured in the case of GFP. GFP is intended to be used as a biomarker for real-time monitoring of target protein production. A fixed-length extension for the optical fiber electrode (optrode) of the opto-electronic transducer was modeled and implemented to rectify anomalies in signal due to movement of optrode in a GFP bioprocess. GFP measurements were further analyzed by observing rate of change of protein expression/generation. Expression and rate signals were processed in real-time and post-processed using digital filters. The bioprocess analysis sensor system was used to monitor protein purification as well.

The instrumentation of the sensor system, when modified by replacing the excitation LEDs and photodiode, was used to measure UV absorbance for quantification of proteins. Quantum dots were used to convert UV light to red light, thus enabling UV absorbance detection with the visible range photodiode already present on the sensor. A comparative study was conducted to evaluate the UV absorbance sensor and quantum dot sensor.

The developed system constitutes common instrumentation for measuring either pH, DO, GFP, or UV absorbance. It has been tested in actual bioprocesses and protein production processes to assess the measurement accuracy of each variable, and has been found acceptable for continuous bioprocess monitoring.

BIOPROCESS ANALYSIS SENSOR SYSTEM FOR REAL-TIME MONITORING OF 'IN-VITRO' PROTEIN PRODUCTION VARIABLES

By

Neha Ravindra Sardesai

Dissertation submitted to the Faculty of the Graduate School of the  
University of Maryland, Baltimore County, in partial fulfillment  
of the requirements for the degree of  
Doctor of Philosophy

2016

© Copyright by  
Neha Ravindra Sardesai  
2016



*Dedicated to my Mother and Father,*  
*&*  
*In loving memory of my sister Ruta (1995-2013)*

## Acknowledgements

I would like to express my gratitude and sincere thanks to my advisors, Dr. Yordan Kostov and Dr. Joel Morris. Dr. Kostov, I thank, for his patience, support, and guidance through my years of research at UMBC. I am grateful to Dr. Morris for his constant encouragement and advice on both, the professional and personal front. I'd like to thank Dr. Govind Rao for his kind words and motivation. I thank Dr. Fow-Sen Choa and Dr. Ian White for taking the time off their busy schedules and being a part of my committee.

I thank all the members of the CAST lab, specifically the system design team. Thank you Mustafa, thank you for being such a good, honest, and supportive friend. Dagmawi and Brandon, for all the fun times, and encouragement when I was disheartened. Thank you Kanika for being my best friend and being there. Apoorva for being the silent supporter. Chirag and Pankaj for their words of encouragement. I appreciate the faith that you had in me.

My deepest thanks to Arnav Joshi, for playing the role of my better half, friend, philosopher, and guide. I am grateful to my parents for making me the woman I am today. Their effort and sacrifices have been instrumental in my success today.

Finally, I would like to thank my sister, Ruta. She was, is, and will continue to be the silent wind that guides me through life.



# Table of Contents

Table of Contents .....	xii
List of Tables .....	xv
List of Figures .....	xvi
Chapter 1. INTRODUCTION .....	1
1.1 Motivation .....	4
1.2 Research Contribution .....	7
1.3 Chapter Organization .....	9
Chapter 2. THEORETICAL DESCRIPTION OF SENSOR MECHANISM .....	11
2.1 Fluorescence .....	12
2.2 Chemical Patch Sensor .....	13
• pH patch .....	13
• Dissolved Oxygen (DO) patch .....	14
• Instrumentation transfer functions .....	14
• Standardization of optoelectronics .....	17
2.3 Absorbance Sensor .....	18
• Absorbance .....	18
• Quantum Dots (QDs) .....	18
2.4 Summary .....	19
Chapter 3. INSTRUMENTATION DESIGN FOR BIO-PROCESS ANALYSIS SENSOR SYSTEM (BASS) .....	20
3.1 Hardware Design for Fluorescence Sensor .....	20
• Chemical Patch Sensor .....	22
• Optics .....	23
• Electronics .....	24
3.2 Hardware Design for Absorbance-based Sensor System .....	28
• UV absorbance sensor .....	28
• Dual channel system for comparison between UV and QD system .....	29
• Preparation of QD – Si-photodiode UV detector .....	30
3.3 Firmware Design for Bioprocess Analysis Sensor System .....	32
3.4 Software Design for Bioprocess Analysis Sensor System .....	33
• Calibration Visual Interface .....	34
• System Interpretation and Data Logging (SIDL) User Interface .....	36
3.5 Summary .....	39
Chapter 4. TESTING AND VALIDATION FOR PH AND DISSOLVED OXYGEN .....	40

4.1 Apparatus Arrangement .....	41
4.2 Calibration.....	42
• pH calibration.....	42
• DO calibration.....	43
4.3 Calibration Verification and Statistics .....	46
• pH calibration verification and statistics.....	46
• DO calibration verification and statistics.....	48
4.4 Standardization of Bioprocess Analysis Sensor System.....	50
• pH standardization .....	50
• DO standardization .....	54
4.5 Temperature Coefficient for DO Measurement.....	56
4.6 E. Coli Experiment.....	59
4.7 Bioreactor Lysate Run using BASS to Measure pH And DO .....	61
4.8 Summary .....	63
Chapter 5. TESTING AND VALIDATION FOR GREEN FLUORESCENT PROTEIN (GFP).....	64
5.1 Calibration and Verification of GFP Sensor .....	65
• Calibration.....	65
• Setting up the GFP IVT (In-Vitro Translation) reaction: .....	68
• Calibration Verification .....	68
5.2 GFP Fixed Length Extension (GFP-FLE) .....	71
• Theoretical modelling of GFP-FLE .....	73
• Practical implementation of GFP-FLE .....	80
5.3 Filtered Rate Analysis (FRA) .....	82
• Online (real-time processing) FRA.....	83
• Offline (post-processing) FRA .....	86
5.4 Use of GFP Sensor in Purification Process.....	93
5.5 Summary .....	97
Chapter 6. UV ABSORBANCE SENSOR SYSTEM .....	98
6.1 UV Absorbance Sensor.....	99
6.2 Comparative Analysis of QD Sensor and UV Sensor .....	102
6.3 Summary .....	106
Chapter 7. CONCLUSION .....	107
7.1 Summary .....	107
7.2 Conclusions.....	109
7.3 Future Work .....	111
APPENDIX A. BIOLOGICALLY DERIVED MEDICINES ON DEMAND (Bio-MOD) .....	112
A.1 Cell-free protein expression .....	113
A.2 Protein Purification .....	115
APPENDIX B. SENSOR HARDWARE DESIGN .....	116

B.1 Micro-controller Functions .....	116
B.2 Beam Combiner.....	116
B.3 Board Schematics .....	117
B.4 Patch Sleeve .....	118
APPENDIX C. SENSOR SOFTWARE CODE .....	119
C.1 Calibrate Visual Interface.....	119
C.2 System Interpretation and Data Logging Software (SIDL) .....	122
APPENDIX D. MATLAB CODE FOR GFP DATA PROCESSING .....	127
Chapter 8. BIBLIOGRAPHY .....	132

## List of Tables

Table 4.1: Flowmeter adjustments for DO calibration .....	44
Table 4.2: Table showing calculation for DO calibration.....	44
Table 4.3: Calibrations for each pH patch with each optrode.....	47
Table 4.4: Calibrations before and after autoclaving pH patch sensor .....	48
Table 4.5: Calibrations for each DO patch with each optrode.....	50
Table 4.6: Yield of EPO in each bioreactor .....	62
Table 6.1: Percentage nucleic acid contamination in protein [44].....	98
Table 6.2: 260 nm:280 nm ratio for serially diluted BSA samples using spectrophotometer and AB1 UV sensor .....	101
Table B.1: Micro-controller functions and the hexadecimal values associated with them .....	116

## List of Figures

Figure 1.1: pH microelectrode response in lysate: the green and orange profiles represent pH microelectrodes for continuous sample measurement in lysate, the blue profile represents periodic sample measurements every 15 minutes in lysate .....	5
Figure 2.1: Jablonski diagram illustrating the concept of fluorescence.....	12
Figure 3.1: Diagram of single channel fluorescence sensor .....	21
Figure 3.2: Image of dual channel optical sensor .....	21
Figure 3.3: Excitation and emission light directionality. <b>Left:</b> Through-space directional patch illumination produces omnidirectional emission. Optical shield prevents excitation and emission passing through patch. The arrangement allows only for close-up placement of chemical patch, as the amount of light reaching the detector depends on the distance. <b>Middle:</b> immobilization of the optical indicator in the patch. <b>Right:</b> Positioning the patch on the tip of a fiber captures all the emission that is within the acceptance cone regardless of the length of the fiber [2].....	22
Figure 3.4: Patch sleeve design.....	23
Figure 3.5: Beam combiner/splitter setup .....	24
Figure 3.6: Block diagram for the electronics, DTA differential transimpedance amplifier, DIA differential inverting amplifier, DLIA differential lock-in amplifier, B blue LED, V violet LED, S sensor optics and chemistry, VCCS voltage controlled current source, SOC system-on-a-chip .	25
Figure 3.7: LED driver.....	26
Figure 3.8: Synchronous rectifier .....	27
Figure 3.9: Schematics of UV absorbance sensor .....	28
Figure 3.10: Schematics of UV quantum dots sensor.....	29
Figure 3.11: Illustration of construction of QD plate .....	31
Figure 3.12: Image of QD and UV absorbance sensor .....	31
Figure 3.13: Flowchart describing the working of the calibration user interface .....	34
Figure 3.14: Screenshot of calibrate tab of calibration user interface .....	35
Figure 3.15: Screenshot of results tab of calibration user interface.....	35
Figure 3.16: (a) Flowchart describing the working of the system interpretation and data logging user interface in brief, (b) Flowchart describing chemical patch type calculation .....	37
Figure 3.17: Screenshot of System interpretation and data logging user interface, (a) Actions tab, (b) Calibrated Signal Plot tab.....	38
Figure 4.1: (a) The complete optoelectronic system with chemical sensors measuring in a flask (b) The visual interface measuring pH and DO in the flask. The visual interface measuring pH and DO in the flask .....	41
Figure 4.2: pH calibration .....	43
Figure 4.3: DO calibration .....	45
Figure 4.4: pH calibration verification.....	46
Figure 4.5: DO calibration verification.....	49
Figure 4.6: Emission spectra of a dye when excited with spectrally narrowed lamp or LED.....	52
Figure 4.7: Standardization of pH patch for sensors 1a, 1b, 2a, 2b, 3a. Dotted lines represent confidence interval for $\pm 3\sigma$ error .....	53
Figure 4.8: Standardization of DO patch for sensors 1a, 1b, 2a, 2b, 3a. Dotted lines represent confidence interval for $\pm 3\sigma$ error .....	55

Figure 4.9: Plot for DO patch w1 on channel 1 of sensor A1 .....	56
Figure 4.10: Plot for DO patch p2 on channel 1 of sensor A1 .....	57
Figure 4.11: Plot for DO patch w1 on channel 2 of sensor A1 .....	57
Figure 4.12: Plot for DO patch p2 on channel 2 of sensor A1 .....	58
Figure 4.13: pH and DO profiles for E. Coli over 25 hours .....	59
Figure 4.14: Bioreactor setup for run 382k14 .....	61
Figure 4.15: pH and DO profiles for bioreactor run 382k14 .....	62
Figure 5.1: Arrangement of standard samples in 96 well plate with concentrations .....	66
Figure 5.2: Setup for calibration of optical sensor and for actual GFP run .....	66
Figure 5.3: Calibration for Spectromax .....	67
Figure 5.4: Calibration for GFP sensors A21 and A22 .....	67
Figure 5.5: Real-time GFP expression in Spectromax .....	69
Figure 5.6: Real-time GFP expression in GFP optical sensor .....	70
Figure 5.7: Use of GFP sensor by submerging optrode in GFP sample .....	71
Figure 5.8: Anomaly in measurement due to variation in depth at which optrode is submerged .....	72
Figure 5.9: GFP-FLE design .....	73
Figure 5.10: Fluorescent emission for one GFP molecule .....	74
Figure 5.11: Excitation and emission profiles for one GFP molecule at varying length along optrode .....	75
Figure 5.12: Front and side view of slicing method .....	76
Figure 5.13: Mathematical illustration for slice 1 of acceptance cone .....	77
Figure 5.14: Emissions along radius along positive Y axis for $n$ slices; $n = 10$ , $L = 0.1$ mm, $r = 1$ mm, $C = 0.5\mu\text{g}/\mu\text{l}$ .....	78
Figure 5.15: Total emission along the diameter for $n$ slices, $n = 10$ , $r = 1$ mm, $l = 1$ mm, $C = 0.5\mu\text{g}/\mu\text{l}$ .....	79
Figure 5.16: Maximum emission intensity for varying lengths .....	79
Figure 5.17: Comparison of theoretical and practical values for GFP-FLE .....	80
Figure 5.18: Comparison of data recorded when using and not using FLE .....	81
Figure 5.19: Ideal GFP expression data and corresponding rate data .....	82
Figure 5.20: Block diagram of real-time rate analysis in GFP optical sensor .....	83
Figure 5.21: Ideal rate and rate after real-time rate analysis of ideal GFP expression data .....	84
Figure 5.22: Real-time GFP expression and rate data from GFP optical sensor .....	85
Figure 5.23: Frequency Response of ideal GFP expression data .....	86
Figure 5.24: Time delay introduced in ideal signal due to use of Butterworth filter .....	87
Figure 5.25: Ideal GFP expression and rate profiles after using Butterworth filter .....	88
Figure 5.26: (a) Time delay introduced in ideal signal due to Hamming window, (b) Ideal GFP expression and rate data after filtering with Hamming window .....	89
Figure 5.27: Frequency response of GFP expression data from optical sensor .....	90
Figure 5.28: Delay introduced due to use of IIR Butterworth filter .....	91
Figure 5.29: Filtered and delay corrected expression plot using Butterworth filter and corresponding rate plot .....	91
Figure 5.30: Filtered and delay corrected expression plot using Hamming window and corresponding rate plot .....	92
Figure 5.31: Block diagram illustrating purification automation .....	93

Figure 5.32: Ideal profiles of GFP before loading on column and after elution.....	94
Figure 5.33: Purification data collected from GFP optical sensor.....	95
Figure 5.34: Purification data collected from GFP optical sensor, area before column = 3.93, area after column = 2.5 .....	96
Figure 6.1: Correlation for UV absorbance at 260nm for AB1 and spectrophotometer.....	100
Figure 6.2: Correlation for UV absorbance at 280nm for AB1 and spectrophotometer.....	100
Figure 6.3: Absorbance of BSA as measured on lab-grade spectrophotometer, and UV photodiode, QD-Si-photodiode equipped sensors (standard deviation data shown in text below). .....	103
Figure 6.4: Calibration of raw voltage data of BSA as measured on QD sensor .....	104
Figure 6.5: Aging data for both, QD and UV sensors .....	105
Figure A.1: Illustration of Bio-MOD in a suitcase [8].....	112
Figure A.2: Transcription and translation resulting in protein expression .....	113
Figure A.3: Illustration of cell-free protein expression [45].....	114
Figure A.4: Procedure for affinity chromatography .....	115

## Chapter 1. INTRODUCTION

Real-time monitoring for bioprocesses is an essential tool for research in biochemical engineering and biotechnology. It determines progress of the tested (bio) chemical processes and has the ability to pick out any abnormalities within such processes, thus enabling control over the process progress. This real-time monitoring is accomplished using a Bioprocess Analysis Sensor System (BASS), which is used to oversee the actual process in real-time by measuring pre-defined bioprocess variables.

A bioprocess analysis sensor system (BASS) needs to be portable and flexible to be able to monitor bioprocesses that are conducted and realized in multiple settings [1], [2], [3], [4], [5], [6]. It needs to be versatile to measure multiple variables simultaneously and selectively, so that the variables are distinguishable. It needs to be user-friendly and should have a minimal learning curve [2], [6], [7]. This dissertation presents a bioprocess analysis sensor system (BASS) that is portable, flexible, versatile, selective, and user-friendly for use in multiple types of bioprocesses.

The instrumentation for BASS was developed as a process analysis tool for monitoring and measurement of in-vitro<sup>1</sup> protein production. The Center for Advanced Sensor Technology (CAST) laboratory at the University of Maryland, Baltimore County (UMBC) is developing an innovative mammalian in-vitro protein expression<sup>2</sup> and protein purification<sup>3</sup> technology for developing therapeutic protein-based pharmaceutical drugs on-site. This project is called ‘Biologically Derived Medicines On-Demand’ or Bio-MOD, and is funded by DARPA. This technology would reduce the biotechnology industry’s footprint to the size of a small laptop computer carried in a backpack/suitcase, housing all the elements necessary to express, purify, and analyze any target protein [8].

---

<sup>1</sup> In-vitro: outside usual biological surrounding, outside living body and in artificial environment

<sup>2</sup> Protein expression: Cellular mechanism that generates therapeutic proteins as an end product, also called cell-free protein expression

<sup>3</sup> Protein purification: Separation of proteins from the non-protein debris in the protein expression product



In-vitro production of biopharmaceuticals is currently not mainstream, therefore, no in-vitro bioprocesses have been approved by the FDA (Food and Drug Administration) as of yet [9]. Bio-MOD targets the development of such a method for production of medical grade biopharmaceuticals. However, every bioprocess needs to have an associated process analytical technique (PAT) [6], [10], [11]. For the portable system format CAST is targeting, there are no defined PATs. Therefore, BASS will serve as a PAT for in-vitro bioprocesses for mobile manufacturing of pharmaceuticals. **This dissertation discusses the research, design, development, and validation of an optoelectronic Bioprocess Analysis Sensor System (BASS) that will serve as a measurement/process-analysis device for multiple process variables. The system would be portable, flexible, versatile, selective, and user-friendly for use in multiple types of bioprocesses.** Development of BASS is intended for, but not specific to, the Bio-MOD system.

The functionality of BASS is based on the processes of fluorescence and absorbance. Chemical patch sensors, an opto-electronic transducer, and the software-based graphic user interface and control system are implemented to realize fluorescence/absorbance and capture an optimal signal to represent the parameter being measured [5], [12]. The parameters measured need to characterize the bioprocess such that the bioprocess is easy to interpret. To ensure optimal biological conditions for maximum yield of protein in Bio-MOD, the bioprocess is monitored via specific variables. The pH and dissolved oxygen (DO) concentration are the most commonly measured variables during bioprocesses [13]. pH is monitored to determine acidity/basicity of the process. Dissolved oxygen (DO) concentration is monitored to track oxidation in the protein expression.

Biomarkers<sup>4</sup> can be used in Bio-MOD to track the entire protein production in real-time [14]. Often, these bio-markers are fluorescent proteins (i.e., Green fluorescent Proteins (GFP) in this case), and are attached to the target protein as an indicator to track production [14]. BASS was

---

<sup>4</sup> Biomarkers: In this case, a biomarker is a fluorescent protein that is attached to the target protein. The protein tag is generated along with the target protein, and stays associated with it. Due to its fluorescent nature, it is possible to track the generation of the target protein.

Refer to APPENDIX A. for further details on protein expression and purification techniques

modified to measure GFP for real-time tracking and post-process analysis of protein expression and purification<sup>5</sup>.

In an in-vitro protein expression system, the protein is generated in the cell lysate<sup>6</sup>. Due to the presence of miscellaneous cell organelles<sup>7</sup> and other machinery in the medium, this protein product has much lower purity [9], [15]. Thus, purification of this highly impure protein is essential to its conversion to therapeutic-grade purity. Monitoring of GFP, when used as a biomarker, gives visual validation to the purification technique.

Not all proteins expressed in Bio-MOD have a GFP tag. UV absorption is a well-known protein quantitation technique [16]. To generalize this purification supervision method to all proteins, a UV absorbance sensor is currently being developed by modifying the optical component of BASS. This absorption sensor measures UV absorbance of proteins after the purification process.

BASS serves as a process analysis tool to monitor and, ultimately, control in-vitro protein expression and purification. This dissertation discusses the theory, which lays out the foundation for system design, actual design and implementation, and validation of BASS in actual bioprocesses. After extensive research and experimentation, BASS proves to serve as an excellent measurement and control tool for in-vitro protein production, as well as monitoring other bioprocesses. This dissertation will, however, address BASS with respect to the in-vitro protein production system.

---

<sup>5</sup> Protein productions comprises the processes of protein expression and purification

<sup>6</sup> Lysate: fluid containing contents of cells that are broken down/lysed

<sup>7</sup> Organelles: subunit in a cell having specialized function, organelles in a cell are equivalent to organs in body

## 1.1 Motivation

In traditional protein production systems, a variety of bioprocess monitoring tools are available. Microelectrodes, bioassays, western blots, High Performance Liquid Chromatography (HPLC), etc., are examples for the same [17]. However, these tools cannot be used in the Bio-MOD system because each procedure involves using different setups and manual preparations. The Bio-MOD system is a portable setup and, hence, these tools cannot be utilized with it.

Also, it was observed that some of the apparatus was not compatible with the lysate being used. For example, microelectrodes that measured bioprocess variables pH and DO failed to perform in lysate, resulting in a drift in measurements. This happened due to the highly viscous nature of the lysate. As a result, there is a high degree of non-specific adsorption on the electrode (predominantly on the glass electrode) surface, which resulted in continuous drift of the microelectrode readings and, ultimately, failure of the electrodes.

Figure 1.1 illustrates pH microelectrodes failing to respond correctly in the lysate. The orange and green profiles represent continuous measurement by the microelectrodes in the lysate. These were compared with a similar microelectrode used to measure every 15 minutes. To prevent this electrode from clogging and measurements drifting, it was thoroughly cleaned.

Figure 1.1 demonstrates a drop in pH over time for continuous measurements when actually, there is a rise in pH that stabilizes at 7.3 pH for the periodic sample measurement. Hence, the microelectrodes fail to read the pH trend accurately, giving rise to a need for more accurate sensors that do not fail in lysate.

We considered using an optical fluorescence sensor for measuring pH and DO during protein expression (these variables are already well-established in the biotechnology industry) [2], [3], [18]. The optical sensor system measurements are based on fluorescence. Optically-excitabile chemical-sensing patches are used in combination with a tailor-made photometer that is designed specifically to read data from them [5]. For pH measurement, DHDS<sup>8</sup> dye is used that has two excitation wavelengths, one in violet ( $\lambda_1 = 405$  nm) and the other in blue ( $\lambda_2 = 457$  nm) [5]. When excited with these wavelengths, the patch sensors fluoresce green emissions corresponding to the

---

<sup>8</sup> DHDS: 1, 8-dihydroxy-3,6-pyrene disulfonic acid disodium salt

individual excitations and a ratio of these emission intensities is considered for measurement of pH. The ratio results in elimination of the noise contribution to measurements [5]. RuDPP<sup>9</sup> is the dye used in the DO patch sensor. The measurements for DO concentration correspond to the difference in response time for emissions from the chemical patch sensor. The instrumentation of BASS is capable of automatically detecting what type of a patch sensor (pH or DO) will be used and adjusts the detection algorithms accordingly. Thus, a pH and DO optical fluorescence sensor system was researched, designed, implemented, and validated for this dissertation as explained further in this dissertation.

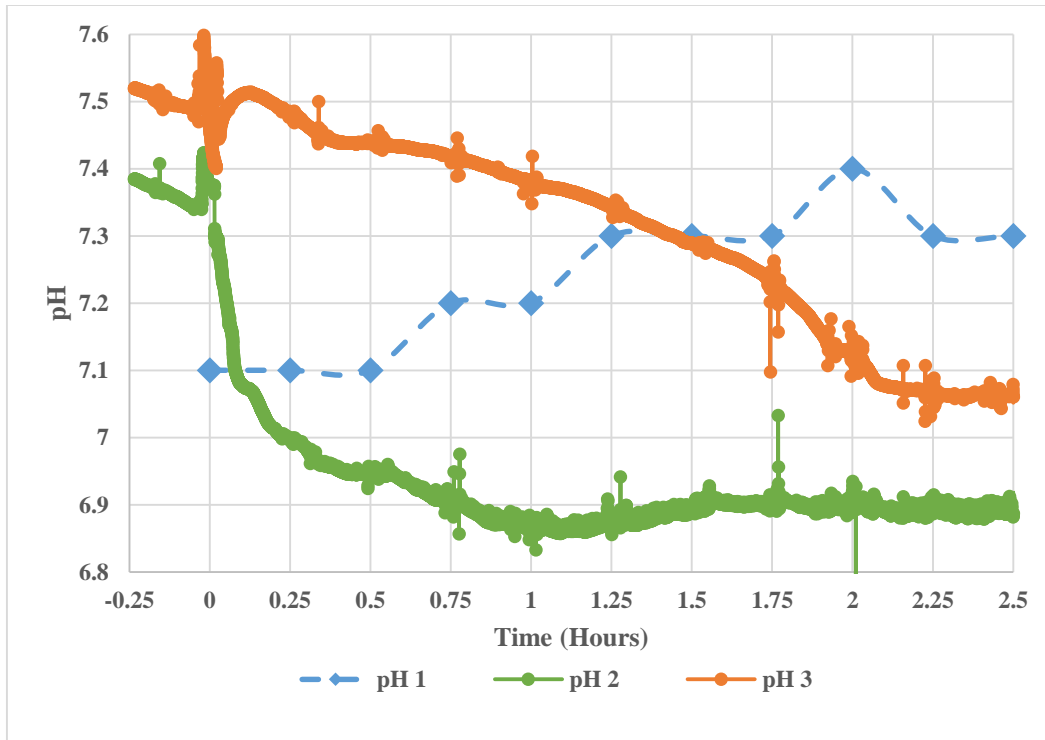


Figure 1.1: pH microelectrode response in lysate: the green and orange profiles represent pH microelectrodes for continuous sample measurement in lysate, the blue profile represents periodic sample measurements every 15 minutes in lysate

<sup>9</sup> RuDPP: ruthenium tris(diphenylphenanthroline) dichloride

Green Fluorescent Protein (GFP) was used as a demonstration protein for the Bio-MOD system. This protein could be used further as a biomarker, i.e., GFP would be attached to the target protein (serving as an indicator tag) to be expressed. GFP is ideal to work with, as its expression is directly proportional to its fluorescent intensity [14]. Furthermore, it is possible to ‘see’ what is expressed since the protein fluoresces green. Since BASS reads green and red fluorescence, it was tested to monitor GFP expression and purification in real-time. Thus, another variable (GFP) for measurement was discovered.

GFP expression rate (i.e. rate at which GFP is produced) analysis is an important tool that helps interpret the expression process. A technique to analyze the ‘rate’ signal was developed to process expression rate data in real-time and for post-processing. The data needs to be filtered to reduce the signal noise. Various filters were tried and tested, and a comparative analysis for them is presented in this dissertation in

5.3 Filtered Rate Analysis (FRA). GFP purification was also monitored before and after the purification process, which provided visual feedback to monitor and control the purification process.

BASS cannot be used as is to monitor production of all proteins, since not all proteins fluoresce. All proteins, however, absorb UV light, and UV absorption is an established technique for the measurement of protein yield [16]. The sensor system was modified to measure UV absorption. Two methods of construction of the absorption sensor are discussed. The first proposed method is a straight-forward implementation that uses a UV LED-UV photodiode pair. The second method uses quantum dots along with a UV LED to convert UV radiation to visible red light to be measured by the preexisting Si-photodetector. The latter approach is a low-cost and efficient option, and contributes lesser noise to the system.

Thus, in this dissertation, an optical sensor system based on fluorescence measurements and UV absorption is developed for the monitoring of various bioprocess variables. Analysis techniques are established for processing of the data. The bioprocess analysis sensor system (BASS) is versatile and can be used in multiple setups.

## ***1.2 Research Contribution***

This PhD dissertation required the application of electrical engineering knowledge to develop solutions for the real-time monitoring and measurement of protein production. Training in the biotech and chemical backgrounds for protein production was essential. Skills for working in a wet-lab were developed to perform experiments to validate BASS in bioprocesses.

BASS is built upon optoelectronics that has been in development in the CAST lab. This work extended its use to fiber optics. The optics and mechanics needed for the system were designed and fabricated, which allowed the coupling of the hardware with a single-core optical fiber. This optical ‘electrode’ or ‘optrode’ would then have a chemical patch sensor<sup>10</sup> (pH/DO) fixed on the other end, and the optrode would be submerged in the bioprocess. Such a measurement method

---

<sup>10</sup> Chemical patch sensor: an indicator sensitive to changes in parameter measured is immobilized in a dry polymer matrix. It is called ‘patch’ because of its resemblance to a piece of paper

resulted in chemical sensor miniaturization. A ‘patch sleeve’ was created to ensure an easy way to attach the patch to the optrode (Chapter 3 and illustrated in Figure 3.4).

A software system was designed and implemented to control measurement with the optoelectronic system. The User Interface (UI) or graphic user interface was developed to abstract the technical implementation and provide a better user experience, given the inter-disciplinary nature of the team. The VI was able to identify key elements like type of chemical sensor used, number of channels on the optical sensor, the currents on the LEDs, etc. It enabled altering certain parameters like LED intensity (by changing current through them), naming/renaming the sensor, etc. Measurements from the bioprocess could be logged. The VI displayed the raw millivolt (mV) readings for fluorescent/absorbance intensity, but it was also possible to calculate and display actual pH/DO/GFP/absorbance readings, by prompting user to input a calibration equation for the same. Initially, each chemical patch sensor needed to be calibrated manually. A VI was then designed to automate the calibration process.

Procedures to calibrate the chemical patch sensors and the instrument were developed. Processes for verification of calibration, standardization of the sensor, and verification on *E. coli* and the lysate were also established. For the above processes, experimental test runs were conducted to collect data for initial interpretation. Multiple patches were calibrated to verify that the drift in calibration between subsequent patches was not significant. A mean calibration was derived as a backup, in the event of insufficient time allotted for calibration.

An approach to measure real-time GFP expression was designed. Anomalies like sudden change in measured signal were detected in the measurements when the optrode was submerged in the bioprocess. To avoid these, a fixed-length extension (FLE)<sup>11</sup> for the optrode was modelled in MATLAB, practically implemented, and verified. This FLE would serve as a limiter for the amount of GFP exposed to the optrode, thus limiting the fluorescence read by the sensor. Real-time monitoring of the GFP purification process was achieved by using the GFP optical sensor.

GFP expression rate analysis is an important tool for interpretation of the GFP expression bioprocess [19]. An algorithm was developed for filtering noise from expression data and then

---

<sup>11</sup> FLE: due to movement of optrode along the length of container in which it is submerged, there anomalies in fluorescence detected. An FLE would limit the amount of fluorescence detected no matter the depth of the optrode

deriving the rate in real-time. For post-processing of noisy rate data, a noise filtering procedure was derived by comparing the post-processing results obtained from various digital filters.

UV absorption is used to quantify protein production. The common instrumentation for the optical sensor was modified to enable UV absorption measurement. A comparative analysis was performed to evaluate two UV absorption measurement methods. Procedure development for absorption measurement using the UV sensor was done.

Bio-MOD is an inter-disciplinary project involving the contributions of people with backgrounds spanning across bio-technology, chemical and biochemical engineering, mechanical engineering, and electrical engineering. Contributions discussed above correspond to our sensors development and their incorporation in the entire Bio-MOD system.



### ***1.3 Chapter Organization***

**Chapter 1** gives an introduction to the dissertation research problem, presents the background information used, and discusses Bio-MOD. Motivation for the research performed and my individual contributions to the project are also presented.

**Chapter 2** deals with basic theoretical concepts of fluorescence and absorbance. The theoretical equations for calibration for pH and DO are derived. Practical modifications to these theoretical equations are also discussed. Instrumentation transfer functions (i.e., equations governing the hardware design) are derived for both, pH and DO, based on which, the circuit is designed. Standardization of electronics for BASS is another concept that is discussed in this chapter.

**Chapter 3** presents the system design for the optoelectronics and software. The pH and DO chemical patch sensors comprise a parameter-sensitive dye immobilized in a Silicone matrix<sup>12</sup>. The optics transport LED emissions to the chemical sensors, and fluorescent excitations from these sensors, back to the photodetectors with minimal losses. The electronics is designed to read this fluorescent signal, and filter out the noise. User interfaces for calibration and system interpretation and data logging are designed and implemented in LabVIEW, and their algorithms are presented in this chapter, along with a novel method for patch sensor determination. The hardware design for the absorbance sensor and the modifications made to the optical sensor are also presented.

**Chapter 4** presents a step-by-step validation of the chemical patch sensor for pH and DO measurements. First, the sensor is calibrated for pH and DO. These calibrations are then verified in known pH buffer solutions and known DO concentration solutions. A number of chemical patch sensors are calibrated and a statistical analysis for error in calibration is presented. A theoretical derivation for standardization of multiple sensors is done, and method for standardization for pH and DO sensors is determined. The DO patch sensors are sensitive to temperature; consequently, a method to derive the temperature coefficient (rate of change) for DO patch calibration is presented. The pH and DO sensors are then tested in an E. Coli cell culture (a well-established

---

<sup>12</sup> Matrix: crisscross arrangement of cross-linked polymers

bioprocess). Finally, the pH and DO patch sensors are tested in EPO (Erythropoietin) protein expression. The results and their interpretations are presented in this chapter.

**Chapter 5** discusses the use of the pH mode of BASS for GFP expression monitoring in real-time, as well as GFP monitoring during protein purification. The GFP sensor is calibrated and the calibration is verified as in the earlier chapter. The GFP sensor monitors an actual GFP expression and the data is presented here. A fixed-length extension (FLE) of the optrode is modelled and practically implemented to prevent anomalies in the data due to movement of the optical fiber (optrode). The rate of protein expression is an important tool in determining process flow. An algorithm calculating the rate for GFP expression is implemented for real-time and post processing of the data. This rate data needs to be filtered due to noise issues. A filtered rate analysis study is performed for GFP in order to determine which method works best in which situation. Protein purification is monitored using the same sensor. The dual-channel sensor system monitors the pre and post-purification process. BASS is also currently being used by the Ohio State University team for their purification experiments.

**Chapter 6** deals with the research and design of the UV absorbance sensor. All proteins absorb UV light and, hence, the amount of UV light they absorb can be used as a purification analysis tool. This chapter presents a comparative analysis of 2 methods of construction of the absorption sensor. Method-1 uses a UV LED-UV photodiode pair and method-2 uses a UV LED-Quantum Dot-visible-range standard Si-photodiode pair. The quantum dots are used to convert UV light to red light, thereby enabling the Si-photodiode to detect absorption.

**Chapter 7** is the conclusion to this dissertation. It summarizes the work done, discusses conclusions drawn from the results, and discusses future work and extensions.

## **Chapter 2. THEORETICAL DESCRIPTION OF SENSOR MECHANISM**

This chapter discusses the physical and chemical phenomena that constitute the foundation of operation of the bioprocess analysis sensor system (BASS). BASS can be used to track two of the fundamental processes in the light-matter interaction: fluorescence (for pH, dissolved oxygen concentration, GFP) and absorbance (protein concentration). These processes are discussed initially. Then, the theoretical calibration equations for the pH and DO chemical patch sensors are stated. From these, the instrumentation transfer functions<sup>13</sup> are derived that in turn, result in the practical calibration equations for pH and DO, respectively.

Measurement results from multiple sensor systems of the same type will be different due to non-ideal nature of the electronics, which results in non-ideal behavior. Standardization techniques for the BASS are needed in order to obtain similar results from multiple sensor systems that measure the same input variable. These techniques are discussed here.

BASS is used to measure UV absorption by modifying the operation mode of the fluorescence optical sensor system. The instrumentation concepts for designing the sensor is discussed. Quantum Dots<sup>14</sup> (QDs) are researched as a novel technique for developing the absorbance sensor.

---

<sup>13</sup> Instrumentation transfer function: mathematical representation of input and output parameters for instrumentation of BASS

<sup>14</sup> Quantum dots: nanoscale semiconductor devices

## 2.1 Fluorescence

Fluorescence is defined as the emission resulting from the return of a paired electron from a higher orbital to a lower orbital, as illustrated in the Jablonski diagram given in Figure 2.1 [20].

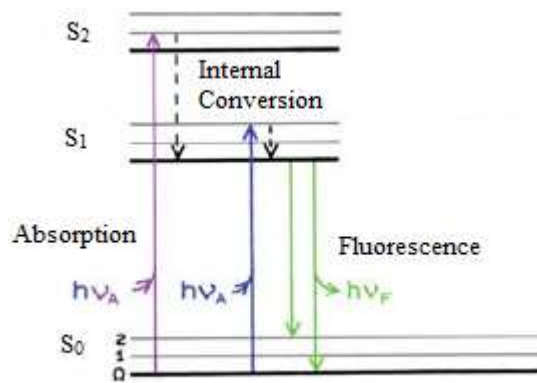


Figure 2.1: Jablonski diagram illustrating the concept of fluorescence

As seen in the figure, the fluorescent substance absorbs photons from an excitation light. This results in the electrons jumping from a lower orbital (S<sub>0</sub>) to a higher orbital (S<sub>1</sub> or S<sub>2</sub>). Internal conversion occurs at the higher orbitals at rates lower than 10<sup>-12</sup> seconds. When the electrons fall back to S<sub>0</sub>, the excess energy is released in the form of photons. Fluorescent emission generally occurs from a thermally equilibrated excited state, i.e., the lowest energy vibrational state S<sub>1</sub>. The typical lifetime of a fluorophore is 10<sup>-8</sup> seconds [20].

## 2.2 Chemical Patch Sensor

The chemical patch sensor was designed by immobilizing a dye sensitive to pH/DO concentration in a polymer matrix. This dye reacts with change in either parameter and emits fluorescence whose parameters depend on the pH of the solution or DO concentration in the solution respectively.

- ***pH patch***

The pH (power of Hydrogen) of a solution is the measure of the molar concentration of hydrogen ions  $[H^+]$  in the solution and is given by the negative logarithm of the hydrogen ion concentration in the solution and can be measured using indicators. Numerically, it is given by the equation

$$pH = -\log_{10} [H^+] \quad (2.1)$$

In this system, a fluorescent indicator 1, 8-dihydroxy-3,6-pyrene disulfonic acid disodium salt (DHDS) is immobilized in a cross-linked polyethylene glycol hydrogel matrix with suitable optical and diffusion properties [21]. The hydrogel is optically transparent while presenting only a minimal diffusion barrier to Hydrogen ions. DHDS exhibits two excitation wavelengths, one violet ( $\lambda_1 = 405$  nm) corresponding to acidic form, and the other blue ( $\lambda_2 = 457$  nm) corresponding to its basic form. The ratio of emission intensities,  $R = I_{\lambda_2}/I_{\lambda_1}$ , for these two wavelengths is related to the proton concentration according to [3],

$$pH = \log \left[ k_a \frac{(R_{\max} - R)(\epsilon_{A^-} \Phi_{A^-})_{\lambda_2}}{(R - R_{\min})(\epsilon_{HA} \Phi_{HA})_{\lambda_2}} \right] = pK_a + \log \frac{R_{\max} - R}{R - R_{\min}} \quad (2.2)$$

where  $R_{\min}$  and  $R_{\max}$  are the ratios of intensities corresponding to the acid (HA) and conjugate base ( $A^-$ ), respectively,  $\epsilon$  and  $\Phi$  are the extinction coefficient and quantum yield of each species evaluated at  $\lambda_2$ , and  $K_a$  is the equilibrium dissociation constant [3]. Thus, the ratio of the intensities of the emissions is related to the pH of the solution in which the DHDS patch is placed. Equation (2.2) is the theoretical equation used for calibration and is non-linear.

- ***Dissolved Oxygen (DO) patch***

Optical detection of dissolved oxygen is achieved using quenching-based indicators [22]. In this dissertation, an oxygen sensing patch with immobilized (rhuthenium tris(diphenyl phenathroline) dichloride [23] was used. The dye is physically adsorbed on silica gel, and the gel in turn is embedded in silicone rubber. The rubber is an optically transparent matrix, which allows for easy passage of gases due to its high diffusion constant. However, it is extremely hydrophobic, which prevents the immobilized indicator from washing out. RuDPP is a member of a well-known family of phosphorescence dyes, and in the presence of di-oxygen, dynamic quenching of its excited-state occurs [23]. The emission intensity  $I$  and the decay constant  $\tau$  in the presence of molecular oxygen is given by the Stern-Volmer equation

$$\frac{I_0}{I} = \frac{\tau_0}{\tau} = 1 + k_{sv} \tau_0 [O_2] \quad (2.3)$$

where  $I_0$  is emission intensity in the absence of oxygen,  $\tau_0$  is the decay lifetime constant in the absence of oxygen,  $k_{sv}$  is the Stern-Volmer constant, and  $[O_2]$  is quencher concentration [1]. As the decay constants do not depend on dye concentration, their values are most often used for oxygen determination. Equation (2.3) is the theoretical representation for calibration of the DO patch.

- ***Instrumentation transfer functions***

Equations (2.2) and (2.3) represent the theoretical transfer functions of the chemical transducers, which convert the chemical quantity into parameters of light. However, BASS consists of a chemical and an optical transducer, which converts the light into electric signal. Therefore, the full transfer function of the instrument needs to be derived. Furthermore, as the sensor system is capable of working with more than one chemical transducer and otherwise, establishment of transfer functions for each case is also necessary.

Most often, the fluorescence signal is measured in the presence of ambient light with an intensity that is orders-of-magnitude higher than the fluorescent signal itself. Furthermore, ambient

light can have multiple components originating from sunlight, incandescent and/or fluorescent light bulbs, etc. The spectral content of these sources varies greatly. The intensity of incandescent lights is modulated at 100 or 120 Hz (double the AC line frequency depending on the country), while the intensity of the fluorescent lights with electronic ballast is typically modulated at approximately 45 kHz (double the switching frequency of the ballast, which is set above the audible range) [24]. Additionally, the excitation light can create interference that is coherent with the signal, and this interference can be both of optical origin (light leakage through the optical filters), or electromagnetic origin (inductive or capacitive coupling from the excitation LED into the photodetector). Thus, the signal-to-noise ratio (where noise is considered as all the unwanted signals) can be easily as low as 1:1000 or even lower. To improve this signal-to-noise ratio of the final measurement, an approach that allows extracting the fluorescent signal from all this noise is used. Such an approach is known as lock-in detection, synchronous detection, or stochastic resonance [25].

First, the intensity of the excitation light is modulated at a frequency that is distinctly different from the interference that results in modulation of the emission signal as well [20], [26]. The modulation of the emission signal with respect to the excitation signal modulation is a property of fluorescence [20]. The amplitude of the emission signal is

$$A_{EM} \sin \omega t = \frac{A_{EX}}{\sqrt{1 + \omega^2 \tau^2}} \Phi \sin(\omega t + \phi) \quad (2.4)$$

where  $\tau$  is fluorescence decay rate of the fluorophore,  $\omega$  is modulation frequency of light,  $\Phi$  is quantum yield, and  $\phi$  is the phase-shift between the excitation and emission signals. It can be derived that  $\tan \phi = \omega \tau$  [20].

In case of pH measurements, the decay rate of the DHDS dye is in range of single nanoseconds. Modulating the excitation at 10 kHz would result in an emission also modulated at 10 kHz, with the denominator of equation (2.4) approximately being 1. Similarly,  $\phi \approx 0$  and, hence,  $A_{EM} = k A_{EX}$  where  $k$  is a constant.

In the case of oxygen measurements, the fluorescence decay rate of the RuDPP dye varies between 1 and 5 microseconds. When the excitation light is modulated at 75 kHz, the occurring

phase shift  $\phi$  is significant (up to 62 degrees). Therefore, finding the phase shift allows determining the decay rate  $\tau$  and hence, the oxygen concentration.

As the frequency of the signals is fairly low, their amplitude or phase are found by homodyning [25]. The signal is multiplied by 2 instances of the excitation signal, one with zero phase shift ( $\sin\omega t$ ), and the other with a  $90^\circ$  phase shift ( $\cos\omega t$ ) as shown in equation (2.5).

$$IP(\omega t) = A_{EX} A_{EM} \sin(\omega t + \phi) \sin(\omega t) = \frac{1}{2} A_{EX} A_{EM} [\cos(\phi) - \cos(2\omega t + \phi)] \quad (2.5)$$

$$QD(\omega t) = A_{EX} A_{EM} \sin(\omega t + \phi) \cos(\omega t) = \frac{1}{2} A_{EX} A_{EM} [\sin(\phi) + \sin(2\omega t + \phi)]$$

Where  $IP(\omega t)$  is the in-phase signal and  $QD(\omega t)$  is the quadrature signal. This signal is then passed through a low pass filter [25] which results in,

$$IP_{LPF} = \frac{1}{2} A_{EX} A_{EM} \cos \phi ; QD_{LPF} = \frac{1}{2} A_{EX} A_{EM} \sin \phi \quad (2.6)$$

Consider pH measurements. As  $\phi \approx 0$ ,  $IP_{LPF} = A_{EX} A_{EM} / 2$  and  $QD_{LPF} = 0$ . Hence, ratio  $R_{IP}$  for the IP values when exciting at two wavelengths is given by,

$$R_{IP} = \frac{IP^{\lambda_1}}{IP^{\lambda_2}} = \frac{A_{EX}^{\lambda_1} A_{EM}^{\lambda_1}}{A_{EX}^{\lambda_2} A_{EM}^{\lambda_2}} = k R \quad (2.7)$$

Here,  $R$  is the ratio of emissions from equation (2.2) and  $k$  is the ratio of excitation amplitudes at two different wavelengths. This ratio must be constant to obtain reliable calibration. Thus, the transfer function of the pH sensing optoelectronics is given by,

$$pH = pK_a + \log \frac{R_{\max} - IP^{\lambda_1} / IP^{\lambda_2}}{IP^{\lambda_1} / IP^{\lambda_2} - R_{\min}} \quad (2.8)$$

Dissolved oxygen concentration measurements are derived from the decay rate  $\tau$  that is proportional to  $\tan \phi$ . From equations (2.6) and (2.7), it follows that



$$\tan \phi = \frac{IP}{QD} \quad (2.9)$$

Therefore, from equations (2.3) and (2.9), the transfer function for DO sensing is

$$[O_2] = \frac{1}{k_{sv}} \left( \frac{\tan \phi_0}{IP/QD} - 1 \right) \quad (2.10)$$

where  $\phi_0$  is the phase angle when the DO concentration in the solution is zero.

- *Standardization of optoelectronics*

The goal of standardization is to achieve the same measurement readout when the same chemical sensor is read using several different optoelectronic transducers. Furthermore, if the optoelectronics readout is equivalent to a lab-grade (i.e. properly corrected spectrally) fluorometer, the chemical sensors can be produced and qualified independent of the hardware used for their interrogation.

Lab grade fluorometers are standardized using excitation spectral corrections and emission spectral corrections. For excitation side correction, the measured fluorescence emission is normalized by the excitation intensity. In effect, the resultant emission is equivalent to excitation with white light [20], [27]. Emission side correction is usually also required due to changes in detectors sensitivity with the wavelength.

In the presented optical sensor system, the reading is always a ratio. When measuring pH, the emission spectrum is the same regardless of the excitation wavelength. When measuring DO, the in-phase and the quadrature components of the same emission are ratio-ed. Therefore, any spectral variation on the emission side are canceled out, and correction is not needed. However, excitation side correction intensity for pH and phase correction (due to the non-ideal frequency response of the optoelectronics) for DO are still required.

## 2.3 Absorbance Sensor

The absorbance sensor was constructed by replacing the visible blue LED on the optical sensor system with an 280 nm UV LED. The most obvious choice was to replace the Si-photodiode with a UV photodiode and observe UV absorbance. However, this method proved contribute more noise to the system (with respect to raw millivolt signal) and was much more expensive. Hence, another method was devised where quantum dots were used as an option to convert the UV light into the visible spectrum. These were used along with the already present Si-photodiode.

- **Absorbance**

As seen in Figure 2.1 on page 12, a substance absorbs the photons from an emission. The amount of photons absorbed by the substance is given by Beer-Lamberts law as follows [16], [20]:

$$A = \ln\left(\frac{I_0}{I}\right) \quad (2.11)$$

where A is the absorbance,  $I_0$  is the intensity of incident light and I is the intensity of transmitted light. The Beer-Lamberts law forms the basis of the absorbance sensor.

- **Quantum Dots (QDs)**

Quantum dots (QDs) are small semiconducting nanocrystals with diameters in the range of 2-10 nm [28]. These are highly luminescent, photo-stable semiconducting nanoparticles, which exhibit much higher photoluminescence quantum efficiency than their bulk counterparts [29], [30]. All commercially available QDs have high absorption in the UV range. As a result, it is possible to achieve fluorescent emission from the QDs in any part of the visible spectrum with UV excitation. Since the sensitivity of the Si-photodiode is significantly higher at  $\lambda \sim 630$  nm, as compared with UV, we selected QDs that emit in the red visible range [30], [31].

## ***2.4 Summary***

A theoretical foundation for BASS is presented in this chapter. Fluorescence and absorbance are explained on a molecular level. An overview of the chemical patch sensor is provided. Transfer functions defining the hardware for the sensor system are derived. Standardization for multiple systems is discussed. Quantum dots as wavelength convertors for the absorbance sensor are discussed.

## Chapter 3. INSTRUMENTATION DESIGN FOR BIO-PROCESS ANALYSIS SENSOR SYSTEM (BASS)

This chapter discusses the design and implementation of BASS. It comprises of hardware and software sections for both the fluorescence and absorbance sensor systems. The hardware design for the fluorescence-based system involves the chemical patch sensor design, optics design, and electronics design. The software design section describes the calibration user interface and the data logging user interface in detail.

For the absorbance-based system, the electronics remains the same. The LEDs are changed to UV LEDs, and the optics is modified accordingly. These modifications are described in detail in this chapter.

The software design for both types of systems is the same. Certain modifications are made based on the variable being measured.

### ***3.1 Hardware Design for Fluorescence Sensor***

The fluorescence-based sensor system measuring pH, DO, and GFP is as shown in Figure 3.1. The sensor comprises of 3 relatively independent modules:

1. **The chemical patch sensor** – The dye immobilized in patch sensor acts as an indicator for change in pH/DO. Upon excitation, dye reacts with change in either parameter and emits fluorescence whose parameters depend on the pH of the solution, or DO concentration in the solution respectively. GFP detection requires no patch sensor.
2. **Optics** – A single core optical fiber provides a path for excitation and emission light. A beam combiner is used to channelize the different LED light paths with a dichroic mirror, short pass filter, and a long pass filter so that they reach the optical fiber. A half ball lens focuses the light coming from the LEDs into the optical fiber, and the emission from the fiber into the

photodiode. A lens holder is used to hold the fiber and the lens, and align it with the beam combiner and circuit board.

3. **Electronics** – The electronics circuit board consists of a system-on-chip (SOC) that controls LED drivers, differential amplifiers, and lock-in amplifiers. The board is designed such that it senses maximum fluorescence signal but there is minimum noise contribution to this signal.

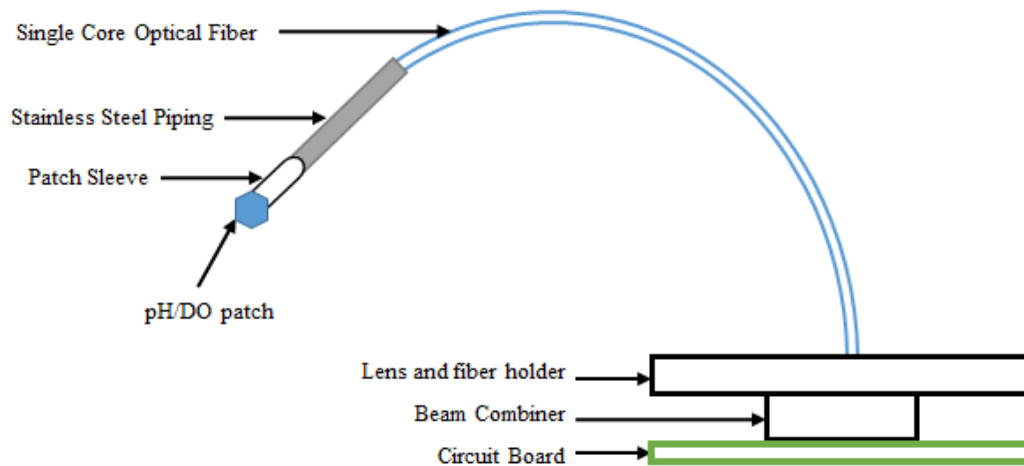


Figure 3.1: Diagram of single channel fluorescence sensor

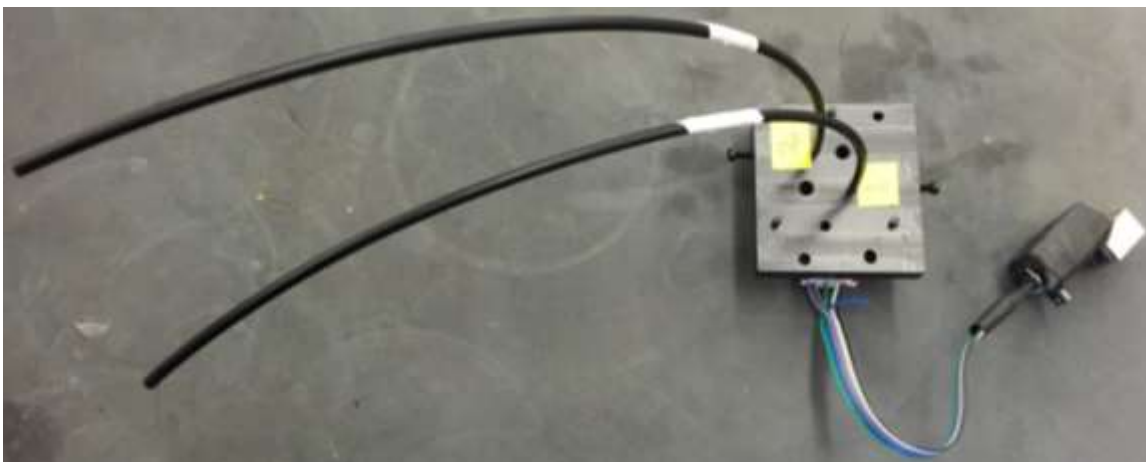


Figure 3.2: Image of dual channel optical sensor

- **Chemical Patch Sensor**

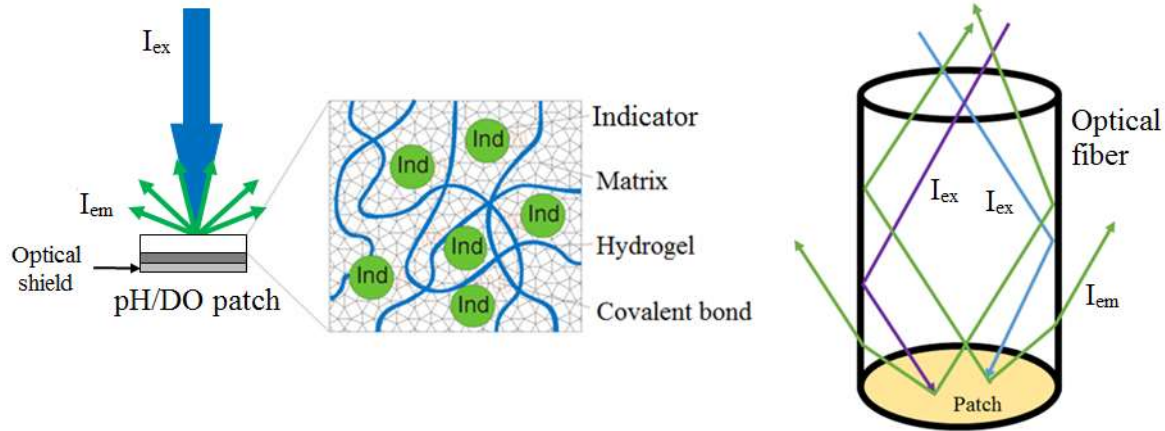


Figure 3.3: Excitation and emission light directionality. **Left:** Through-space directional patch illumination produces omnidirectional emission. Optical shield prevents excitation and emission passing through patch. The arrangement allows only for close-up placement of chemical patch, as the amount of light reaching the detector depends on the distance. **Middle:** immobilization of the optical indicator in the patch. **Right:** Positioning the patch on the tip of a fiber captures all the emission that is within the acceptance cone regardless of the length of the fiber [2].

The pH or DO sensors [1], [3] have a form factor of a thin foil ( $\sim 500\ \mu\text{m}$ , with  $\sim 100\ \mu\text{m}$  sensing layer) comprising of sensing layer sandwiched between a light shield and an adhesive layer (Figure 3.3 left). They can be used by directly attaching it on the inner surface of a vessel window and probing it externally. This approach works in cases where ample space is available for access of the optics through the window. In cases when the space is limited (small size vessels, lack of vessel windows, or presence of only small ports), the sensors are placed on the tip of a plastic optical fiber (Figure 3.3 right).

In order to ensure tight reusable coupling between the fiber and the patch, a 'patch sleeve' was developed as shown in Figure 3.4.

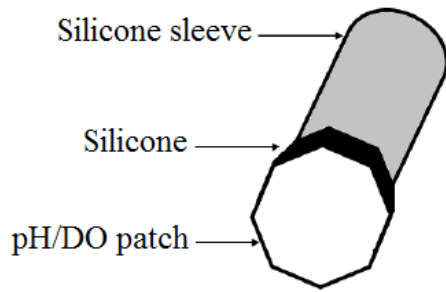


Figure 3.4: Patch sleeve design

The patch is attached to one side of a short silicone tubing using RTV silicone rubber. The tubing diameter is slightly smaller than the fibers jacket, ensuring that the patch stays in place due to the compression, while removing the possibility for the tested medium to enter the space between the fiber and the sensor foil.

- ***Optics***

In the case when the system was used with optical fiber, 15 inch long single core plastic optical fiber manufactured by Edmund Optics is used (Core diameter = 1960  $\mu\text{m}$  fiber diameter = 2000  $\mu\text{m}$ , outer diameter = 3mm, refractive indices for core and cladding = 1.49, 1.402 respectively, NA = 0.5, Edmund Optics). One end is fit inside a stainless steel tubing with inner diameter equal to the outer diameter of the fiber (i.e. 3 mm). This piping helps steady the fiber while taking readings. On the other end, the fiber enters a plastic holder (Figure 3.5). The holder keeps the fiber aligned with the incoming light and also holds the focusing lens. A half-ball lens with 5 mm diameter is used to focus the excitation light into the fiber and emitted light to the photo-detector.

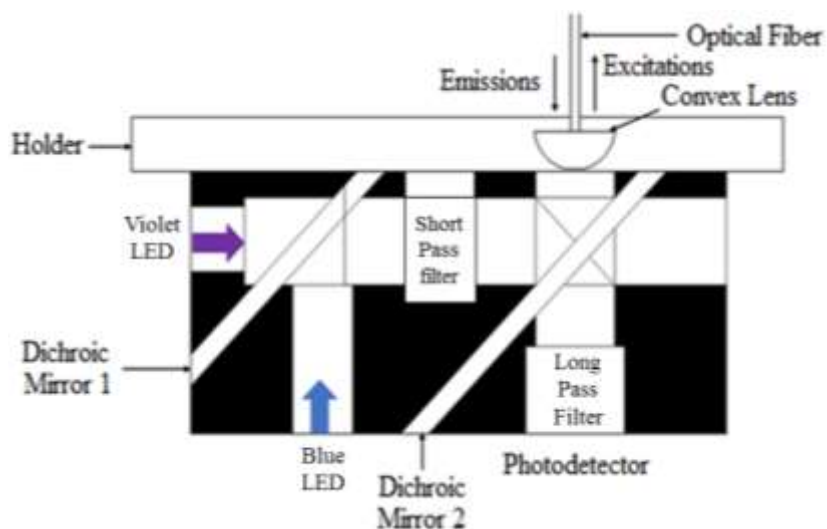


Figure 3.5: Beam combiner/splitter setup

In order to perform ratiometric excitation, two LEDs with emission maxima at 405 nm (violet) and 465 nm (blue) are used. They need to illuminate the same area of the sensing foil so as to avoid differential bleaching. Therefore, a beam combiner/splitter is used to direct the light from the LEDs and to the photodetector. As seen in Figure 3.5, the blue and violet LED light is combined into a single beam using a dichroic filter with a cut-off 430 nm (450FL07, Andover, NH, oriented at 450 incidence). The 'red tail' of the LED emission is removed by passing the beam via colored glass short-pass filter (BG-24, Schott). Then, the beam is directed toward the fiber/window using a second dichroic mirror (475FD68, Andover, NH, oriented at 450 incidence). The mirror reflects the blue and the violet part of the spectrum while transmitting the red and the green one. The returning fluorescence (with peaks  $\sim 530$  nm in the case of pH sensing or 610 nm in the case of oxygen sensing) passes through the dichroic mirror and is additionally filtered using a long-pass filter (500FH90, Andover, NH). The use of the long-pass filter allows to detect the emission either from the pH or from the DO chemical sensors.

- **Electronics**

The electronics (Figure 3.6) consists of 3 main blocks: LED drivers, lock-in photodetectors, and system-on-a-chip controller (SOC, MSP430F4270, TI). All three have separate power supplies



to avoid synchronous pick-up of interference via power fluctuations. The LED drivers are powered with 4.75 V to provide sufficient forward bias of the LEDs. The lock-in photo-detection module is powered also by 4.75 V to provide  $\pm 2.37$  V for the operational amplifiers. The SOC runs on 3.3V. All the power is derived from USB, which also provides bidirectional communication with the main computer.

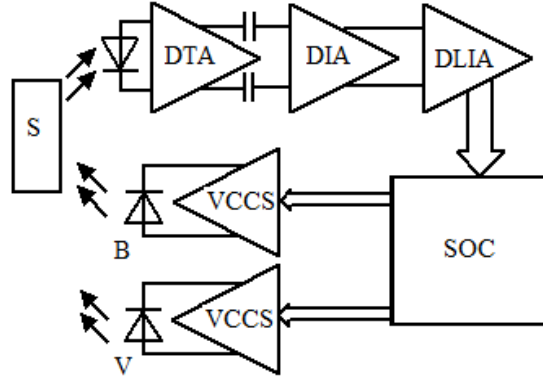


Figure 3.6: Block diagram for the electronics, DTA differential transimpedance amplifier, DIA differential inverting amplifier, DLIA differential lock-in amplifier, B blue LED, V violet LED, S sensor optics and chemistry, VCCS voltage controlled current source, SOC system-on-a-chip

The LED drivers are modulated, voltage-controlled current sources with shut-down capability. As such, video operational amplifier (OPA355, Texas Instruments) in current follower configuration was used as shown in Figure 3.7. The resistive divider on the non-inverting input ( $R1$ ,  $R2$ ) scales the control voltage  $U_C$  down to allow for fine control of the current through the LED. The capacitor  $C1$  in parallel with the resistor to the ground smoothens the sharp transients and reduces the spurious content in the electromagnetic emissions. The current through the LED is given by the equation:

$$I_{LED} = \frac{U_C}{R3} \frac{R2}{R1+R2} \quad (3.1)$$

The resolution of the current steps is  $25\text{ }\mu\text{A}$ . The drivers are able to produce highly repeatable intensity through the LEDs during a pulse, very high contrast ratio, and the capability to completely turn off the LED emission when disabled. The maximum current amplitude is  $\sim 50\text{ mA}$ . The drivers were capable of modulation frequencies up to  $6\text{ MHz}$ .

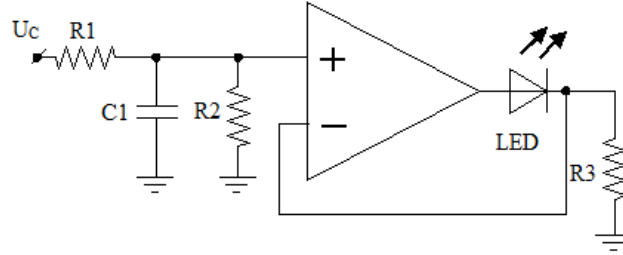


Figure 3.7: LED driver

The lock-in photodetector utilizes a PIN photodiode (BPW32, Osram) connected to a differential transimpedance amplifier (pair of OPA 354, TI). Differential amplifiers allow for doubling of the output amplitude or the bandwidth and are very efficient at suppressing common-mode interference. This is of great importance in miniaturized designs, where relatively high-current LED circuits are in very close proximity ( $7\text{-}8\text{ mm}$ ) to the very high-impedance inputs of the photodetectors. The bandwidth of the photodetector was  $\sim 200\text{ kHz}$ .

Two-stage amplification was used. The second stage was a capacitor-separated inverting amplifier. The frequency response of the stage was designed to remove the DC light component as well as the ever-present  $60\text{ Hz}$  light flicker. This allowed to avoid possible saturation of the detector under room-light illuminations. The output of the amplifiers was fed directly into a differential square-wave synchronous detector (Figure 3.8) that consists of discrete analog switches (SN74LVC1G3157, TI) and third-order low-pass filter with cut-off frequency of  $3\text{ Hz}$ .

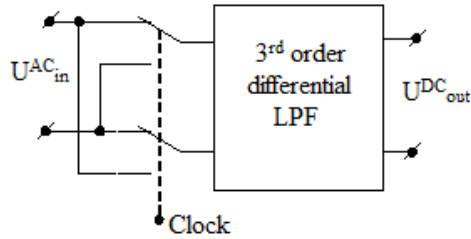


Figure 3.8: Synchronous rectifier

After the rectifier, the resulting DC voltage is proportional to the IP or QD as defined in the section Instrumentation transfer functions. It is worth noting that the respective waveforms were multiplied by a square wave instead of a sine wave; however it has been shown that this change can be easily accounted for in the calibration [25]. The use of the discrete components allowed for the use of a relatively slow and low-power system-on-a-chip, SOC (MSP430F4270, Texas Instruments), which features 16-bit 8 MHz microcontroller with built in 16 bit timers, 16 bit analog-to-digital converter (ADC) and 12-bit digital-to-analog converter (DAC). The synchronous detector was directly controlled by the SOC's timer. The on-chip DAC was used to set the LED brightness, while the ADC converter was used to monitor the output from the lock-in amplifier. The micro-controller is programmed to perform a number of tasks such as reading signal from photo-detector, controlling current in LEDs, turning specific LEDs ON and OFF, etc. A hexadecimal number is associated with each function the controller performs. This number is used by the user interface to communicate with the board via a USB cable.

### 3.2 Hardware Design for Absorbance-based Sensor System

- *UV absorbance sensor*

The absorbance sensor was constructed by modifying the sensor platform described above. The electronics for the board does not change. The Si-photodiode is replaced with a UV sensitive photodiode (FGAP71, Thorlabs), and the violet and blue LEDs are replaced by UV LEDs with  $\lambda_1 = 260$  nm and with  $\lambda_2 = 280$  nm respectively (UVTOP260TO18BL, UVTOP280TO18BL, SETi Sensor Electronic Technology Inc). The beam combiner uses a 266 nm dichroic mirror (Di01-R266-25x36, Semrock), and a 311 nm short pass filter (FF01-311/SP-25, Semrock). The UV absorbance-based sensor system is illustrated in Figure 3.9.

The LEDs, beam combiner, and PIN diode are aligned using a mechanical holder which is designed to hold a regular or flow-through cuvette carrying the protein to be tested. The LEDs operate at 20 mA (current is variable). Quartz plates are used to make the walls of the cuvette, since their absorption of UV light is minimal [20].

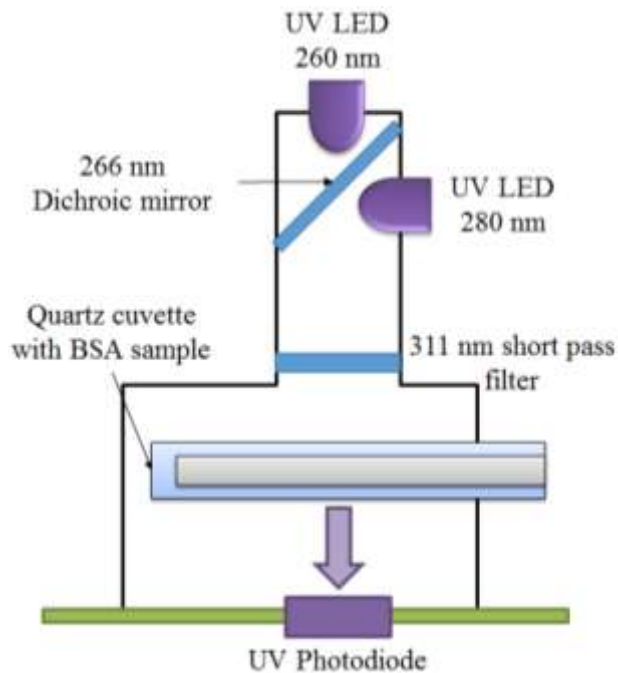


Figure 3.9: Schematics of UV absorbance sensor

For the UV absorbance-based sensor system, the UV LEDs turn on for 500 ms; then, its intensity is ‘on-off’ modulated at a frequency of 10 kHz (as in the pH measurement mode). This UV light passes through the protein solution in the cuvette, which absorbs part of the UV light. The absorbance corresponds to the concentration of protein in the solution and is calculated using Beer-Lambert’s law.

$$A = \lg\left(\frac{I_0}{I}\right) \quad (3.2)$$

where  $A$  is the absorbance,  $I_0$  is the intensity of UV light when there is no absorbance (blank correction), and  $I$  is the intensity of UV light not absorbed by the sample [32].

- ***Dual channel system for comparison between UV and QD system***

A dual channel BASS platform is used so as to compare in parallel, the performance of the QD-Si photodiode and UV photodiode. Their signals are passed through the same amplification and signal conditioning chain as described in the Electronics section. The visible LEDs (blue and violet) in this platform are replaced by UV LEDs (UVTOP280TO18BL, SETi Sensor Electronic Technology Inc,  $\lambda = 280$  nm). The Si-photodiode is used as is; a quartz plate with QDs deposited on it is added above it. This plate acts as the convertor for light from 280 nm to 630 nm. The second photodiode is replaced by the UV sensitive photodiode (FGAP71, Thorlabs). The setup for absorbance measurements and comparison is presented in Figure 3.10.

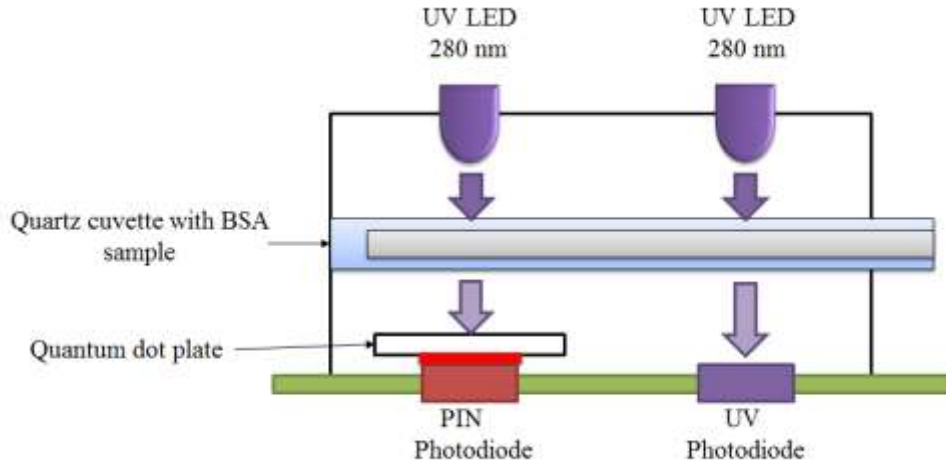


Figure 3.10: Schematics of UV quantum dots sensor

The LED and PIN diode are aligned using a mechanical holder which is designed to hold a regular or flow-through cuvette carrying the protein to be tested. The LEDs are operated at 25 mA. Quartz plates are used to make the walls of the cuvette, since their absorption of UV light is minimal [33]. Henceforth, the absorbance sensor system using QDs and Si-photodiode will be termed as the ‘QD sensor’ and the sensor system with only a UV photodiode will be termed as the ‘UV sensor’.

Both absorbance systems operate as follows: first, the UV LED is turned on for 500 ms; then, its intensity is ‘on-off’ modulated at a frequency of 10 kHz (as in the pH measurement mode). This UV light passes through the protein solution in the cuvette, which absorbs part of the UV light. The absorbance corresponds to the concentration of protein in the solution. The unabsorbed UV light passes through the quartz cuvette and reaches the quantum dot plate and the UV photodiode. The QDs convert the UV light into visible red light. This red light is then detected by the Si-photodiode. For the UV sensor, the UV photodiode detects the unabsorbed UV light directly. The hardware electronics convert this detected red/UV light to voltage. The absorbance for the data collected with both detectors is calculated using Beer-Lamberts law.

- ***Preparation of QD – Si-photodiode UV detector***

A suspension of CdSeS/ZnS alloyed QDs in toluene (753793-5ML, Sigma Aldrich) at a concentration of 1 mg/ml, is immobilized in Silicone on a quartz plate overnight. These dots are 6 nm in diameter, and have an emission at 630 nm. 1 ml of the QDs are taken, and the volume is reduced to 0.5 ml by heating the solution at a constant 100<sup>0</sup> Celsius, thus, letting the toluene evaporate. Then, 0.5 ml of the Silicone is added to this solution and thoroughly mixed. Hence, the ratio of QDs to Silicone is 3:1 and its concentration was 0.667 mg QDs in 1 ml Silicone. A 1 mm rectangular mold is cut out from a PMMA (poly (methyl methacrylate)) sheet and affixed to the quartz plate. The mixture is poured into the mold and left to cure overnight. The mold is removed after, and a QD deposition on the quartz plate is fixed on top of the Si-photodiode. Following figure shows the QD plate construction in the form of a diagram and an actual image.

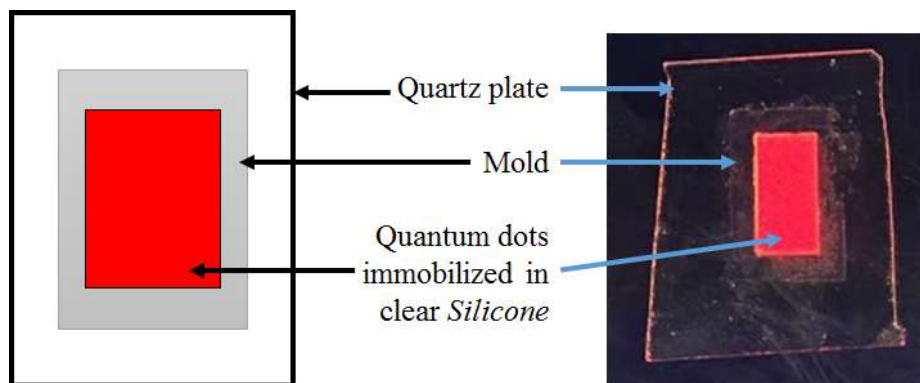


Figure 3.11: Illustration of construction of QD plate

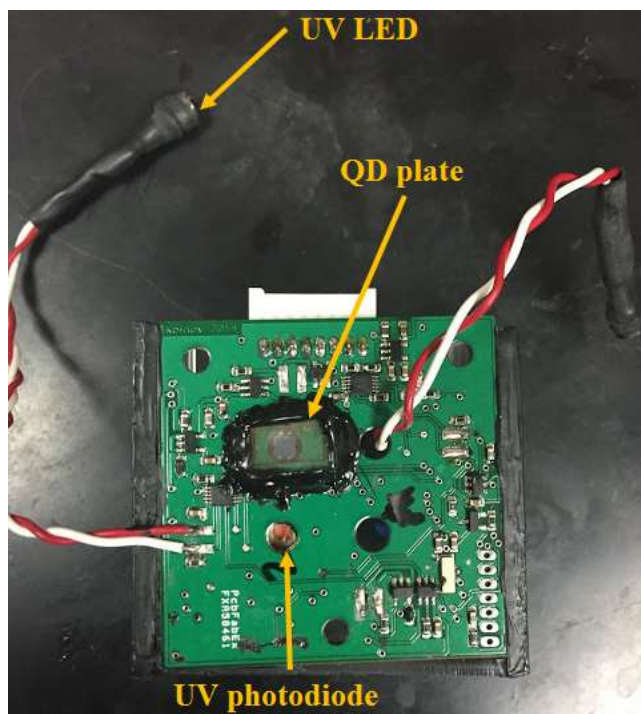


Figure 3.12: Image of QD and UV absorbance sensor

### ***3.3 Firmware Design for Bioprocess Analysis Sensor System***

The micro-controller is programmed to operate the system in slave mode and hence, it never initiates tasks. It handles three groups of tasks: testing, constants recording, and measurements. The testing task involves a set of commands that allows to verify the operation of the sensor peripherals, i.e. turning the LEDs on and off, switching between the in-phase and quadrature detection, or turning the photodetector on and off. The ability to save constants is necessary in order to adjust and remember the brightness levels of the LEDs, as well as to record the chemical sensor constants that would be used later for the actual calculation of the pH or DO. It is also recording the amplitude and phase offsets that would be subtracted from the final measurement. The measurement commands specify whether pH (amplitude measurement at two different wavelengths) or DO (in-phase and quadrature measurement on a single wavelength) will be performed. The device returns either the raw measured voltages or the calculated values of pH/DO depending on the command. It receives the commands and returns the measurement data in byte format via USB-to-RS232 converter (FT232, FTDI Inc.).



### ***3.4 Software Design for Bioprocess Analysis Sensor System***

The user interface (UI) for the optical sensor is designed and implemented in *LabVIEW*. A calibration UI and a data logging and calculation UI are designed for the same. The interface is designed such that the user has the flexibility to manually change various settings for the sensor system, for example, current supplied to LEDs, delay between samples taken when data is measured continuously, measuring and reading offsets and considering them while taking measurements, etc. It also had the ability to perform online calibration for pH, DO, and GFP.

Another added feature to this system is that it can measure fluorescence intensity of fluorophores in a solution when no chemical patch sensor is used. This feature was used for real-time measurement of GFP (Green Fluorescent Protein) concentration, since it was one of the products of the bioprocesses under study. Since the system was designed to detect green emissions, GFP concentration measurements using the fluorescence intensity mode were included as a feature in the system.

This UI was designed for rapid calibration of the pH and DO patches, and GFP. It can be used to calibrate two optrodes for either pH or DO patch sleeves, or just the plain optrodes without any chemical patch sensor can be calibrated for GFP measurement. It consisted of three steps; the first involves initial setup, where the user selected what variable is to be calibrated and the number of calibration points to be considered. The second step was the actual real-time logging of the data and collection of points in an array. For this, the system begins recording data at the time interval specified. There is a variable 'dy' which records the difference between present sample and the previous sample measured by sensor system. This was used to determine stability of samples collected by sensor system. Once the 'dy' value went below a certain threshold, user would 'Add a Point'. The 'Calibrations Recorded' array would record this measured value as well as the desired value that the user specified. The final step was actual calibration. After the required number of points had been recorded, the UI calculated the calibration curve and output the values. For pH and GFP measurement, a linear fit was calculated using the desired and measured points, whereas a quadratic fit (with intercept zero) was calculated for DO.

- *Calibration Visual Interface*

The flowchart describing the working of the calibration UI is given in Figure 3.13.

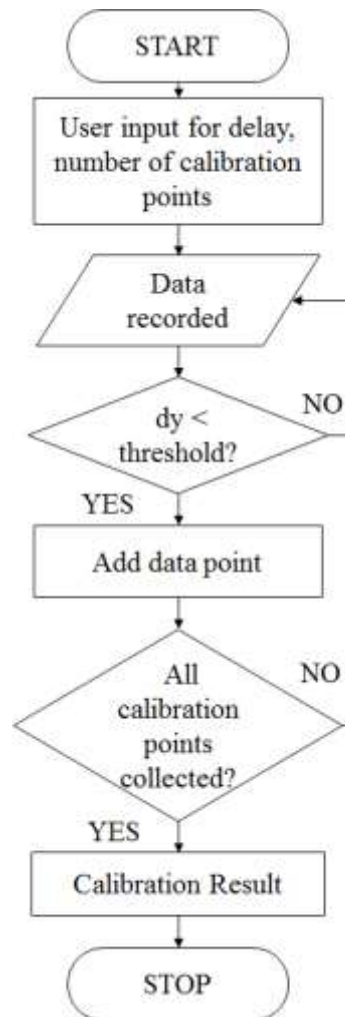


Figure 3.13: Flowchart describing the working of the calibration user interface

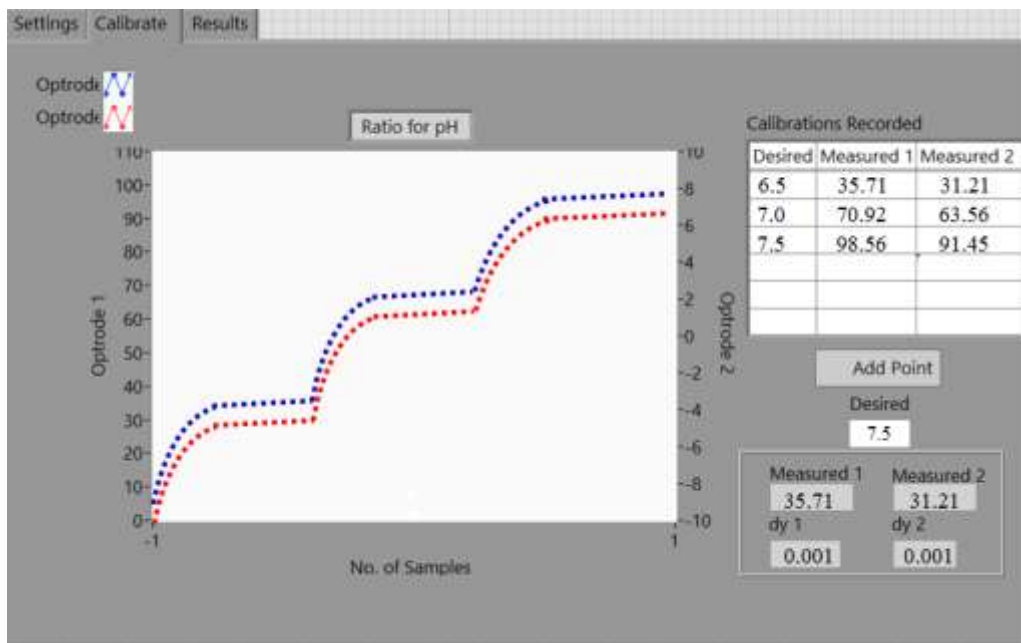


Figure 3.14: Screenshot of calibrate tab of calibration user interface

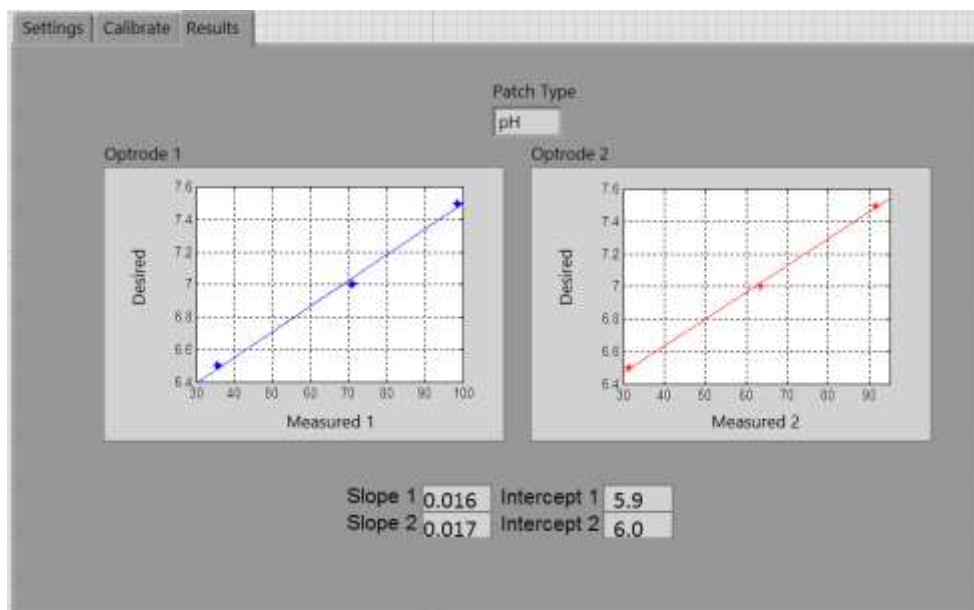


Figure 3.15: Screenshot of results tab of calibration user interface

Figure 3.15 and Figure 3.15 present a screenshot of the calibration UI. User decides what the desired value is and adds the measured value along with it to the 'Calibrations Recorded' array. The 'Results' tab then displays the calibrations. In this case, since pH is calibrated, the slope and intercept are displayed.

- ***System Interpretation and Data Logging (SIDL) User Interface***

Flowchart shown in Figure 3.16 (a) illustrates the working of the settings interpretation and data logging user interface. On start-up, the software performed several tasks on initialization. First, based on the voltage levels, it determined whether there was a chemical patch sensor in front of the optics. If there was no sensor (low amplitude measurements), the program can measure fluorescence intensity allowing the sensor to be used for monitoring of the expression of GFP. If a chemical patch sensor was detected (high amplitude levels), then the system determined whether this was a pH or DO sensor.

Then, it was determined whether a single channel or dual channel device was being used. To do this, a red LED was introduced in the system near the photo-detector. The UI compared the second red LED amplitude to first red LED offset. If the second channel red LED amplitude value was greater or equal to the offset, there were 2 fibers on the board, else there was only 1 fiber. The ability to use two channels was especially valuable when both pH and DO of a bioprocess had to be monitored simultaneously.

Once the chemical patch sensors were identified, the software waited for user to allow it to start measurement. If user decided to measure data continuously, one measurement cycle took typically 1 second. It was also possible to define longer intervals between the measurements to decrease the bleaching of the chemical patch sensor. The performed measurements were displayed in both numerical form and graphically, allowing for direct monitoring of the process variables.

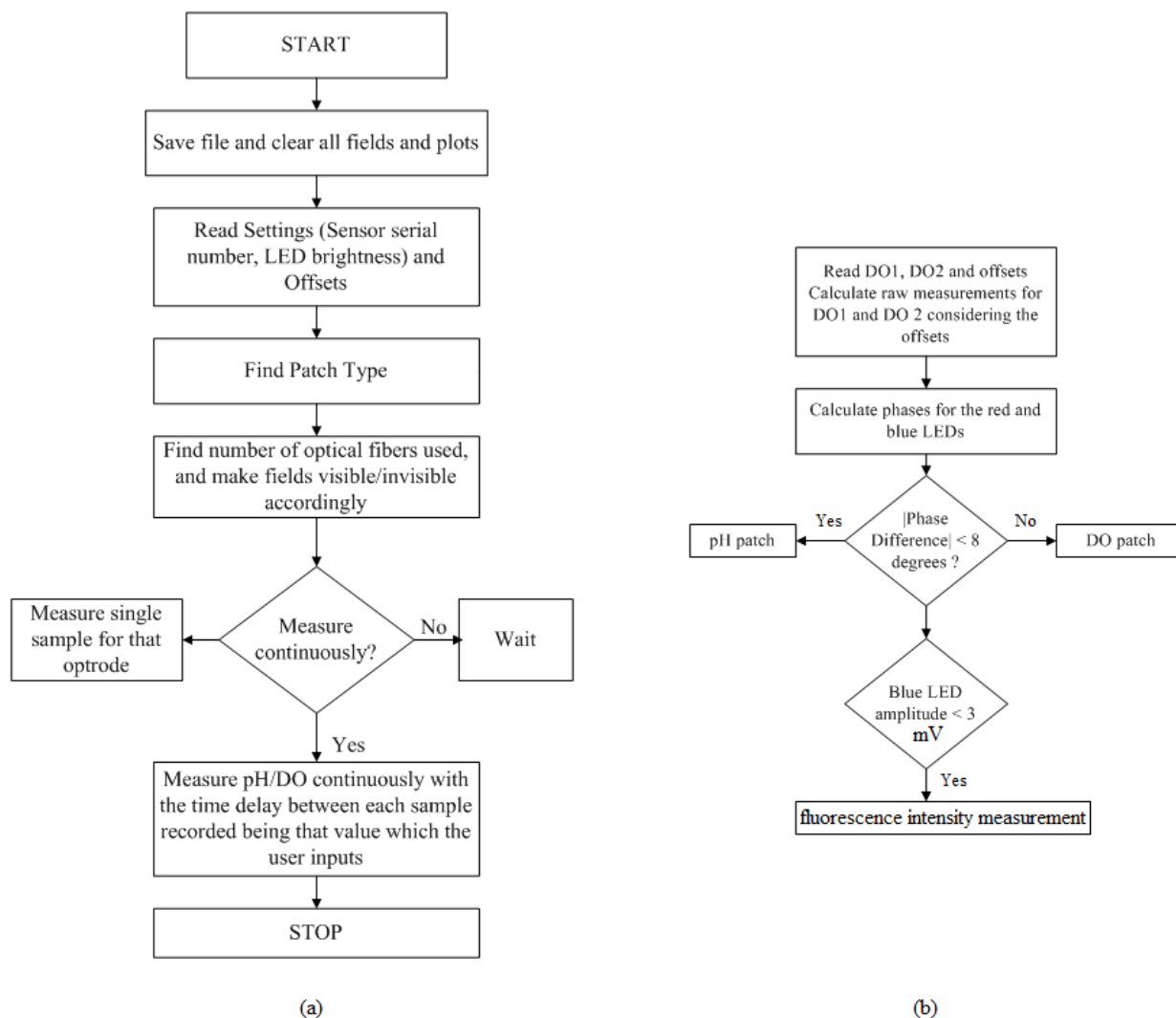


Figure 3.16: (a) Flowchart describing the working of the system interpretation and data logging user interface in brief, (b) Flowchart describing chemical patch type calculation

The flowchart shown in Figure 3.16 (b) describes how the chemical patch type is identified. As mentioned earlier, the pH sensing LEDs were modulated at 10 kHz, and DO sensing LEDs were modulated at 75 kHz. The fluorescence decay rate of the pH indicator is approximately 1000 times shorter as compared the DO sensor [13]. Hence, pH would not exhibit phase shift due to optical properties of the patch, and DO would have some phase shift measured in the emissions. Therefore, the phase was measured for each chemical patch sensor at 75 kHz (DO measurement),

irrespective of the chemical patch sensor mounted on it. Due to measurement at a higher frequency, circuit parasitic capacitances would introduce some phase shift even with the pH measurements; however, this electronics-derived phase shift would be still smaller than the shift resulting from the measurement of the oxygen patch. Hence, a threshold was determined for patch identification. If the measured phase shift was below this threshold, a pH sensor was being used, else a DO sensor was mounted on the optical sensor. If blue LED amplitude was lesser than 3 mV, there was no patch sensor mounted and the sensor system could be used for fluorescence intensity measurement.

When dual sensor systems were used, the auto-identification of the chemical patch sensor was especially valuable, as they were difficult to be identified visually due to their small size. This feature was aimed at prevention of possible mix-ups and loss of valuable data.

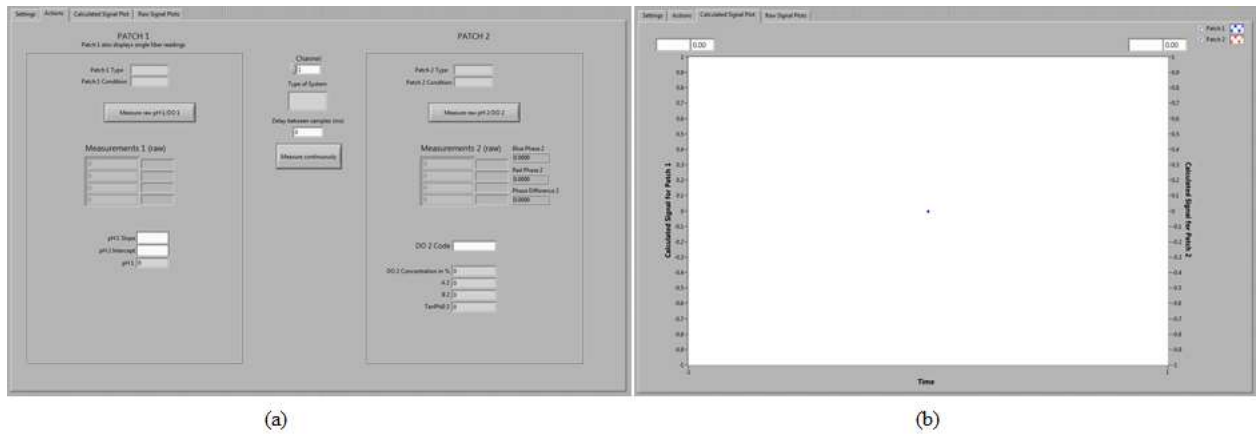


Figure 3.17: Screenshot of System interpretation and data logging user interface, (a) Actions tab, (b) Calibrated Signal Plot tab

Figure 3.17 is a screenshot of the system interpretation and data logging user interface. The 'Actions' tab displayed chemical patch sensor type, whether system had single or dual fiber, and measured raw voltages. In Figure 3.17 (a), first optical electrode (optrode) measured pH and second measured DO. There was a variable allotted for user to enter calibration data for both. Figure 3.17 (b) shows the calculated signal plot tab, which displayed the signal value calculated from the calibration data and raw data. Additional UI snapshots are displayed in APPENDIX C.

### ***3.5 Summary***

This chapter summarizes the design and construction of BASS. It explains in detail the chemical patch sensors, optics, and electronic design. Modification made to the system hardware to measure UV absorbance are illustrated. A software interface is developed to enable control of BASS, and to log and interpret data read by BASS.

## **Chapter 4. TESTING AND VALIDATION FOR PH AND DISSOLVED OXYGEN**

This chapter presents the data from all the experiments conducted to validate the pH and DO sensor, and discusses the observations and inferences. To validate the sensor for its ultimate use in a bioprocess, the sensor was calibrated to calculate true pH and DO values from raw mV readings. These calibrations were confirmed by using the sensor in a solution with known pH/DO. A study was then conducted by calibrating multiple chemical patch sensors. This study would determine an approximate calibration per batch of sensors and standard error could be defined for the same. The DO patches were temperature sensitive, hence, a temperature coefficient determination experiment was done. This coefficient would aid in extrapolating the calibrations for the DO patches at room temperature to the temperature at which the experiment needs to be conducted.

The optical sensor was then used in an actual bioprocess to validate its operation. An E. Coli cell culture was selected as the bioprocess (pH and DO profiles for the same are well defined in literature). Then, the sensor was tested in an actual protein expression run. EPO (Erythropoietin) was expressed for 4 hours and the pH and DO in the same were monitored by the optical sensor.



## 4.1 Apparatus Arrangement

The assembled sensor equipped with 2 optical fibers for simultaneous measurement of pH and DO (optrode 1 and 2 read from their respective sensors alternately) is shown in Figure 4.1, (a). The electronics fit on a 5x5 cm board. The height of the mounted optics was 2 cm. The system allowed for monitoring in small vessels (i.e. test tubes, microwell plates, etc.) with diameter down to 10 mm. Used in a single fiber configuration, the system was successfully used to monitor a process in an Eppendorf tube. The visual interface with the controls for the measurement is shown in Figure 4.1, (b). Note that all these experiments were conducted with all LEDs having a constant current of 20 mA through them.

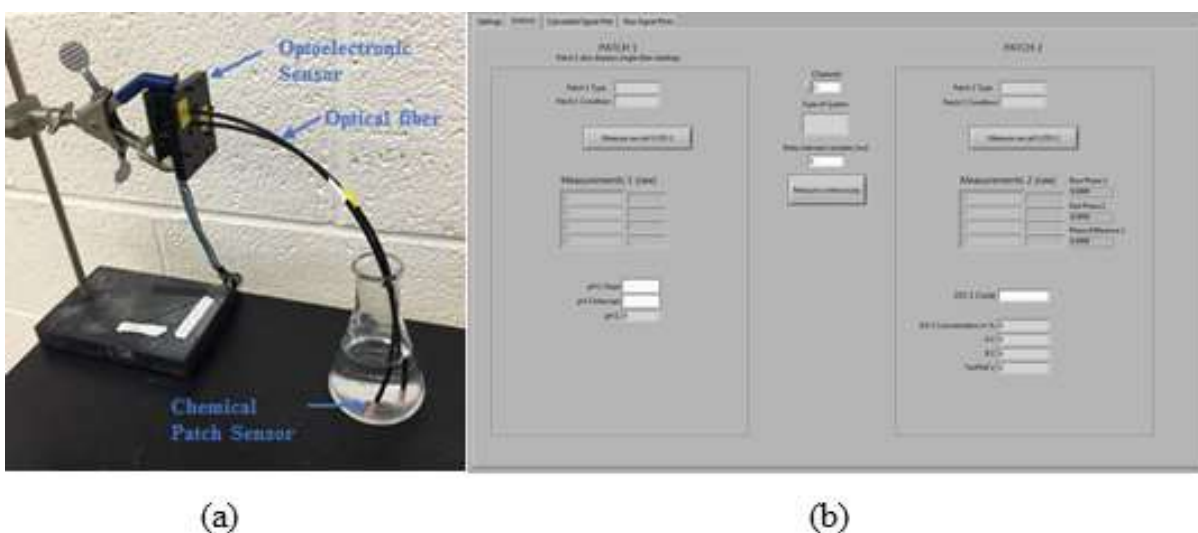


Figure 4.1: (a) The complete optoelectronic system with chemical sensors measuring in a flask  
(b) The visual interface measuring pH and DO in the flask. The visual interface measuring pH and DO in the flask

## 4.2 Calibration

- *pH calibration*

To calibrate the pH patches, the calibration VI recorded the ratio of the raw voltages of blue and violet amplitudes in pH buffers with four different values (6.79, 7.34, 7.52, and 7.75). Initially, the pH patch sleeves were kept immersed in DI (De-Ionized) water overnight for hydration.

Hydration of the patches was done so that the patches stabilize in the buffers faster. If the patches were used without hydration, the patches take longer (about 1.5 hour) to stabilize in the buffer whereas with hydration, it takes the patches about a half hour to stabilize. Hydration could also be achieved by microwaving the patches for 1 minute. But overnight hydration works better.

After hydration, the patch sleeves were put on the optical electrode and immersed in the first buffer of pH 6.79. Once the VI set all the initial parameters, measurements were taken continuously (once every 30 seconds in this case). Once the value of the ratio of blue amplitude to violet amplitude stabilized, i.e., when the difference between the previous sample and present sample ( $dy$ ) was less than a threshold (0.001 in the case of pH), the user prompted the VI to 'add' the present point to the calibration points array. Then the optrodes were immersed in the next buffer. Same procedure was followed for all four buffers. Once all points needed were collected in the array, a linear curve fit was done, whose equation represents pH calibration. This is illustrated in Figure 4.2.

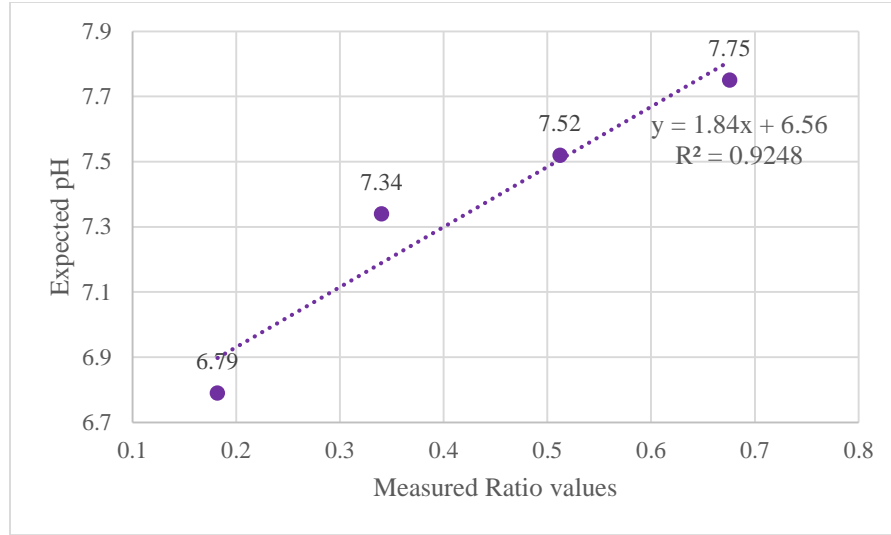


Figure 4.2: pH calibration

- **DO calibration**

To calibrate DO patches, the phase difference between the blue and red LEDs was recorded by the calibration VI for air percentages of 0%, 20%, 40%, 60%, 80%, and 100% and the phase offsets were subtracted from these values. Phase offsets were calculated using Rhodamine B dye. The decay rate of Rhodamine B (1.68 ns) is three orders of magnitude shorter than the decay rate of the used oxygen sensitive dye, RuDPP (~ 5μs in absence of O<sub>2</sub>). Therefore, the dye can be used as a fluorophore that will introduce zero degree phase shift at the modulation frequency for the oxygen sensor (75 kHz). In fact, the phase shift it introduces at this frequency is below the resolution of our phase detector (0.04°, 6 confidence intervals). The ends of the optical fibers (without the sensors) were positioned touching the wall of a small beaker holding the dye solution (1 mg Rhodamine B in 20 ml water). The resulting offset phase was recorded, and subsequently subtracted from the measured phase of the optical sensor. In this case, offsets were 0.78° for optrode 1 and 1.17° for optrode 2. For 100% air, there is approximately 21% DO in the solution.

The DO patches need to be calibrated at the temperature at which the actual experiment takes place, since the fluorophore in the dye is temperature sensitive [18]. The optrodes had the DO patch sleeves on them and were immersed in DI water. This apparatus was placed in an incubator at 37° Celsius. To change the percentage of DO in the DI water, a dual flowmeter was used with

one input as nitrogen gas and the other as air. The output channel of the flowmeter was placed in the DI water to bubble the output gas through it. By varying the nitrogen and air inputs, the percentage of DO in the DI water was varied. Table 4.1 refers to the flowmeter values to be adjusted to get specific percentage of DO in DI water. It should be noted that the percentages from 0 to 100 are for the percentage of air saturated with oxygen in the solution.

Air		Nitrogen		% Air	% DO
Reading in flowmeter	Flowrate (ml/min)	Reading in flowmeter	Flowrate (ml/min)		
0	0	138	349	0	0
52	69.2	116	277.7	19.9	4.2
77	139.2	96	208.9	40	8.4
97.5	209.6	76	139.5	60.1	12.6
119	280.6	51.5	69.9	80.1	16.7
141	351.6	0	0	100	21

Table 4.1: Flowmeter adjustments for DO calibration

Percentage DO	$\phi_D$ in degrees	$\phi_D$ in radians	$K = \frac{\tan \phi_0}{\tan \phi_D} - 1$
0	-57.85	-0.99	0
20	-43.25	-0.73	0.69
40	-37.63	-0.64	1.06
60	-34.5	-0.58	1.31
80	-31.5	-0.53	1.6
100	-28.61	-0.48	1.93

Table 4.2: Table showing calculation for DO calibration

The VI collected and saved data for the phase difference corresponding to the different percentages of DO in DI water. The stabilized phase difference values corresponding to each DO percentage were averaged. shows the values of  $\phi_D$  for each DO percentage.

The fourth column in Table 4.2 shows the calculation performed to get the value from which, calibration was done. The  $\tan \Phi_0$  value was the tangent of the phase difference when DO percentage in DI water was zero. The calibration curve was plotted as shown in Figure 4.3. The calibration is quadratic without an intercept.

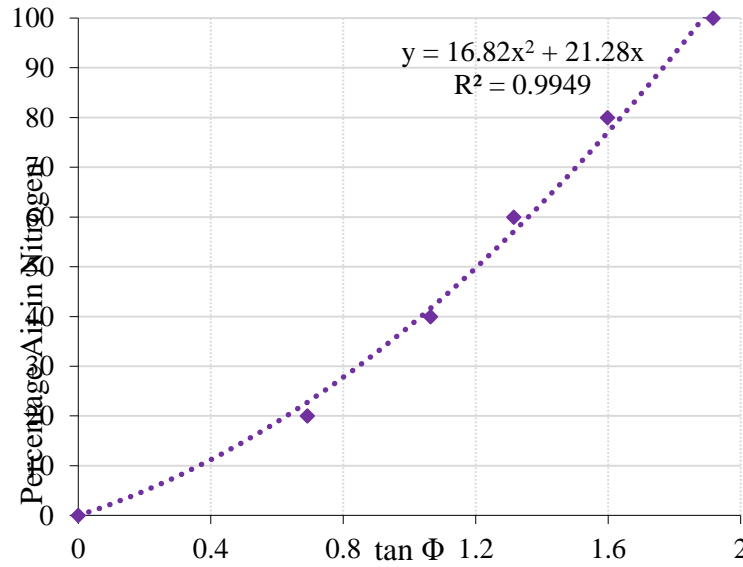


Figure 4.3: DO calibration

DO percentage is calculated as per the formula,

$$\% \text{ DO} = A * K^2 + B * K \quad (4.1)$$

where, A and B correspond to the DO calibration equation  $Ax^2 + Bx$  and  $K = \frac{\tan \Phi_0}{\tan \Phi_D} - 1$  (from equation (2.10)). The calibration VI outputs a code for the DO calibration which contains the values of A, B, K. It is a 12 digit value whose first 4 digits correspond to the  $1000 * \tan \Phi_0$  value, the next 4 digits represent  $100 * A$ , and the last 4 digits are  $100 * B$ . For example, for DO code 152111582259,  $\tan \Phi_0 = 1.521$ ,  $A = 15.86$ ,  $B = 22.59$ .

### 4.3 Calibration Verification and Statistics

This section discusses the experiments conducted to verify calibrations generated for pH and DO patches by the optical sensor. Optrodes were dipped in a solution with known pH and DO concentration, and measured every minute overnight. A number of pH and DO patches were also tested with the dual sensor to check variation in the measurements and calibrations. A temperature coefficient for DO patches was derived.

- *pH calibration verification and statistics*

In this experiment, a brand new pH patch was calibrated using 4 buffers, 6.77, 7.24, 7.51, and 7.82. The calibration for the patch was  $y = 1.74x + 6.47$ . After calibration, the patch was dipped in the pH 7.24 buffer and the sensor read data overnight. The pH profile for the same is as shown in figure given below.

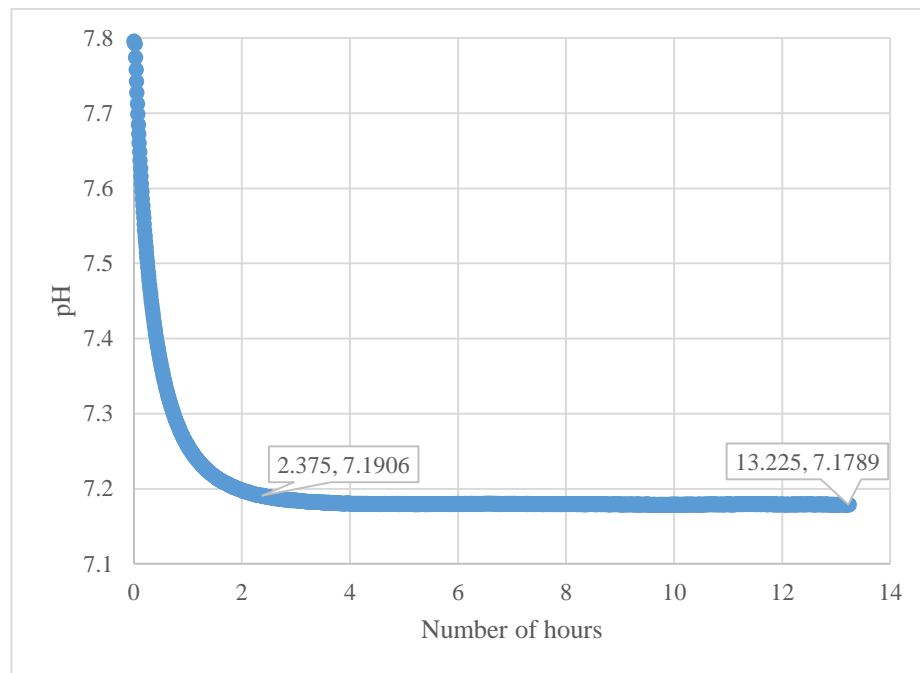


Figure 4.4: pH calibration verification

For this patch, after calibration, it took about 2 hours to stabilize in the 7.24 buffer. After stabilization, the average pH recorded was 7.18. The standard deviation was  $\sigma = 0.0045$ , and  $3\sigma = 0.0135$ , which implied that a deviation of  $\pm 3\sigma$  resulted in a deviation of 0.01 pH units to the signal. This was decided as the threshold beyond which, data would be considered to drift. The error was  $7.24 - 7.18 = 0.06$ , which was acceptable (since we were focusing on only one digit after the decimal point).

The brand new patch needed to sit in the buffer for about 2 hours for the sensor to get a stable reading. To prevent this, a second patch was dipped overnight in DI water. When this patch was dipped in the buffer, the reading took about a half hour to stabilize.

The sensor was also tested with other patches to check the variation in calibration between patches and the individual optrodes on the dual sensor. The means and standard deviations for the same were calculated.

The sensor used was named ‘A1’ and the 2 optrodes on it were ‘A11’ and ‘A12’. There were 4 pH patches (named C1, C2, D1, D2) that were calibrated alternately with both A11 and A12. The pH buffers 6.72, 7.35, and 7.87 were used for calibration. The calibrations for each patch for each optrode is tabulated below.

Patch, optrode	A11		A12	
	Slope	Intercept	Slope	Intercept
<b>C1</b>	3.13	6.49	2.78	6.49
<b>C2</b>	3.01	6.51	2.7	6.48
<b>D1</b>	2.85	6.55	2.69	6.48
<b>D2</b>	3.1	6.48	2.46	6.55
<b>Mean</b>	3.02	6.51	2.66	6.5
<b>Standard Deviation</b>	0.16	0.03	0.14	0.03

Table 4.3: Calibrations for each pH patch with each optrode

It was observed from the table above that the slopes for both optrodes vary, but the intercepts are almost the same. Numerically, the mean calibration considering all the calibrations done for

the patches and both optrodes is,  $y = 2.84x + 6.5$ , with standard deviations of 0.15 and 0.03 for the slopes and intercepts respectively.

The patches were then tested for variation in calibration due to autoclaving. Autoclaving involved placing the patches in the autoclave chamber for 45 minutes. The autoclave chamber heats to a temperature of 121<sup>0</sup>C at 1 atmospheric pressure. Autoclaving ensured that all the patches were biologically clean. Patches C2 and D2 were autoclaved and they were calibrated again with A11 and A22 using the same buffers. Table given below illustrates the calibrations before and after autoclaving.

	Patch	A11		A12	
		Slope	Intercept	Slope	Intercept
Before autoclaving	C2	3.01	6.51	2.7	6.48
	D2	3.1	6.48	2.46	6.55
After autoclaving	C2	7.4	4.09	6	3.97
	D2	8.69	4.23	5.62	4.47

Table 4.4: Calibrations before and after autoclaving pH patch sensor

It was observed that autoclaving the patch causes variations in the calibration. These variations were not numerically consistent either. This concludes that the sensor should be used with fresh patches instead of reusing older ones.

- ***DO calibration verification and statistics***

A new DO patch sensor was calibrated by calculating the phase difference between the blue and red LEDs for oxygen saturated in air percentages of 0%, 20%, 40%, 60%, 80%, and 100%. Phase offsets were calculated using Rhodamine B dye.

The channel was tested in water that was saturated with the respective gas mixture obtained by mixing air and nitrogen. The percentages were set using the ratios of the flow rates in a dual flowmeter. The DI water as well as the sensor were set in an incubator at 30<sup>0</sup> Celsius (to account for the temperature sensitivity of the oxygen dye). The water were stirred to achieve faster



equilibrium with the gas mixture. The data collection was started after the water-gas equilibrium was reached. Again, the data were collected at 30 seconds intervals. The calibration for the DO patch calculated using equation (4.1) was  $22.91x^2 + 22.77x$  and  $\tan \phi_0 = 0.994$  radians. After calibration, the same patch sensor was dipped in DI water with 20% air saturation bubbled in the solution at 30<sup>0</sup> C for 15 hours. The calibration verification data is as shown below.

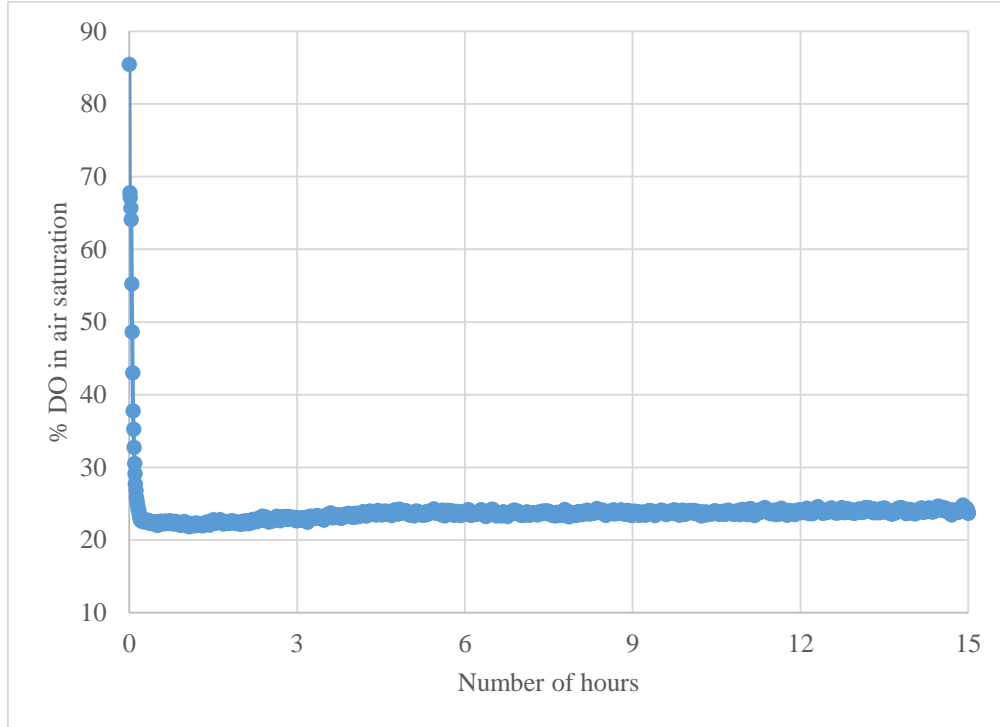


Figure 4.5: DO calibration verification

The average DO concentration recorded was 23.5% for air saturation, which is ~5% of DO concentration. The standard deviation is 0.6 % for air saturation and 0.12 % for DO concentration. Thus, DO concentration error is less than 1 %.

Same as the pH patches, the sensor was also tested with other patches to check the variation in calibration between patches and the individual optrodes on the dual sensor.

There were 2 pH patches (named W1 and P2) that were calibrated alternately with both A11 and A12. Calibration was done at 30<sup>0</sup> C. The calibrations for each patch for each optrode is tabulated below.

Patch, optrode	A11			A12		
	A	B	$\tan \phi_0$	Slope	Intercept	$\tan \phi_0$
<b>W1</b>	10.91	67.07	-1.67	12.39	71.02	-1.75
<b>P2</b>	12.93	72.66	-1.79	10.67	66.7	-1.74
<b>Mean</b>	11.92	69.865	-1.73	11.53	68.86	-1.745

Table 4.5: Calibrations for each DO patch with each optrode

It was observed from the table above that the values of the coefficients for both optrodes vary, but  $\tan \phi_0$  values are consistent. More experiments need to be conducted to determine a constant calibration for the DO patches.

#### 4.4 Standardization of Bioprocess Analysis Sensor System

- *pH standardization*

In lab-grade fluorometers, the excitation source is typically a high-power broadband lamp. For excitation, the light is passed through a wavelength selection device (monochromator, narrow band-pass filter). A small portion (~4%) is diverted and quantified for normalization of the measurement. This is necessary due to the drifts of the lamp intensity due to temperature, aging, etc. However, it is technically challenging to add additional optics and detectors in the small form factor of a sensor. Furthermore, the excitation side correction for a lab grade fluorometer is computationally intense and strains the resources of the low power micro-controller typically used in sensors. Finally, the LED intensity-light source of choice in the small, optical systems - is significantly more stable as compared with a lamp. With that in mind, we opted for correction by adjustment of the excitation LEDs intensity. Below we will discuss the theoretical base for such approach.

The intensity ' $I_F$ ' of a fluorophore when excited at a particular wavelength is given by,

$$I_F = \eta(I_{EX} - I_{TSM})\Phi \quad (4.2)$$

where,  $I_{EX}$  is excitation intensity,  $I_{TSM}$  is intensity of the excitation source that passes through but is not absorbed by the sample,  $\eta$  is the ratio of the average energy of emitting photons to that of the incident photons, and  $\Phi$  is the quantum yield [20], [2].

Applying Beer-Lamberts law, integrating over the entire excitation bandwidth, and approximating absorption profile to a line as generally acceptable for dilute dye solutions ( $\sim 10^5 M$ ) [2], we obtain the following expression for the fluorescence intensity  $I_F$ ,

$$I_F = 2.303\eta \int_{\lambda_S}^{\lambda_L} I_{EX}(\lambda) \varepsilon(\lambda) d\lambda \Phi \quad (4.3)$$

where,  $I_{EX}(\lambda)$  and  $\varepsilon(\lambda)$  are functions describing dependence of excitation intensity and the extinction coefficient on the wavelength, and  $\lambda_S$  and  $\lambda_L$  are respectively the shortest and the longest wavelength in the excitation spectrum that contribute to the detected fluorescence emission. The values for the functions and the wavelengths are different, but constant for the both excitation systems. Therefore, the value of the integral in equation (4.3) is constant and the fluorescence intensity obtained by the use of LED excitation is proportional to the normalized intensity obtained using a lamp. Furthermore, the goal is to measure not just the intensity, but the ratio of intensities  $R$  when the transducer is excited at two different wavelengths (i.e.  $\lambda_S$  and  $\lambda_L$ ). This ratio can be expressed by,

$$R = \frac{I_{F\lambda 1}^{Lamp}}{I_{F\lambda 2}^{Lamp}} = \frac{m_1 I_{F\lambda 1}^{LED}}{m_2 I_{F\lambda 2}^{LED}} \quad (4.4)$$

where Lamp and LED superscripts denote the excitation light source. It should be noted that for the LED excitation, two different LEDs with the respective emission maxima are used (they are not spectrally narrowed). Also,  $m_1$  and  $m_2$  are the proportionality coefficients for the respective LEDs and the lamp. These proportionality coefficients reflect the fact that the total intensity observed by the photodetector, according to equation (4.3), is actually the surface under the two respective curves as shown in the figure below. As the observed emissions vary both with the light source and the wavelength, separate proportionality coefficients are needed for each wavelength.

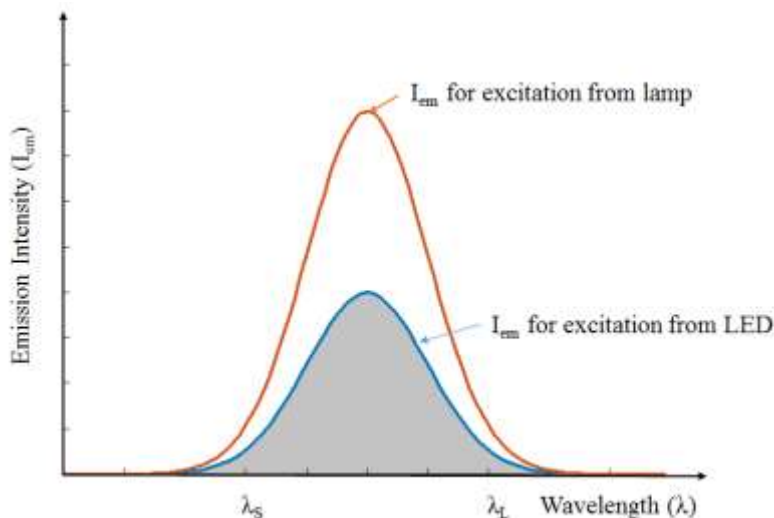


Figure 4.6: Emission spectra of a dye when excited with spectrally narrowed lamp or LED

The difference in the observed emission is less than an order of magnitude; in a lab-grade fluorometer, its monochromator selects a narrower wavelength range ( $\sim 5$  nm) from the spectrum emitted by the broad-band lamp, whereas an LED emits in a wider range of wavelengths ( $\sim 40$  nm), thus compensating for its lower intensity. Whichever the source, the emission spectrum is the same. Hence, it follows from equation 11 that if we can vary the fluorescent intensity resulting from LEDs excitation, it should be possible to equalize the ratio read by the lab-grade and the LED-based fluorometers. This is easily done by adjusting the current via the LED.

Standardization of the sensors in pH mode was performed using a solution of 0.2 mg of HPTS (8-Hydroxypyrene-1, 3, 6-Trisulfonic Acid, Trisodium Salt, Aldrich) in 20 ml of deionized water. The pH of the solution was adjusted to 11 using NaOH. The ratio of the fluorescence intensities at 455/405 nm was measured on a lab fluorometer (Cary Eclipse, Varian) and was found to be 1.35. The solution was placed in a beaker and optical fibers (without the sensors) were positioned sideways to the beaker touching its wall. The beaker was placed on a black non-fluorescent surface (standard lab bench; if needed, a stand made of black ABS or Delrin can be used).

First, the fluorescence was excited using the 405 nm LED. The measured voltage resulting from fluorescence was adjusted to be 50% of the ADC range by varying the intensity of the 405 nm

LED. Then, the fluorescence was excited using the 460 nm LED. By changing its intensity, the ratio of the blue/violet intensities was adjusted to the same ratio as measured by the benchtop fluorometer. Four different units were calibrated in this way 3 single channel units and one dual channel unit. The achieved difference in the measured ratio was less than 1%. The values of the current for the required brightness is stored in the flash memory of the SOC.

Next, the system with the pH sensors were calibrated using 6 different pH buffers: 5.87, 6.45, 6.77, 7.44, 8.08 and 8.86. Before the measurements, the sensors were hydrated in deionized water overnight at room temperature. The pH sensor was immersed in the buffer and the reading was recorded for a period of 10 minutes with an interval of 30 seconds between the measurements. The average value over these measurements was accepted as system reading. The results of the calibrated sensor systems are shown in Figure 4.7.

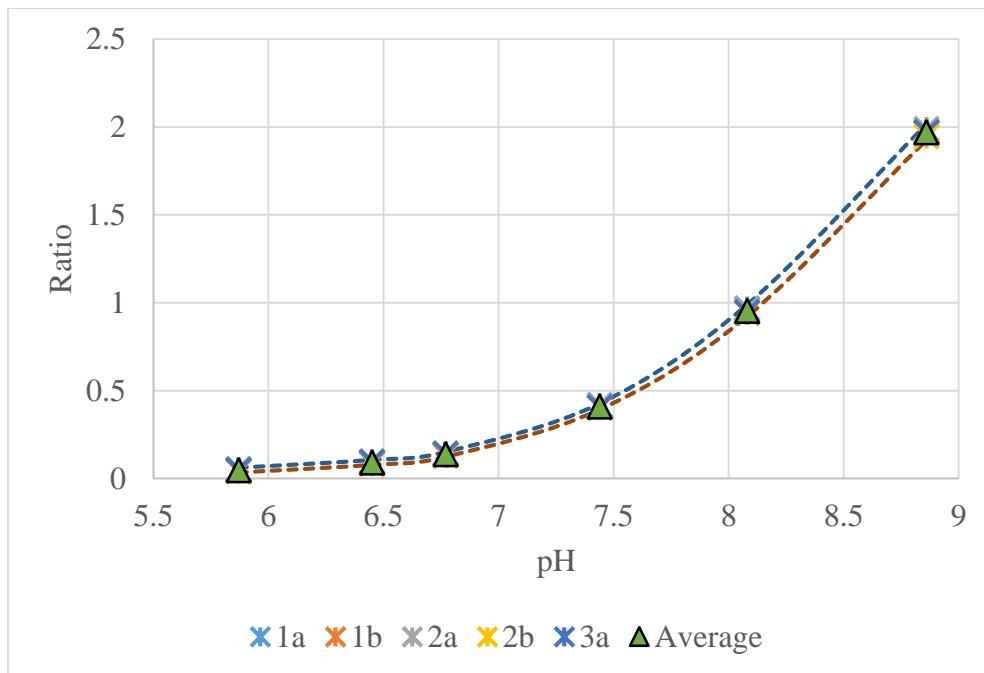


Figure 4.7: Standardization of pH patch for sensors 1a, 1b, 2a, 2b, 3a. Dotted lines represent confidence interval for  $\pm 3\sigma$  error

The standard deviation of the measurement within a single sensor channel was 2.61% at the lowest pH and gradually decreased to 0.15%. In the physiological range - pH 7.44 the standard

deviation of within a single device was 0.32%, which resulted in resolution of  $\sim 0.0037$  pH for a single device with the use of the pre-calibrated patch. The confidence interval of the measurement was 6. When the same patch was used across all the devices, the standard deviation reached 3.06%. The bigger variation between the devices as compared with the standardization results was due to the differences in the patch positioning relatively to the light sources we are using big diameter (2mm) optical fibers, and the size of the LED chip is  $\sim 0.5 \times 0.5$  mm. This results in somewhat uneven patch illumination from the LEDs. The bigger variation resulted in a resolution of 0.068 pH, again with confidence interval of 6. As resolution that is better than 0.1 pH unit is deemed sufficient for use in bioprocesses, this accuracy allows for use of any of the units in monitoring of fermentations and other bioprocesses.

- ***DO standardization***

For DO mode, the sensors are excited and read at single wavelength; therefore, no emission or excitation side spectral correction is needed. However, it is still needed to correct for any additional phase shifts that are introduced by the light source and detection electronics. Due to very high transimpedance amplification, analog amplifiers introduce significant phase shift in the measured signal. Therefore, a procedure to measure and subtract the phase offset was developed. It relies on the use of 'zero decay time constant' fluorophore.

In essence, this is a fluorophore with a decay time that is 3 or more orders of magnitude shorter than the sensing fluorophore, but with similar spectral characteristics. The minimum phase shift of the oxygen sensing fluorophore (RuDPP) is  $\sim 20^\circ$ . Hence, it follows from equation (2.4) that the phase shift of a fluorophore with a decay constant that is 1000 times shorter will be less than  $0.04^\circ$ , which is below the detection limit of the electronics. Therefore, any observable phase shift with this fluorophore is resulting from the electronics and should be subtracted.

The standardization in DO mode was performed using a solution of 1 mg Rhodamine B in 20 ml of water. The resulting offset phase was recorded, and subsequently subtracted from the measured phase of the optical sensor. The average phase offset of the boards was  $22^\circ$ . The values of the offsets are stored in the memory of the SOC for subsequent use.

Next, the five channels of the systems were calibrated using the same DO sensor for DO percentages of 0%, 20%, 40%, 60%, 80%, and 100% of air saturation. The channels were tested in water that was saturated with the respective gas mixture obtained by mixing air and nitrogen. The percentages were set using the ratios of the flow rates in a dual flowmeter. The water solutions as well as the sensor were set in an incubator at 37<sup>0</sup> Celsius in order to account for the temperature sensitivity of the oxygen dye. The solutions we also stirred to achieve faster equilibrium with the gas mixture. The data collection was started after the water-gas equilibrium was reached. Again, the data were collected for 10 minutes at 30 seconds intervals and the values were averaged. The calibration results are presented in Figure 4.8.

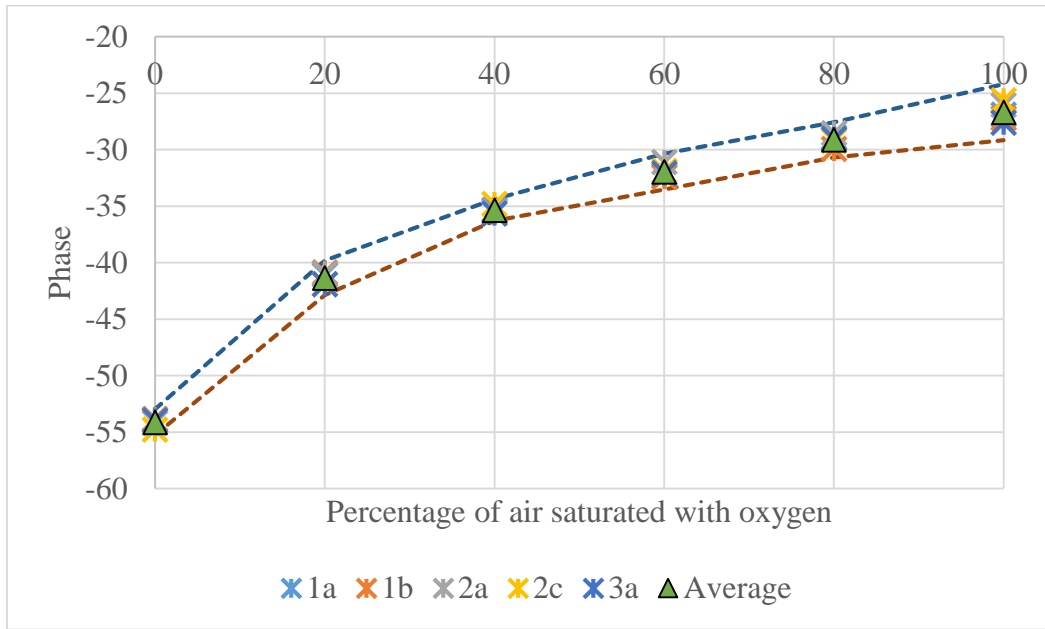


Figure 4.8: Standardization of DO patch for sensors 1a, 1b, 2a, 2b, 3a. Dotted lines represent confidence interval for  $\pm 3\sigma$  error

The standard deviation of the measurement within a single sensor channel was 1.14% at the highest oxygen concentration and gradually decreased to 0.25% when oxygen concentration dropped to 0. This corresponds to resolution of 2% at air saturation and better than 0.5% of air saturation when the oxygen concentration approaches zero. The confidence interval of the measurement was 6. When the same patch was used across all the devices, the standard deviation

reached 6.69% at 100% of oxygen saturation. We attribute the higher error in oxygen measurements to the measurement setup, where we had to open and close the incubator door to and move the vessel to position it on multiple photometers. Unlike the pH chemistry, the oxygen sensor has sensitivity of  $\sim 4\%$  per  $^{\circ}\text{C}$ ; furthermore, movement easily changes the level of the dissolved gas in the vessel.

#### 4.5 Temperature Coefficient for DO Measurement

The fluorophore in RuDPP dye used in the DO patch is temperature sensitive. An experiment was conducted to try and determine a temperature coefficient for the DO patch sensor which would enable the user to calibrate the patch sensor at room temperature and extrapolate the data to get a calibration at the temperature needed.

In this experiment, 2 DO patches were calibrated against both the channels of a dual channel optical sensor at  $30^{\circ}\text{C}$ ,  $35^{\circ}\text{C}$ , and  $40^{\circ}\text{C}$ . The nomenclature for this experiment is the same as that of the DO calibration statistics. Figure 4.9, Figure 4.10, Figure 4.11, and Figure 4.12 show the plots for each patch against each sensor at different temperatures.

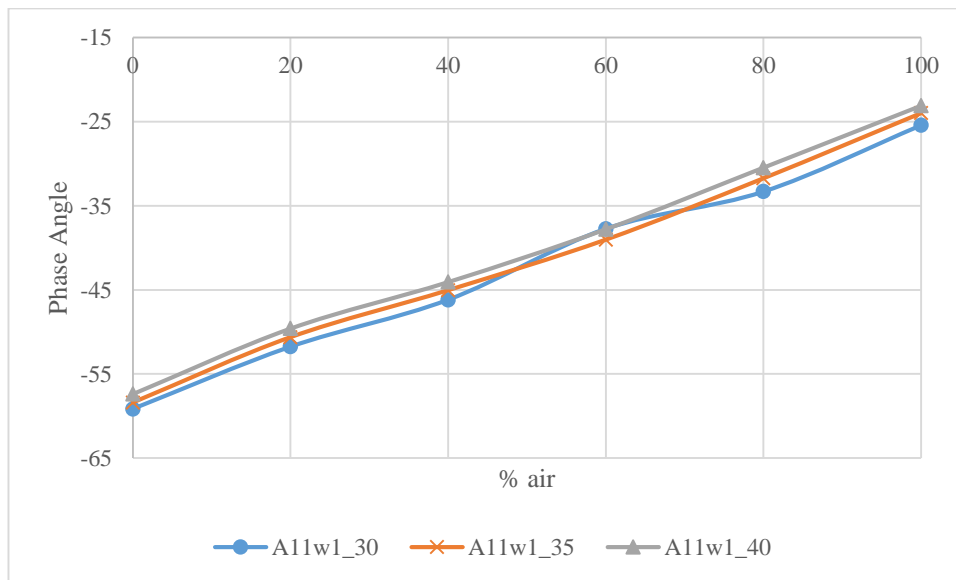


Figure 4.9: Plot for DO patch w1 on channel 1 of sensor A1



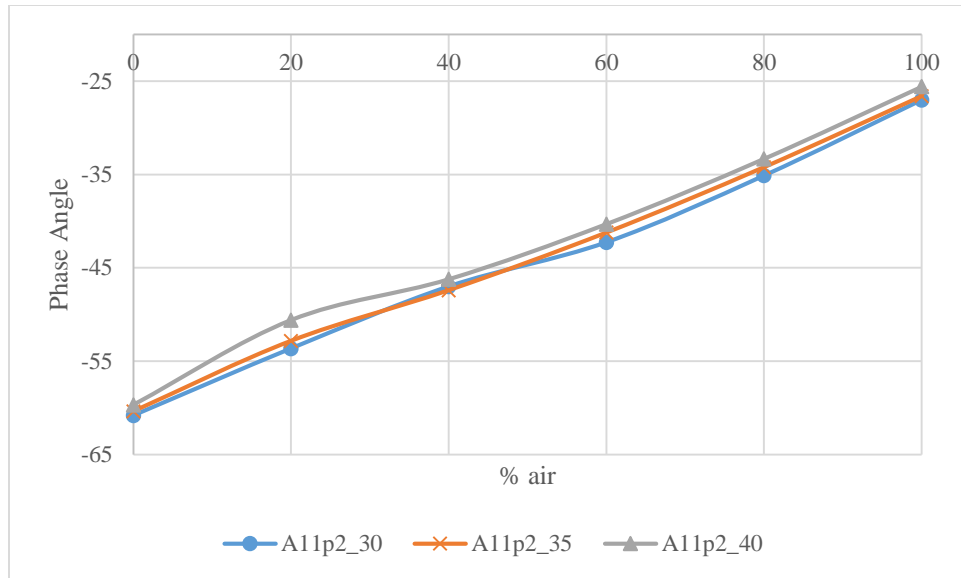


Figure 4.10: Plot for DO patch p2 on channel 1 of sensor A1

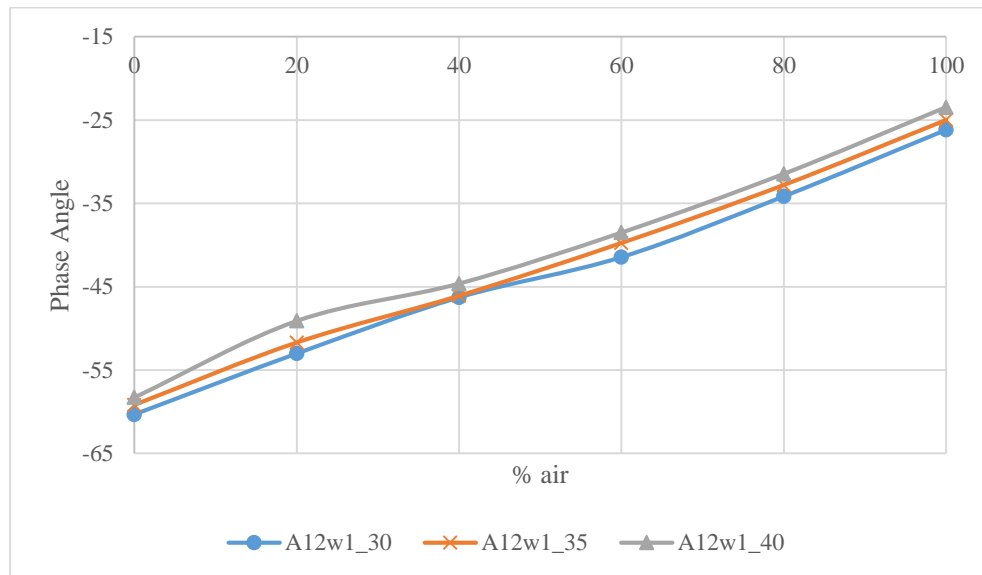


Figure 4.11: Plot for DO patch w1 on channel 2 of sensor A1

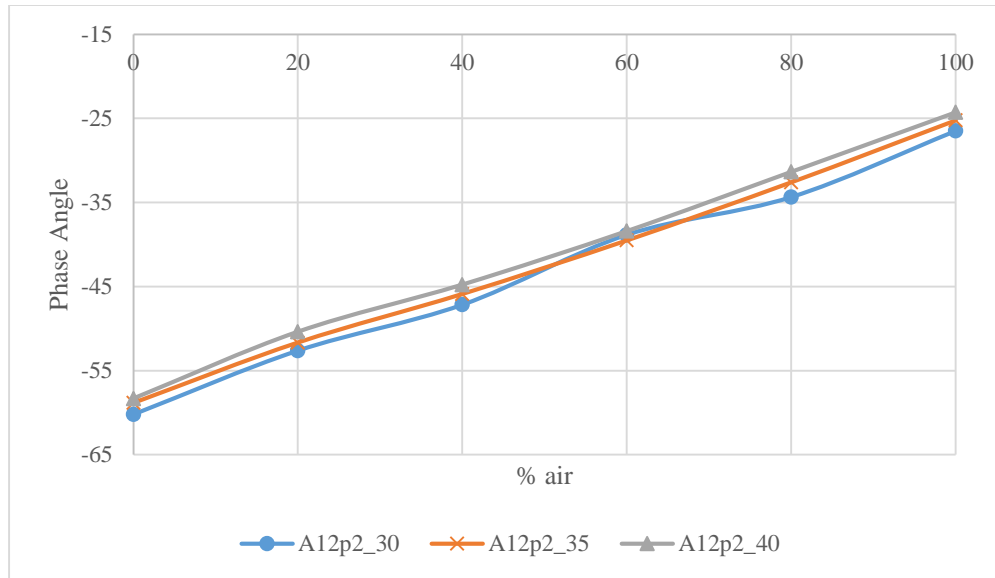


Figure 4.12: Plot for DO patch p2 on channel 2 of sensor A1

All plots show a consistent increase in phase angle with increase in temperature. There is an average increase of  $1^{\circ}$  phase angle for the sensor per  $5^{\circ}$  C. The error observed when considering this coefficient is  $\sim \pm 38\%$ . Further tests need to be done to further validate this data and to derive a more stable and robust temperature coefficient. Care has to be taken to maintain temperature, and maintain concentration of DO in the DI water. This will aid in the reduction of the error for the temperature coefficient.

## 4.6 E. Coli Experiment

To verify the ability of the sensor to operate under the conditions of an actual bioprocess, it was used to monitor pH and DO in an E. coli cell culture for 25 hours, which was placed in an incubator. The flask in which the cells were cultured was shaken at 150 rpm at 37°C. The overnight seed culture consisted of a 0.5% (10mL) inoculum of E. coli strain BL21(DE3) frozen stock in LB media (Fisher Scientific, Catalog number MP113002142) incubated at 37°C with shaking at 250 rpm [7]. The cell culture was then started in another flask by adding 10% seed culture to the media. Optical density value representative of the bacterial growth was measured online with a Hewlett-Packard 8452A Diode Array spectrophotometer at 600 nm and was observed to be 0.343 for the passaging flask [7].

The optrodes were first sterilized with 70% ethanol. Then, the patch sleeves were put on the probes. These sleeves were cleaned by dipping them completely in sterile deionized water for 30 minutes. The cell culture was continuously stirred using a magnetic stirrer. The probes were dipped in the culture such that the patches were completely submerged. The entire setup was placed in an incubator at 37°C. Data for pH (on optrode 1) and DO (on optrode 2) was logged every 15 seconds as shown in Figure 4.13.

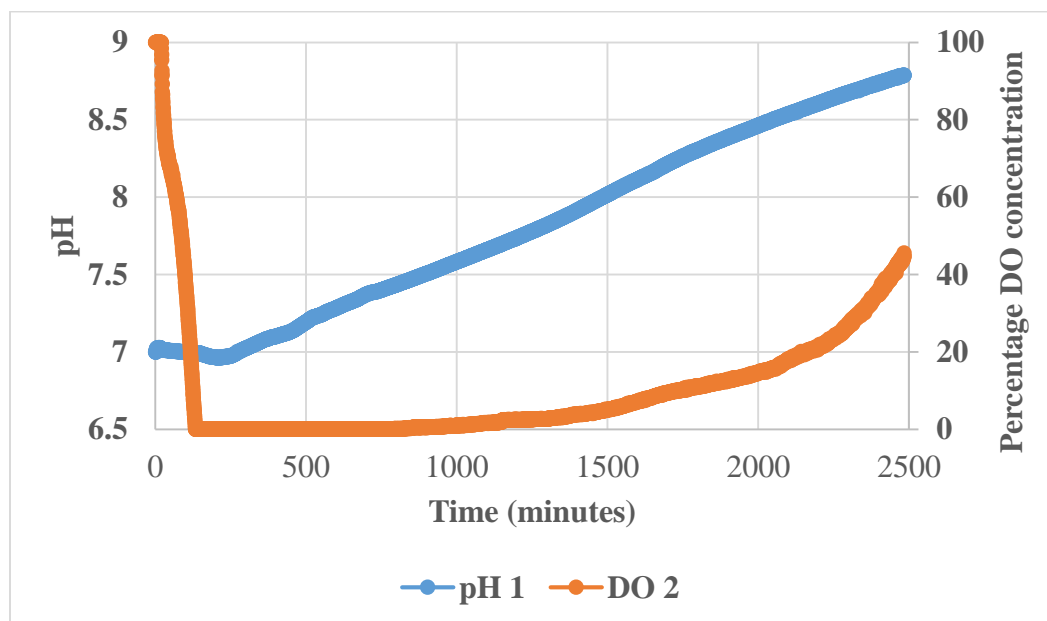


Figure 4.13: pH and DO profiles for E. Coli over 25 hours

Figure 4.13 illustrates the profiles observed for pH and DO in the E. Coli cell culture over a period of 25 hours using the presented sensors. The typical patterns of pH and DO profiles were observed clearly with the optical sensor. Oxygen depletion occurs during the exponential growth of the culture, with gradual recovery of the DO at the end of the process [7]. The pH slightly drops during the exponential growth, but with the beginning of the stationary phase it continuously rises, consistent with the continuous lysing of the cells. These profiles are very similar to the profiles usually obtained with electrochemical sensors.

#### 4.7 Bioreactor Lysate Run using BASS to Measure pH And DO

Once the patches were verified, the optical sensor was used in an actual bioreactor run. For run 382k14, minibioreactors B2 and C3 were monitored using the DO and pH optrodes respectively. Figure 4.13 illustrates the bioreactor setup.

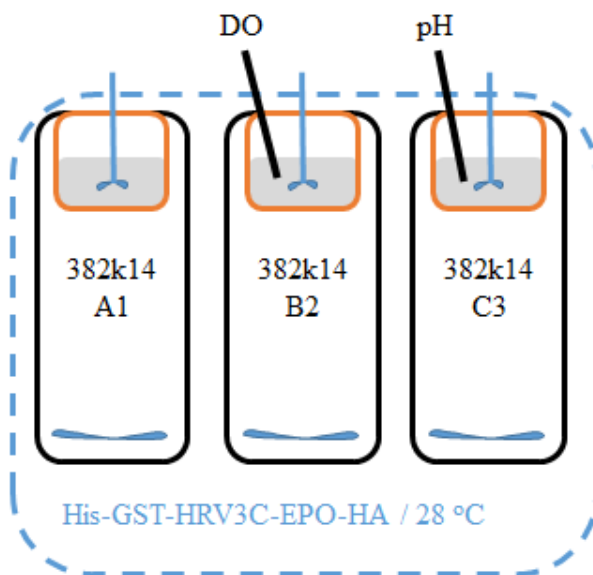


Figure 4.14: Bioreactor setup for run 382k14

The bioreactor setup shows that DO is measured in bioreactor B2 and pH is measured in reactor C3. These bioreactors were set to express Erythropoietin (EPO). The expression lasted for 4 hours. The measurement starts at 11:02 am. DNA is added to the lysate at 11:45 am. The pH and DO profiles for the run are as shown in Figure 4.15.

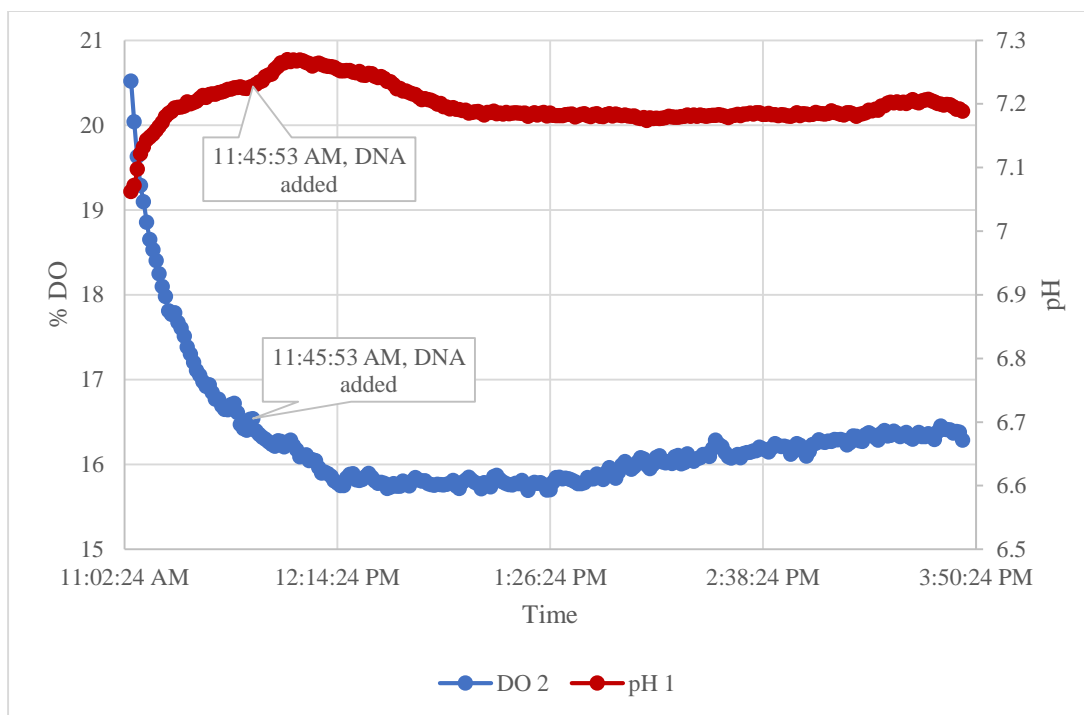


Figure 4.15: pH and DO profiles for bioreactor run 382k14

The pH and DO profiles indicate that the sensors do function without failing in the lysate. The pH in the lysate increased from 7.06 to 7.26 initially, and then stabilized at 7.18. There was a small rise in pH profile with a peak at 7.2 at the end of the run. The DO profile gradually decreases from complete saturation to about 80% air saturation (15% DO concentration) and stays stable at these values.

Bioreactor	Average Abs (450-600)	EPO mIU/ml	Comments
A1	1.14	104491	No probe
B2	0.65	59578	DO optrode
C3	0.65	59578	pH optrode

Table 4.6: Yield of EPO in each bioreactor

Table 4.6 shows the amount of protein (EPO) expressed at the end of the run. It can be seen that the reactor with probes in them had a lesser yield compared to the reactor with no probes. A

possible conclusion as to why this happened was the cleaning procedure observed for the probes before starting the run.

More data needs to be collected by the sensor in protein expressions runs to be able to determine the authenticity of pH and DO profiles for the same. This single run however, ensures that the data collected from the optical sensor is does not drift. The optical nature of data collection makes certain that there is no protein build up within the optrode (like that in the microelectrodes). This, in turn, makes the optical sensor a valuable process analysis tool for protein expression.

#### ***4.8 Summary***

BASS was validated for measurement of pH and DO as variables. Chemical patch sensors for pH and DO were calibrated. The calibration was verified. The sensor system was standardized such that multiple systems would log the same raw data for specific pH and DO. A temperature coefficient for DO patches was derived. BASS was validated in an E. Coli growth culture for pH and DO. Finally, the system monitored pH and DO in a protein production run for expressing Erythropoietin (EPO). This experiment proved that BASS could be utilized to monitor in in-vitro protein production systems without failing.

## **Chapter 5. TESTING AND VALIDATION FOR GREEN FLUORESCENT PROTEIN (GFP)**

GFP or Green Fluorescent Protein exhibits green fluorescence when exposed to light in the ultraviolet to blue spectrum. This protein was first isolated from a jellyfish in the 1960s and 1970s. Since then, it has found multiple applications as a biomarker, a reporter gene, in fluorescence spectroscopy and microscopy, among others. For example, as a biomarker, GFP is used for tagging whole cells – e.g. neurons are tagged to track brain activity, etc. [14]. GFP can be used as a biomarker for cell-free protein production to visually track expression and purification, exciting the sample with UV/blue light.

GFP is termed as a ‘surrogate marker’ for quantification of target protein. The DNA is genetically engineered by inserting a GFP DNA sequence next to the target protein sequence such that when the protein is expressed, the peptide chain ‘folds’ into the target protein structure along with the GFP structure attached to it. There is a fixed ratio between the target and the number of surrogates attached to it.

The optical sensor described in the earlier chapters is designed to measure green fluorescent emissions with blue excitation. The same sensor could be used to measure green fluorescence that these ‘GFP-biomarked’ proteins would emit, by using the optrode as is (without any patch sensors), enabling real-time monitoring of protein expression and purification.

When the optical sensor is used as a GFP sensor, sample is excited with blue light with 10 kHz modulation. GFP has a maxima at  $\lambda = 510$  nm with blue excitation [13]. The single core plastic optical fiber is used as a pathway for the blue excitation and green fluorescent emissions. There are no changes in the sensor instrumentation.

GFP was also used as a demonstration protein for the Bio-MOD system. Hence, all the experiments were done targeting GFP as an individual protein. GFP ‘tagged’ to the target protein is a future research goal for the protein production team.



The sensor undergoes the same testing and validation as pH and DO. It is first calibrated, then its calibration is verified. It is then tested in a real-time GFP expression process. A fixed length extension is modelled and implemented as a solution to variable path length. Rate analysis is done to further analyze the process of protein production.

### ***5.1 Calibration and Verification of GFP Sensor***

- ***Calibration***

The optical sensor was calibrated using GFP standard (88899, Thermo Scientific), spiking it to 2X dilution with CHO lysate (1863067, Thermo Scientific). GFP standards are already available GFP samples with known concentrations. The lysate was added so that the optical sensor and the lab-grade fluorometer, the Spectromax (M5, Molecular Devices) could be calibrated considering the background fluorescence of the lysate. Readings from the Spectromax are considered as standards readings. A 96 well black-walled clear-bottom micro-well plate was used for the calibration and run.

There were a total of 6 samples of known GFP concentration that were used for calibration. Figure 5.1 illustrates the arrangement of the samples in the well plate along with their concentrations. Each well had a volume of 100  $\mu$ l. Serial dilution was performed with 1X PBS buffer for getting the desired concentrations.

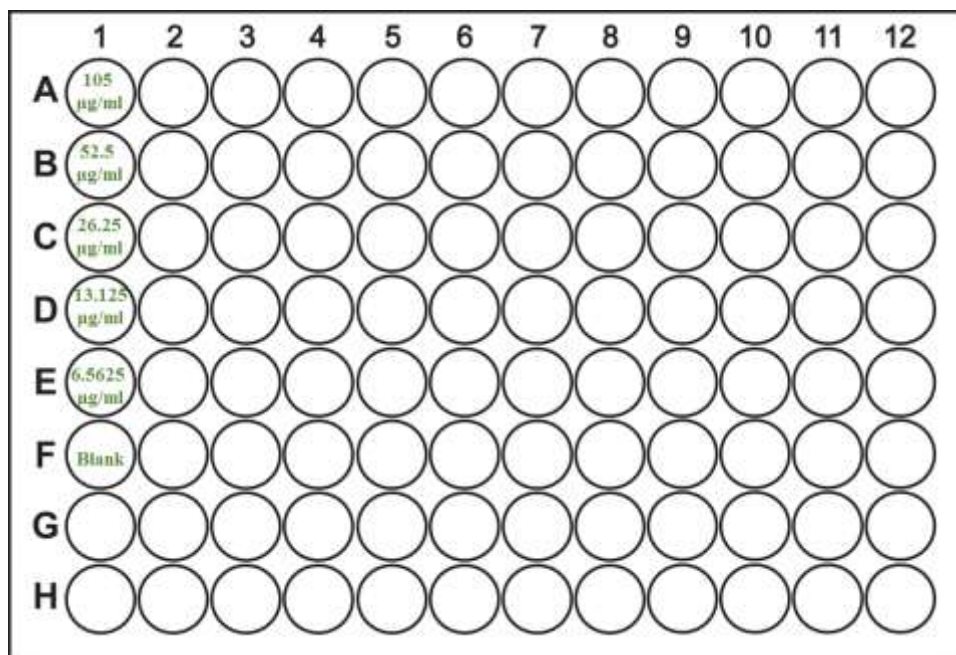


Figure 5.1: Arrangement of standard samples in 96 well plate with concentrations

The optical sensor was arranged as shown in Figure 5.2 for calibration. The sensor was setup such that it reads from the bottom of the plate, just as in the Spectromax. As the aim of this experiment is to verify that the sensor reads concentrations to a certain accuracy, the apparatus is arranged in a similar way, so that the only variables involved are the concentration of GFP. Moreover, immersing the fiber in the sample would compromise the reading as the sensor is not reading all the fluorescence generated by the sample.

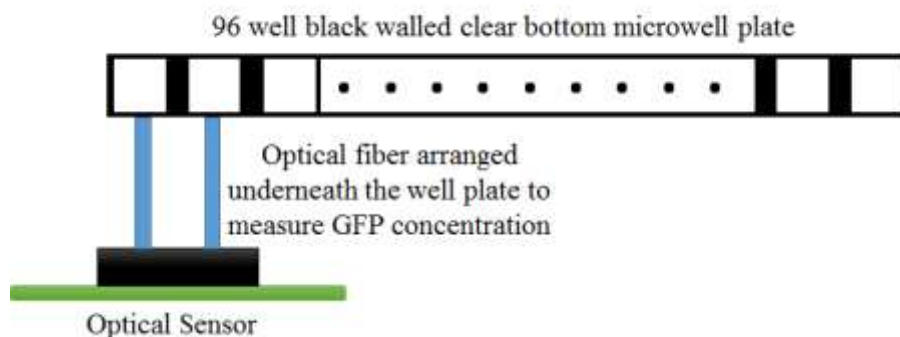


Figure 5.2: Setup for calibration of optical sensor and for actual GFP run

Calibration for the Spectromax and the optical sensor are as shown in Figure 5.3 and Figure 5.4. It should be noted that the optical sensor used has 2 fibers, which are named A21 and A22 respectively. Thus, one sensor board (A2) houses 2 optrodes, A21 and A22. The Spectromax, A21, and A22 have  $R^2$  value greater than 0.99 implying linearity.

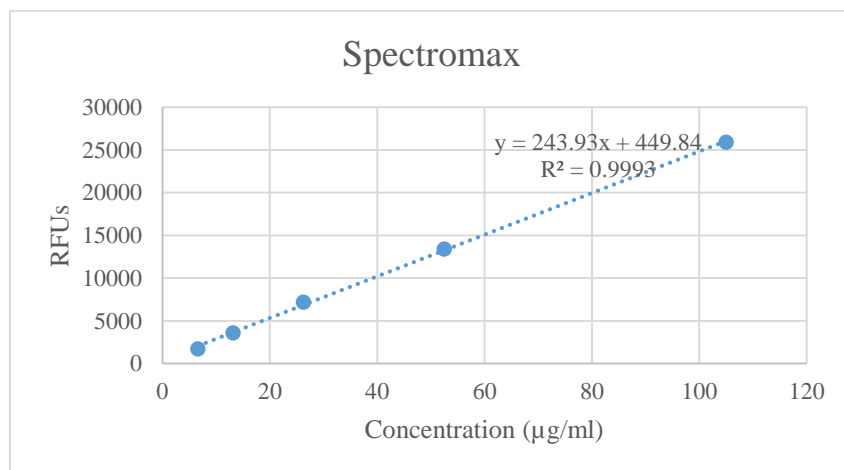


Figure 5.3: Calibration for Spectromax

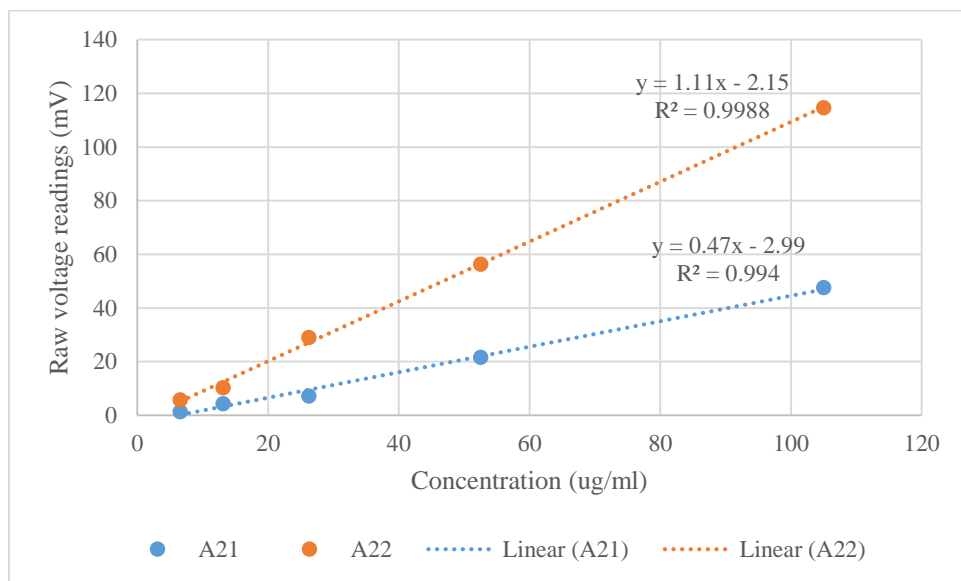


Figure 5.4: Calibration for GFP sensors A21 and A22

To validate the calibration, a GFP expression run was conducted in a 96 well plate. As shown in Figure 5.2, the GFP sensor measured in the same configuration every 30 seconds, for 15 hours. Following section explains how the GFP expression run was set.

- ***Setting up the GFP IVT (In-Vitro Translation) reaction:***

The IVT reaction was set up in a black walled clear bottom 96 micro-well plate. Lyophilized CHO lysate (1863067, ThermoScientific) was reconstituted by adding Nuclease Free Water (NFW) to the IVT lysate. Accessory Proteins (1862722, ThermoScientific) were added, and this mixture was left ‘standing’ under the HEPA filter laminar hood for 15 minutes. After the 15 minutes, reaction mix (UMRM0723205, ThermoScientific) and NFW were added. 100  $\mu$ l of this mixture is considered as the blank and is added to one of the wells of the plate. To the remaining mixture, DNA (pT7CFE-tGFP-His, ThermoScientific) for GFP was added. Two black walled clear bottom 96 micro-well plates were used to hold the samples for the GFP optical sensor and Spectromax.

- ***Calibration Verification***

The GFP optical sensor was arranged such that the optrodes were flat against the base of the well containing the sample, as shown in Figure 5.2. The sensor then read the green fluorescent emissions for blue excitation every 30 seconds. The LEDs were set to run at 40 mA. This entire setup was kept in an incubator to maintain the temperature at 30<sup>0</sup> C. The run was set for 12 hours.

Another 96 well plate was kept in the Spectromax. The well had 5 GFP samples and 1 blank sample (lysate mix without DNA). Volumes of all these were 100  $\mu$ l. The Spectromax was also set at 30<sup>0</sup> C, and it read data every 5 minutes. Before every reading, the samples were shaken for 5 seconds. This run was also set for 12 hours.

The Spectromax data was considered as the standard. Figure 5.5 illustrates the GFP expression profiles and the blank profile from the respective wells in the well plate. It is observed that the expression plateaus after 7 hours, implying no further protein production.

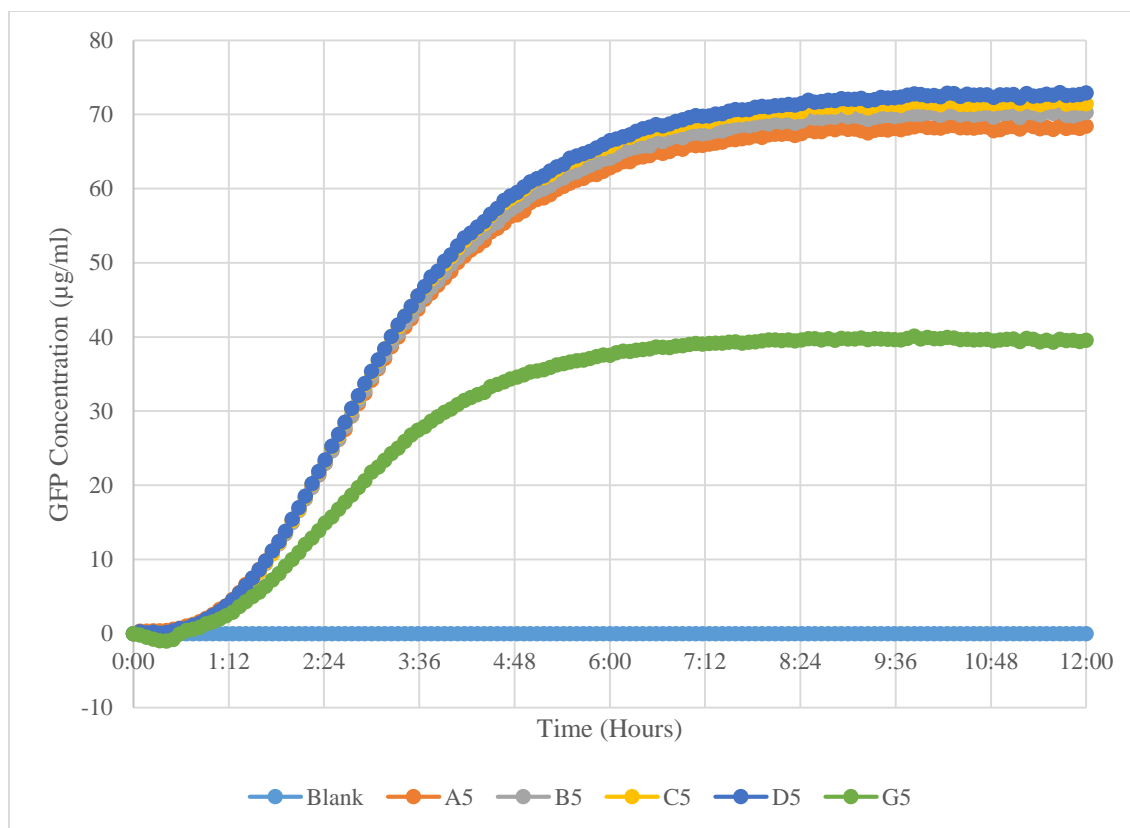


Figure 5.5: Real-time GFP expression in Spectromax

Samples from wells A5, B5, C5, D5, and G5 produce 68.7  $\mu\text{g/ml}$ , 70.5  $\mu\text{g/ml}$ , 72.1  $\mu\text{g/ml}$ , 73.1  $\mu\text{g/ml}$ , and 40.1  $\mu\text{g/ml}$  of GFP respectively. Since this is a biological reaction, protein concentrations per sample will vary even though the same procedure was followed for all samples. Hence, on an average, 64.9  $\mu\text{g/ml}$  of protein was expressed.

The GFP optical sensor GFP expression profiles are shown in Figure 5.6. Sensor A21 and A22 detect 53.6  $\mu\text{g/ml}$  and 60.1  $\mu\text{g/ml}$  of GFP. An average of 56.85  $\mu\text{g/ml}$  of GFP was produced.

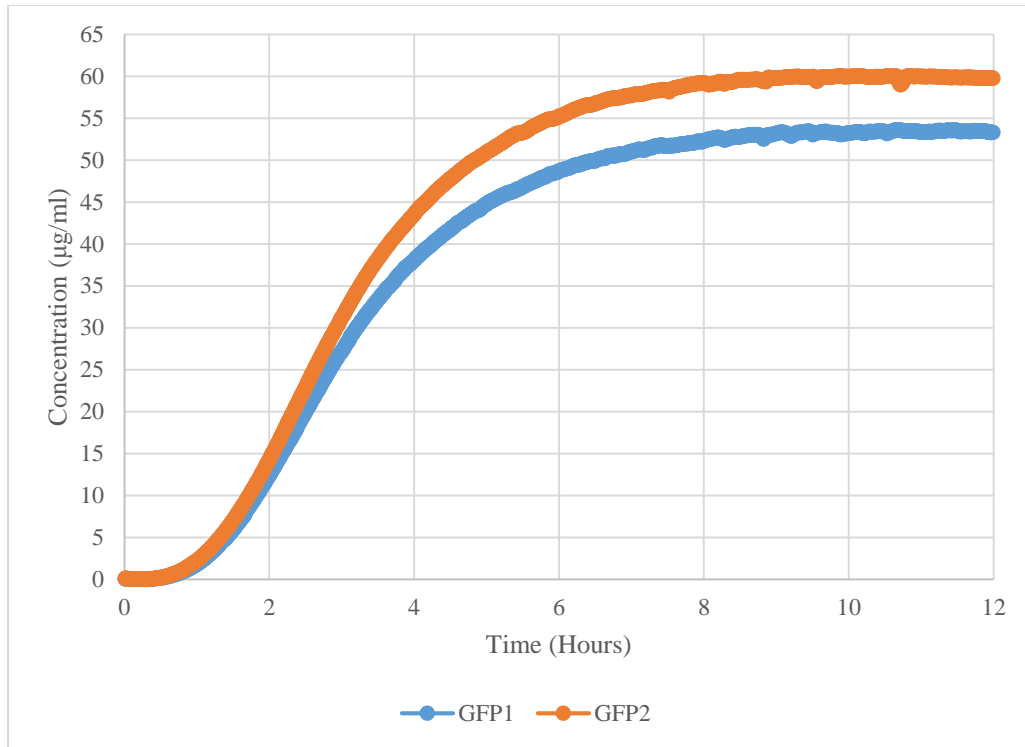


Figure 5.6: Real-time GFP expression in GFP optical sensor

From Figure 5.5 and Figure 5.6, it was observed that the concentrations detected for the same GFP expression vary by 12.4%. This error can be considered, if concentration is needed for an estimated guess. More experiments (triplicate/pentaplate runs) need to be conducted to validate sensor calibration. The sensor can still be used to track the profile to determine end of expression process.

## ***5.2 GFP Fixed Length Extension (GFP-FLE)***

The GFP sensor was used for calibration and verification externally. However, certain settings did not allow for it to be used so. Figure 5.7 presents how the GFP sensor is used by dipping the optrode in the bioprocess to measure its fluorescence intensity. It was observed that in this setup, external monitoring was not possible.

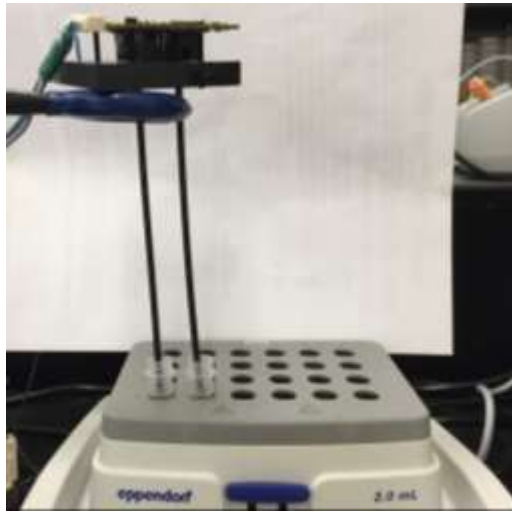


Figure 5.7: Use of GFP sensor by submerging optrode in GFP sample

In such an arrangement, a change in the height at which the optrode was dipped affects the readings logged by the sensor. This is illustrated in Figure 5.8.

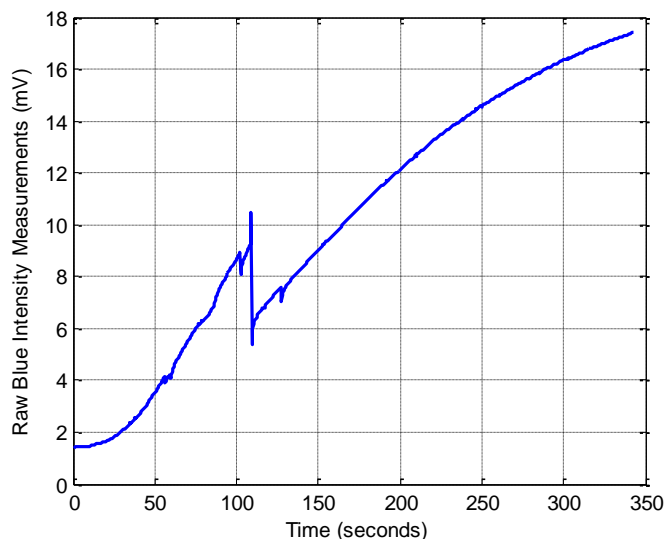


Figure 5.8: Anomaly in measurement due to variation in depth at which optrode is submerged

It was observed that there is a 33.33% drop in the blue intensity reading when the optrode was shifted (by accident or otherwise) along the length of the container. This compromised the measurements, and an error correction was needed to be performed to get rid of the anomaly. The problem arose from the variation in lengths of the fluorescence emission path. To prevent this, an extension needed to be designed such that the length of the emission path was fixed and the depth at which the optrode was dipped in the bioprocess did not affect the measurements. This extension was termed a ‘Fixed-Length Extension’ or FLE.

The basic principle behind the design of this extension was to place a non-fluorescent surface at a specific length ‘ $l$ ’ from the end of the fiber. This would result in only a fixed amount of emissions being detected by the fiber. Since the field of view of the fiber was constant, movement of the optrode along the length of the container would not affect measurements. The design of the extension is illustrated in Figure 5.9.



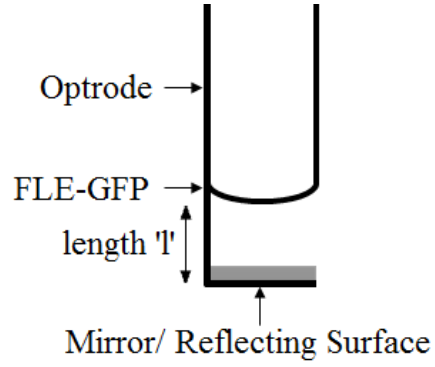


Figure 5.9: GFP-FLE design

The aim of the extension was to capture maximum emission intensity. The GFP-FLE was modelled using MATLAB to determine ideal parameters. The variables considered in this derivation were length ' $l$ ' and concentration ' $C$ '.

- ***Theoretical modelling of GFP-FLE***

Assume that one single GFP molecule is present along the axis of the optrode that is to be detected. This molecule would act like a point source for its fluorescent emissions. The blue LED excitation beam exits the fiber and gets absorbed by the GFP molecule. Within a timespan of a few nanoseconds, the energy is re-emitted as green fluorescence, which is coupled back to the fiber. The acceptance angle for these emissions is  $60^\circ$  [34]. The single GFP molecule will have a spherical emission profile as shown in Figure 5.10.

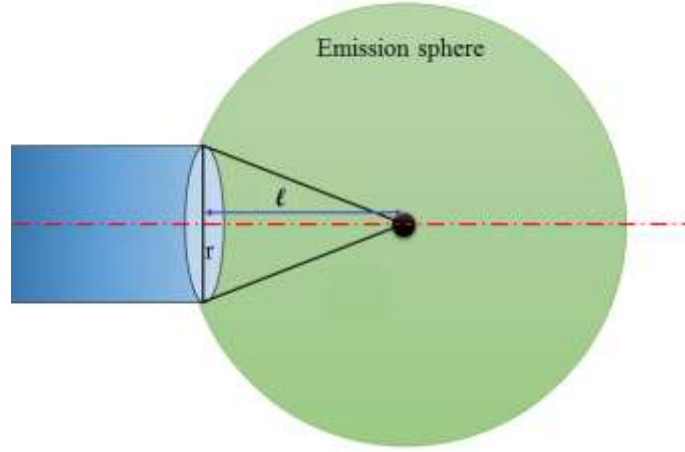


Figure 5.10: Fluorescent emission for one GFP molecule

Consider the emission sphere for the GFP molecule till it reaches the fiber tip as shown in Figure 5.10. The radius of the optrode is ' $r$ ' and the GFP molecule is at a distance ' $l$ ' from the fiber along its axis. According to Beer-Lambert's law, excitation and emission fluorescent intensities are given by [20];

$$I_{ex} = 10^{-\varepsilon Cl} \quad (5.1)$$

$$I_{em} = 10^{-\varepsilon Cl} \quad (5.2)$$

where  $l$  is length along axis at which GFP molecule is present (path length),  $C$  is concentration of GFP molecules (which is 1 in this case), and  $\varepsilon$  is the molar attenuation coefficient, (0.021 mm<sup>2</sup>/mole for GFP), and  $Q$  is the quantum yield for GFP which is 0.77 [20] [35].

From Figure 5.10, it is observed that only a conical part of the emissions sphere is reaching the fiber. The emission intensity that the optrode detects is this conical fraction. Thus,

$$I_{em1} = Q I_{ex1} \frac{\text{surface area of fraction of sphere in fiber}}{\text{surface area of sphere}} \quad (5.3)$$

$$I_{em1} = Q I_{ex1} \frac{R-l}{2R} \quad R = \sqrt{r^2 + l^2}$$

where,  $r$  is the radius of the optical fiber (1 mm in this case), and  $R$  is the radius of the emission sphere. The profiles of excitation and emission intensities for one GFP molecule along the axis with length from fiber varying is as shown in Figure 5.11.

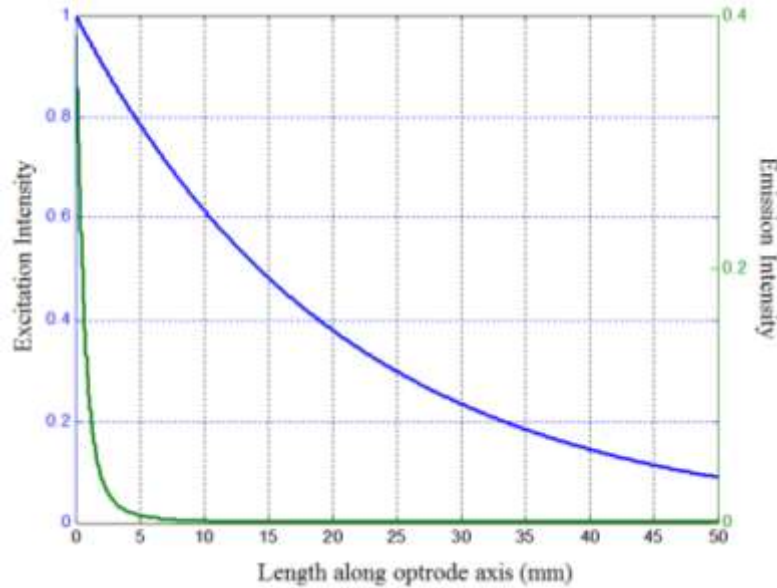


Figure 5.11: Excitation and emission profiles for one GFP molecule at varying length along optrode

It was observed that the emission intensity decreased rapidly along the length. It reached zero at approximately 5 mm for one GFP molecule. For all the GFP molecules along the axis, the total emission intensity would be the sum of all the individual molecule intensities. This principle could be extended to all the GFP molecules in the acceptance cone of the fiber. But these GFP molecules would have different  $R$  and  $l$  values.

To numerically approximate the emission intensity equation, we sliced the acceptance cone along the X axis at equal length  $L$  such that  $L \rightarrow 0$ . Hence, it could be assumed that the GFP molecules in each slice were at an equal distance from fiber. Thus, the emission intensity of each slice was the sum of the emission intensities of each GFP molecule in that slice. Slicing of the acceptance cone is shown in Figure 5.12.

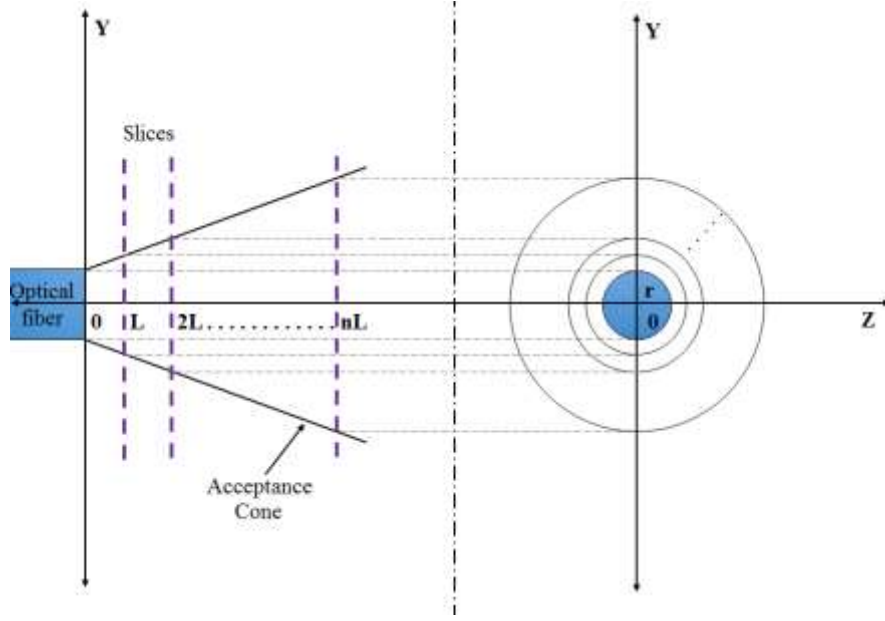


Figure 5.12: Front and side view of slicing method

Consider the first slice. Assume the GFP concentration is constant at  $0.5 \mu\text{g/ml}$ . The distance of slice 1 from the optical fiber is  $L$  mm. Hence excitation intensity is given by,

$$I_{ex}^{s1} = 10^{-\epsilon C L} \quad (5.4)$$

Figure 5.13 illustrates how the emission intensities are calculated along the first slice. Only a fraction of the emission sphere of the molecule contributed to the emission intensity detected by the fiber. Assume that the emission intensity at the arc of the fraction of the sphere was superimposed on the actual end of the fiber. The range for emission is from the center of the fiber (along the axis) till the point at which the slice intersects with the acceptance cone.

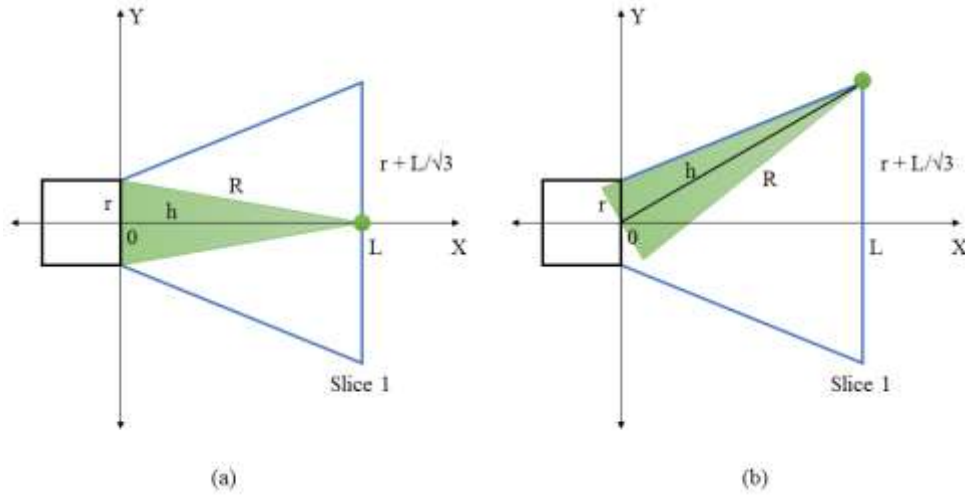


Figure 5.13: Mathematical illustration for slice 1 of acceptance cone

Figure 5.13 illustrates how the limits for GFP fluorescence intensity are determined along the diameter of the slice. Since the fiber is symmetric along its axis, the emission profile along the positive Y axis was determined, and then mirrored along the negative Y axis. Thus, the emission limits were emissions from the GFP molecules at  $(L, 0)$  and  $(L, r+L/\sqrt{3})$ . The varying heights 'h' had a range of  $\left[ L \leq h \leq \sqrt{L^2 + \left(r + \frac{L}{\sqrt{3}}\right)^2} \right]$ . The emission intensity for the GFP molecules lined up along the diameter of the first slice is given as follows:

$$I_{em}^{s1} = Q I_{ex}^{s1} \frac{R-h}{2R}, \quad R = \sqrt{r^2 + h^2} \quad (5.5)$$

The emission intensities at the center and both ends of the slice predetermined. By varying  $h$  and hence  $R$ , the profile of intensity along the radius of the fiber could be determined. Assume  $L = 0.1$  mm, the radius of the fiber  $r = 1$  mm. For  $n$  slices, the excitation and emission intensities are given in equation (5.6).

$$I_{ex}^{s_n} = 10^{-\varepsilon C n L} \quad (5.6)$$

$$I_{em}^{s_n} = Q I_{ex}^{s_n} \frac{R-h}{2R},$$

$$\left( nL \leq h \leq \sqrt{nL^2 + \left(r + \frac{nL}{\sqrt{3}}\right)^2} \right), R = \sqrt{r^2 + h^2}$$

The profiles for the emission intensities for  $n$  slices are as shown in Figure 5.14. The total emission intensity at the fiber is the sum of all the intensities resulting from each slice.

Figure 5.15 illustrates the contribution of 10 slices to the emission intensity at fiber end. Note that this profile is for emissions along the entire diameter for the fiber (earlier profiles are for the positive  $Y$  axis only).

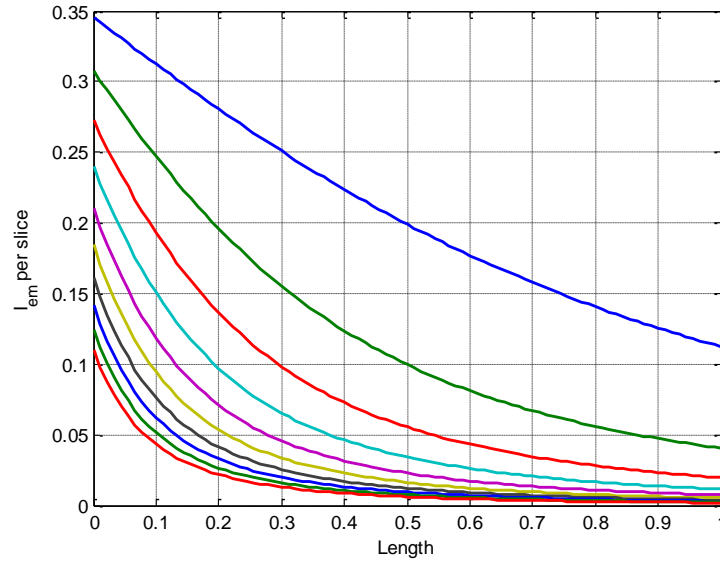


Figure 5.14: Emissions along radius along positive  $Y$  axis for  $n$  slices;  $n = 10$ ,  $L = 0.1$  mm,  $r = 1$  mm,  $C = 0.5 \mu\text{g}/\mu\text{l}$

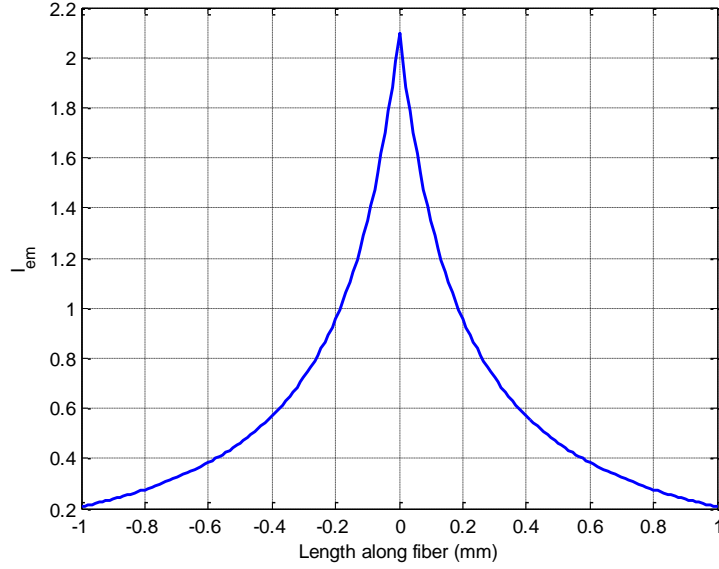


Figure 5.15: Total emission along the diameter for  $n$  slices,  $n = 10$ ,  $r = 1$  mm,  $l = 1$  mm,  $C = 0.5\mu\text{g}/\mu\text{l}$

In each case, the peak emission at the fiber axis is at maximum. If this maximum intensity is plotted against  $l$ , the plot shown in Figure 5.16 is observed. The plot suggests that the maximum emission intensity value stabilizes as  $l$  increases. In this case, more than 90% of the emission is captured when the FLE is placed at a distance of more than 4mm from the fiber.

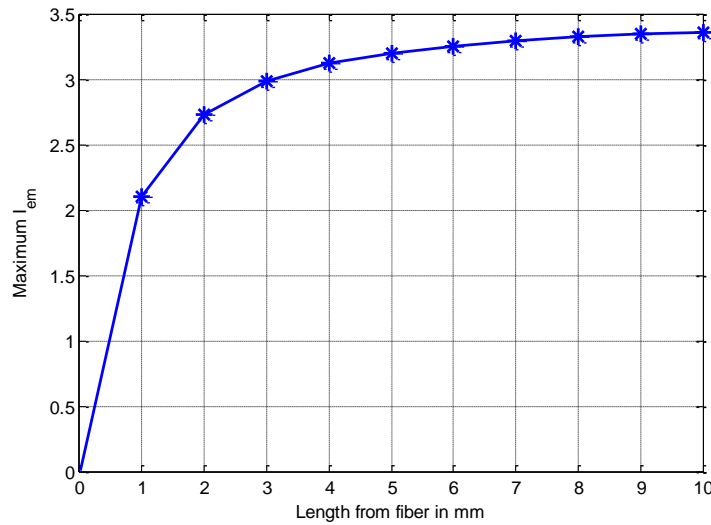


Figure 5.16: Maximum emission intensity for varying lengths

- ***Practical implementation of GFP-FLE***

The theoretical curve as shown in Figure 5.16 was verified practically by using the GFP optical sensor with blue LED intensity at 40 mA. The FLE was positioned 5 mm from the tip of the optrode. It was observed that both the theoretical and practical curves overlap, thus, validating the GFP-FLE derivation.

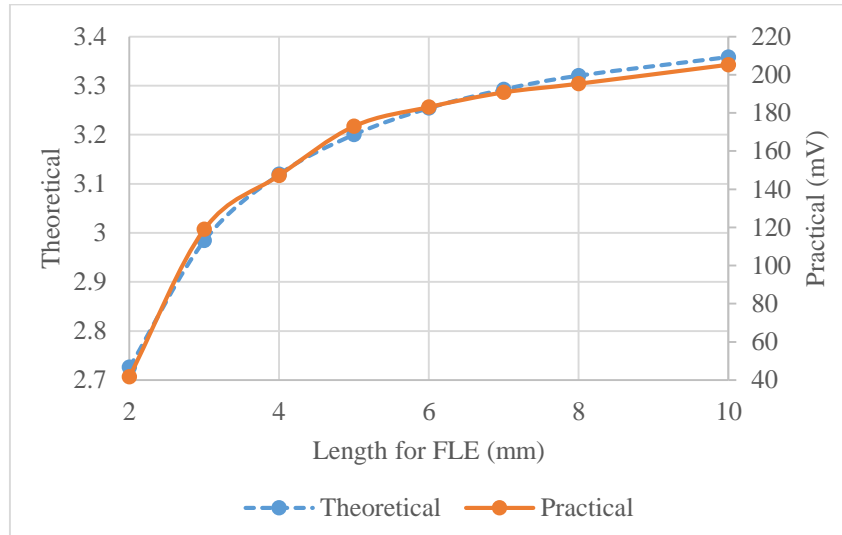


Figure 5.17: Comparison of theoretical and practical values for GFP-FLE

Then, a comparison was drawn between the presence and absence of FLE on the GFP sensor. The optrode was dipped in an HPTS solution (0.1 ml HPTS + 10 ml DI water) in a flask. Data was read at different depths and compared as shown in Figure 5.18. Without the FLE, the standard deviation observed is 11.092 mV whereas with the FLE, the standard deviation is 0.75 mV. Thus, the FLE stabilizes the reading from the solution eliminating the depth parameter as a variable.



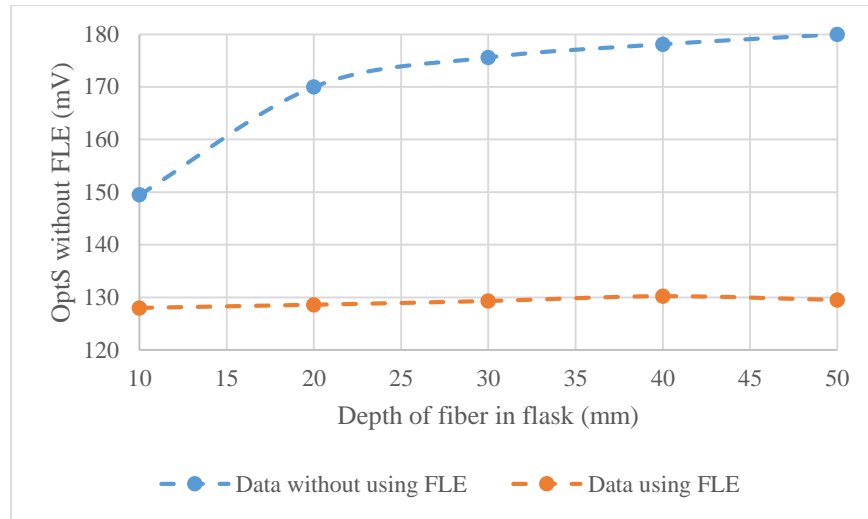


Figure 5.18: Comparison of data recorded when using and not using FLE

### 5.3 Filtered Rate Analysis (FRA)

The differentiation of GFP expression data with respect to time results in rate of expression. Rate is a highly useful tool in determining the control process of protein expression. Figure 5.19 illustrates the ideal GFP expression and rate profiles.

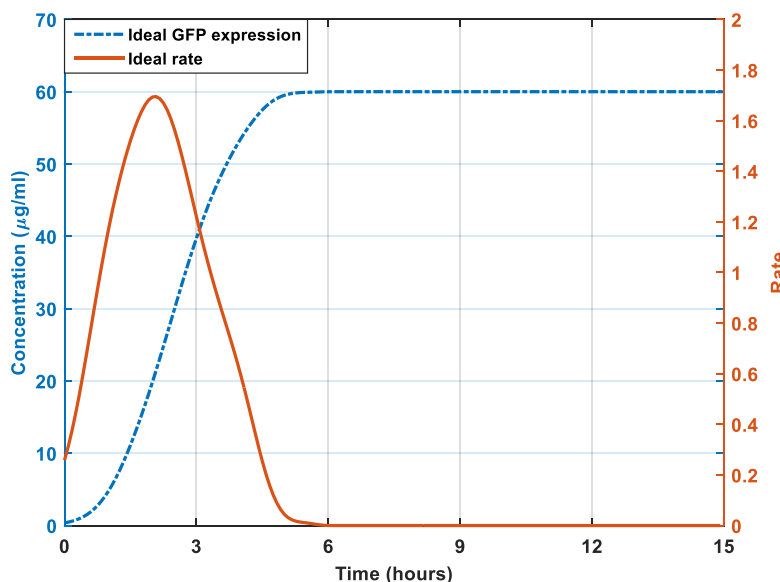


Figure 5.19: Ideal GFP expression data and corresponding rate data

The plot shows that the peak (maximum) of the reaction is the maximum rate achieved by the reaction, and the end of the reaction occurs when the rate curve returns to zero. To enhance the protein expression process, one could either work towards increasing the peak of the reaction, or increasing the time period of the reaction, based on the requirement. Thus, rate analysis assists in optimization and process control for protein production. Rate analysis can be used to diagnose the mechanism of gene expression and the cause of changes in the reaction. Furthermore, monitoring the rate can help with removing bottlenecks for gene expression.

Direct differentiation of expression data to derive rate data is possible only in case of an ideal signal. In case of real signals, expression data is noisy leading to rate data being noisy. Digital filters are used to eliminate noise from expression and rate signals. Filters like IIR Butterworth

filter, FIR Hamming window filter and moving average filter were evaluated to obtain optimum results, without signal attenuation and delay.

Rate analysis can be performed both online and offline. Online processing would ensure real-time rate monitoring. Offline analysis or post-processing of expression data is useful for further investigation of rate data. This study involved the comparative analysis of multiple filters to evaluate the most ideal fit for online and offline monitoring and analysis of rate.

The ideal rate data was calculated by serially differentiating 10 ideal expression data points at a time. This data was generated for comparison of real-time and post processed results of real data and to determine the best choice of filter. The methods used for real-time processing and post-processing of the real data are used for ideal data as well, after which results of both evaluations were compared.

- **Online (real-time processing) FRA**

Real-time rate analysis involved filtering the data collected from the GFP optical sensor and differentiating ten expression data points to get one rate point. Figure 5.20 illustrates the algorithm developed for real-time rate analysis.

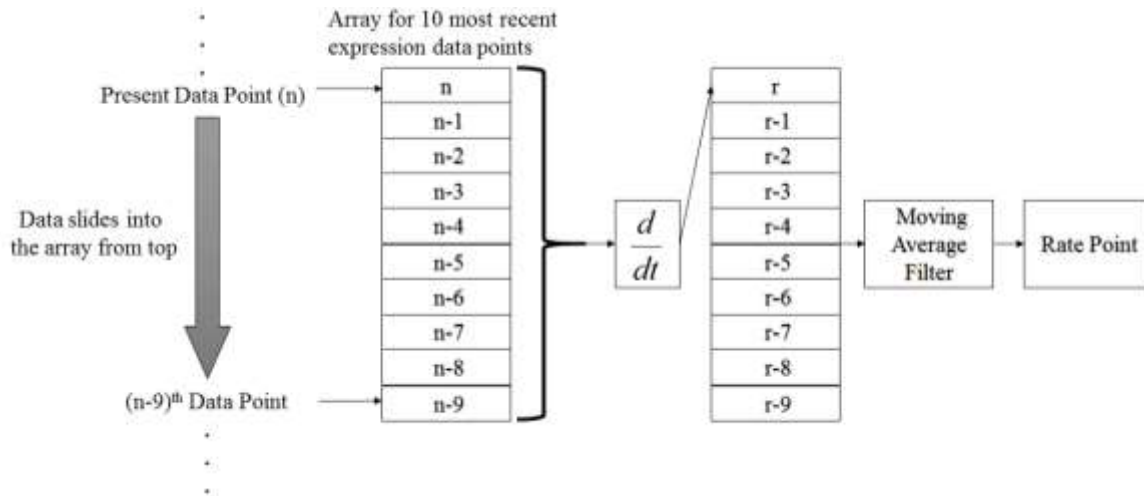


Figure 5.20: Block diagram of real-time rate analysis in GFP optical sensor

An array of size 10 was setup in the form of a queue data structure. This implied that for the data collected, the most present data point 'n' is at the first position in the array; and as newer data points are recorded, this 'n<sup>th</sup>' data point is pushed further down in the array. After the 10th position in the array, the data point was discarded. It should be noted that the array size is selected by user.

In every iteration, a new data point was collected in the queue. Once 10 data points were collected in the array, the entire array was numerically differentiated to calculate one rate point corresponding to the 10 elements in the array in that iteration. This rate point was then pushed onto another queue filled with the 10 most recent rate points as shown in Figure 5.20. A moving average filter was implemented, as the simplest choice for an FIR filter, especially in a real-time process. Ten rate points are filtered (averaged) to obtain one filtered rate data point.

The ideal signal was processed as per the real-time processing of data for rate analysis. The differentiated signal (rate signal) was passed through a moving average filter with a window size 10. A visual interface was designed in LabVIEW to process the ideal data. The following figure illustrates the ideal data rate analysis using the real-time processing.

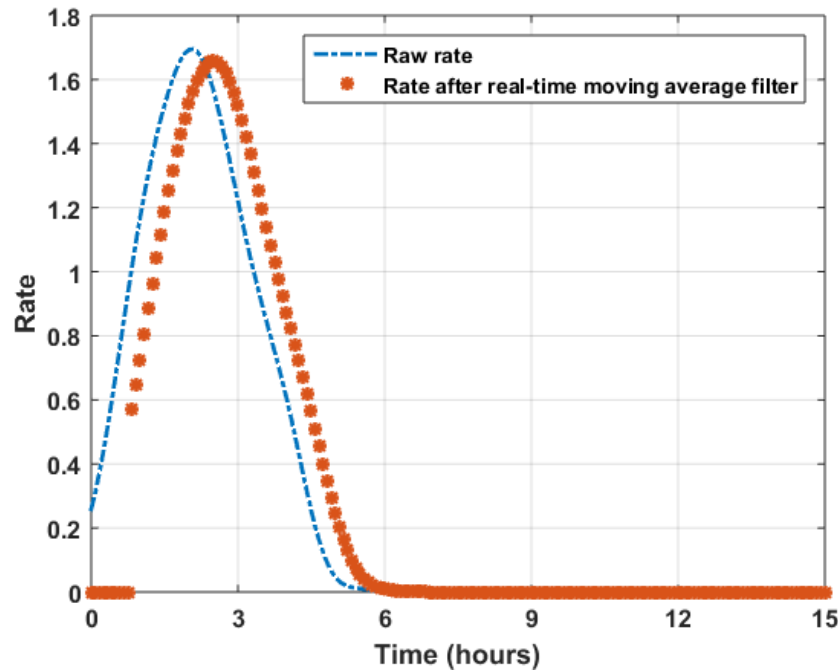


Figure 5.21: Ideal rate and rate after real-time rate analysis of ideal GFP expression data

As observed from Figure 5.21, the ideal rate data was compressed and delayed after passing through the moving average filter. The compression of amplitude of the signal was 2.2%, and the delay was approximately 25 minutes. The signal compression can be ignored; and since the GFP protein folding time is approximately 20 minutes, the delay can be overlooked as well. This is a result of the use of a digital filter to clean out the noise from a signal.

The real-time data collected from the GFP optical sensor is shown in Figure 5.22. The GFP expression data is represented by the dotted line whereas the filtered rate data is the solid line. From the rate data, it is observed that the expression reaches its peak after 2.5 hours. The rate peak goes back to zero amplitude after approximately 6 hours. At this point, the expression profile also stabilizes. Thus, it was verified that the expression reaches a plateau when the rate profile goes back to zero amplitude.

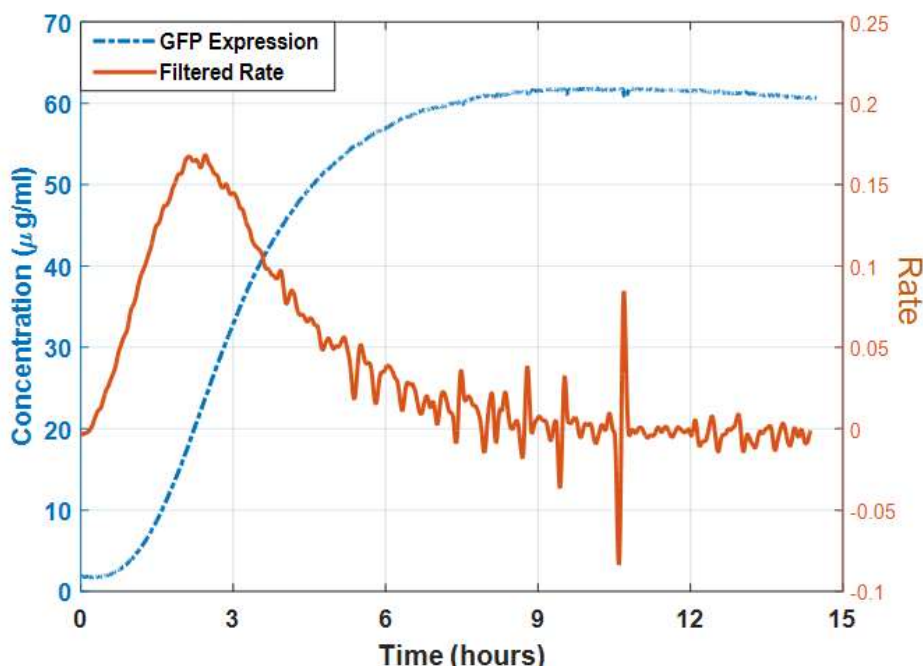


Figure 5.22: Real-time GFP expression and rate data from GFP optical sensor

It was observed that when the expression data stabilizes, there is a lot of noise introduced in the rate signal (even though a moving average filter is used) due to the smallest anomaly in the

expression data. Thus, the real-time rate analysis gives a brief idea about the reaction process, but for further clarification, post-processing of the data is essential.

- **Offline (post-processing) FRA**

After studying a variety of filters that can be used, the IIR Butterworth filter and FIR Hamming window were selected for post-processing of expression data for rate analysis. The filters were implemented in MATLAB. To ease the process, the sampling time was normalized to 1 sample/second. Hence, the frequency of sampling was 1 Hz while the normalized frequency was  $2\pi$ .

The expression data was filtered, as opposed to the rate data for post-processing. This is because the error introduced in the form of delay and signal amplitude compression was lesser when expression data, and not rate data, was filtered.

For both filters, the cutoff frequency was found by plotting the frequency response, and both filters are implemented on the expression data. Further, the rate data is calculated by differentiating the filtered expression data.

The frequency response for the ideal GFP expression signal is as shown in Figure 5.23. The cut-off frequency for the same is decided at  $0.06 \pi$  rad/sample.

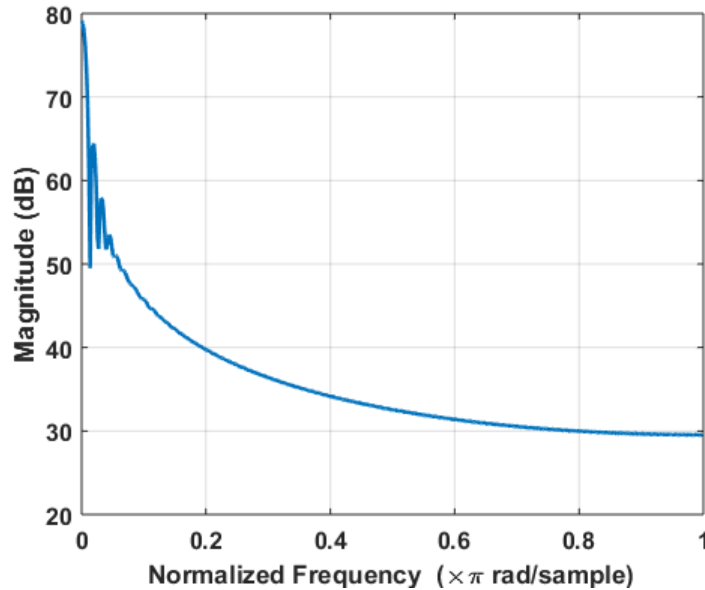


Figure 5.23: Frequency Response of ideal GFP expression data

Considering this cut-off, the ideal expression data was filtered using a Butterworth filter. There was no signal compression, but the delay introduced was approximately an hour, as shown in Figure 5.24. This delay cannot be ignored and hence, the delay was compensated by shifting the filtered signal back by an hour.

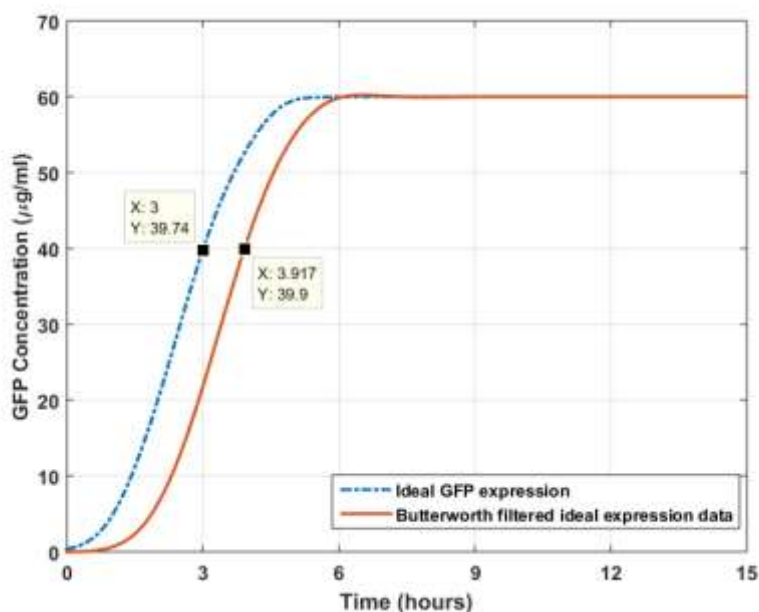


Figure 5.24: Time delay introduced in ideal signal due to use of Butterworth filter

Figure 5.25 illustrates the Butterworth filtered GFP expression profile after delay compensation, and the resulting rate profile. It was observed that the Butterworth filter introduced a small wave-like profile at the end of the expression and rate curve. This was an anomaly introduced because of the Butterworth filter coefficients. These anomalies are introduced as a result of the unstable nature of the Butterworth filter.

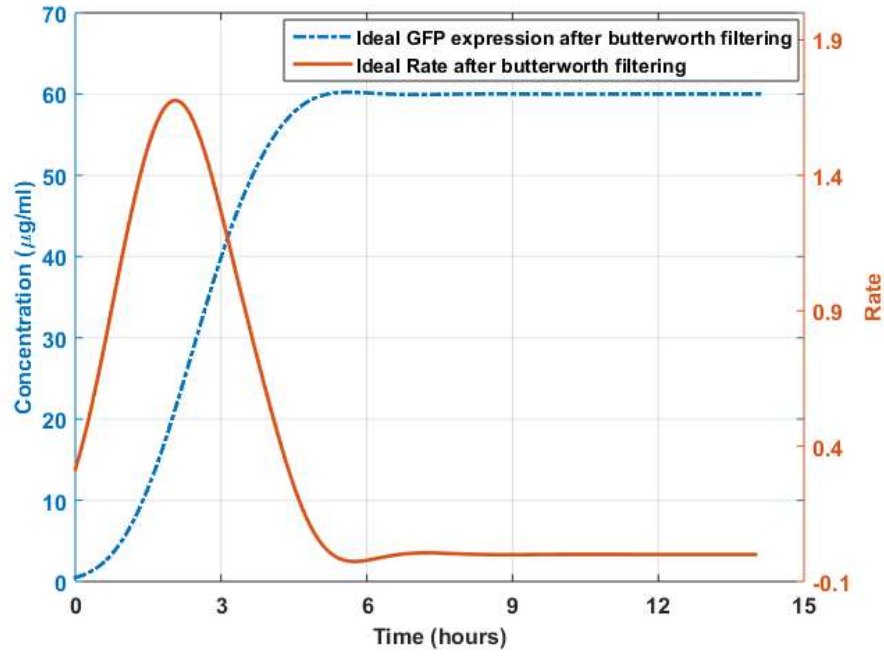


Figure 5.25: Ideal GFP expression and rate profiles after using Butterworth filter

To rectify these anomalies, an FIR filter using a Hamming window was used. The filter used a cutoff frequency of  $0.06 \pi$  rad/sample (same as the Butterworth filter) and the window size was 100. Figure 5.26 shows plots for filtered expression data and rate data after filtering.

It was observed that there is no compression but the delay introduced was approximately 4 hours. This delay cannot be ignored and hence, the delay was compensated for by shifting the filtered signal an hour back. The profile for the signal was preserved better compared to the Butterworth filter.



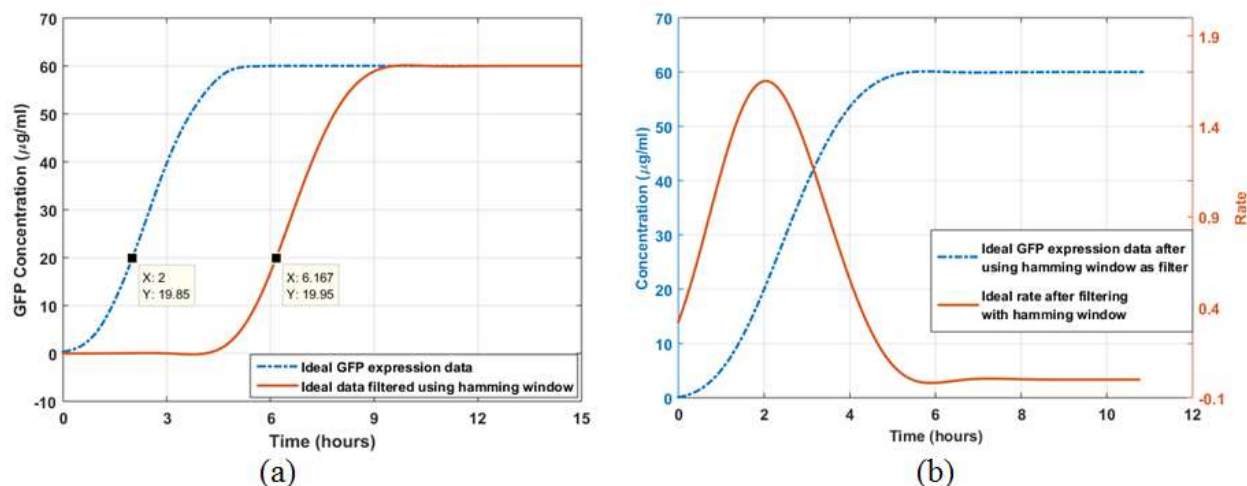


Figure 5.26: (a) Time delay introduced in ideal signal due to Hamming window, (b) Ideal GFP expression and rate data after filtering with Hamming window

In Figure 5.26 (b), it was observed that the Hamming window also introduced a small wave-like profile at the end of the expression and rate curve. This anomaly however, is not as evident as in the Butterworth filtered profile.

GFP expression data was collected real-time by the optical sensor and processed in real time as shown in Figure 5.22 above. Even though the rate data was filtered, it was still observed to be moderately noisy. This is because of the use of the moving average filter. Post-processing is performed to clean up the noise in this data. The cutoff frequency for the signal is decided at  $0.03 \pi$  rad/sample.

This data is processed using an IIR Butterworth filter and a FIR Hamming window filter with a  $0.03 \pi$  rad/sample cut-off.

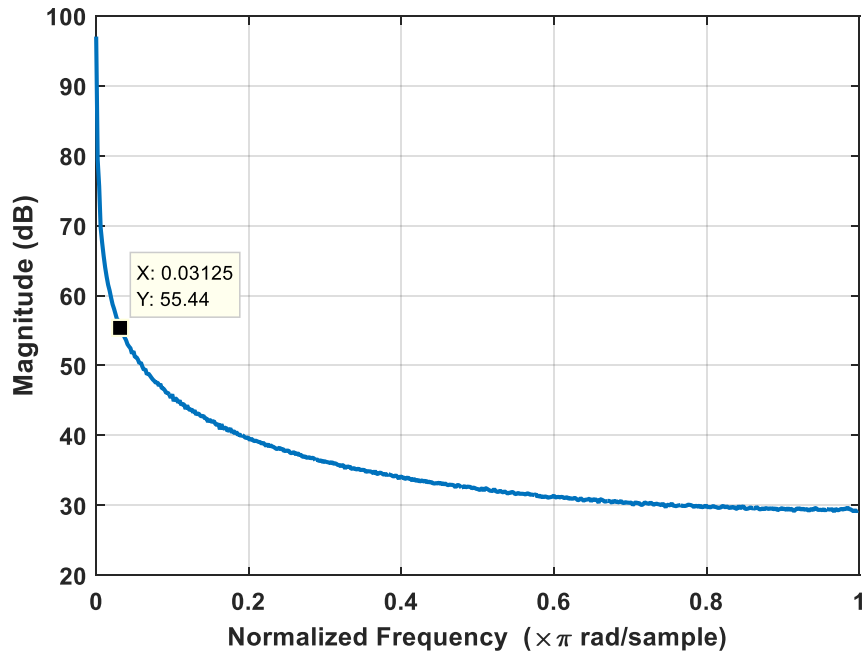


Figure 5.27: Frequency response of GFP expression data from optical sensor

**Butterworth filter:** As the Butterworth filter is an IIR (Infinite Impulse Response) filter, it is not always stable. Thus, the order of the filter needs to be high enough to filter out the high frequency components, but the signal profile should not be compressed or delayed by a great extent. The order is selected to be 3 for the frequency cutoff of  $0.03 \pi$  rad/sample. The delay introduced due to filter complexity (due to high order of filter) was approximately 0.2 hours or 12 minutes. This delay is compensated by shifting the entire expression profile back in time by 12 minutes. The filtered expression data and corresponding rate data are as shown in Figure 5.28 and Figure 5.29.

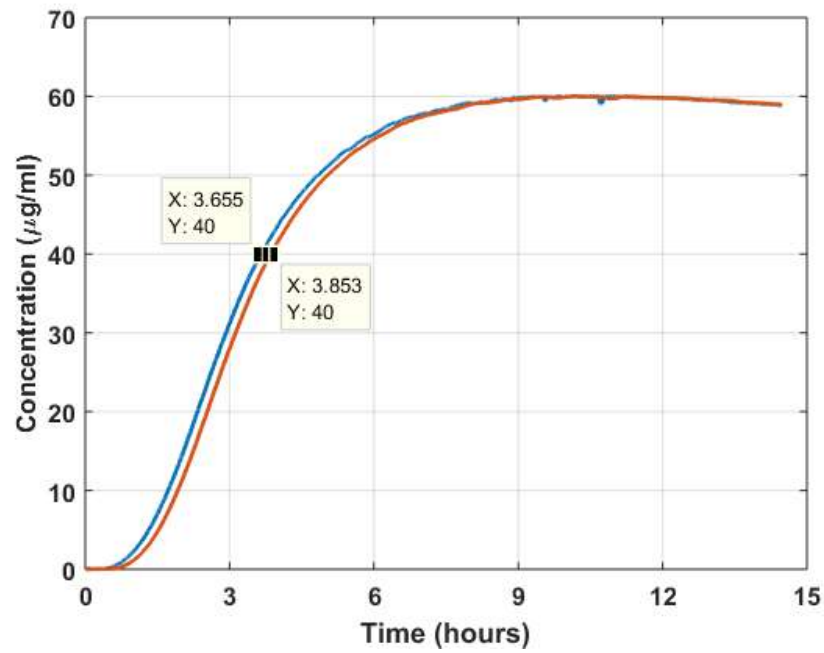


Figure 5.28: Delay introduced due to use of IIR Butterworth filter

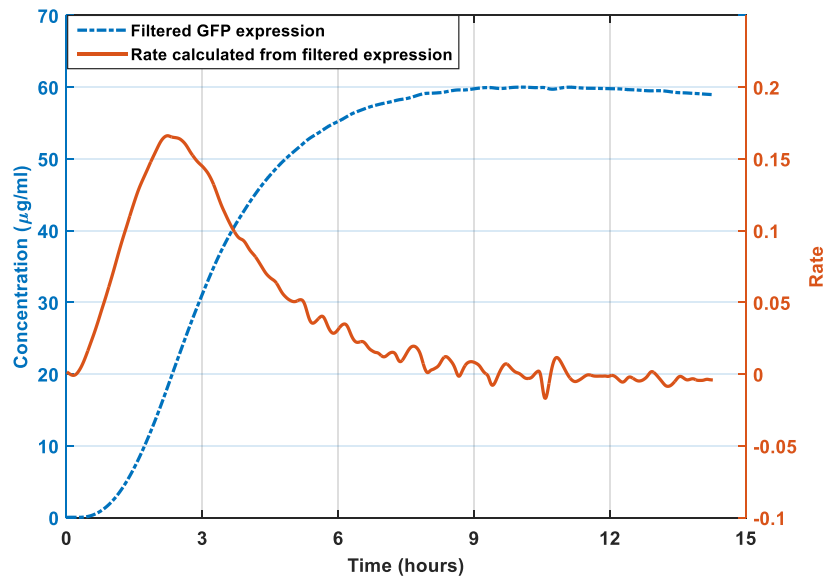


Figure 5.29: Filtered and delay corrected expression plot using Butterworth filter and corresponding rate plot

The disadvantage of using a Butterworth filter or any IIR filter is that the signal amplitude gets compressed when higher orders of the filter are used. Hence, FIR filters prove to be a better option since their use does not cause signal compression even with a high signal delay.

**Hamming window filter:** FIR filters are more stable than IIR filters, but with a higher complexity which introduces more delay. The Hamming window is the least complex window, and is a good fit for this application. It uses same cut-off frequency as Butterworth filter is used ( $0.03 \pi$  rad/sample).

The filter had the window width of 150. The delay observed when using this filter is approximately 42.5 minutes, which is compensated for by shifting the waveform. Figure 5.30 illustrates that the rate data is comparatively less noisy than the Butterworth filtered rate data.

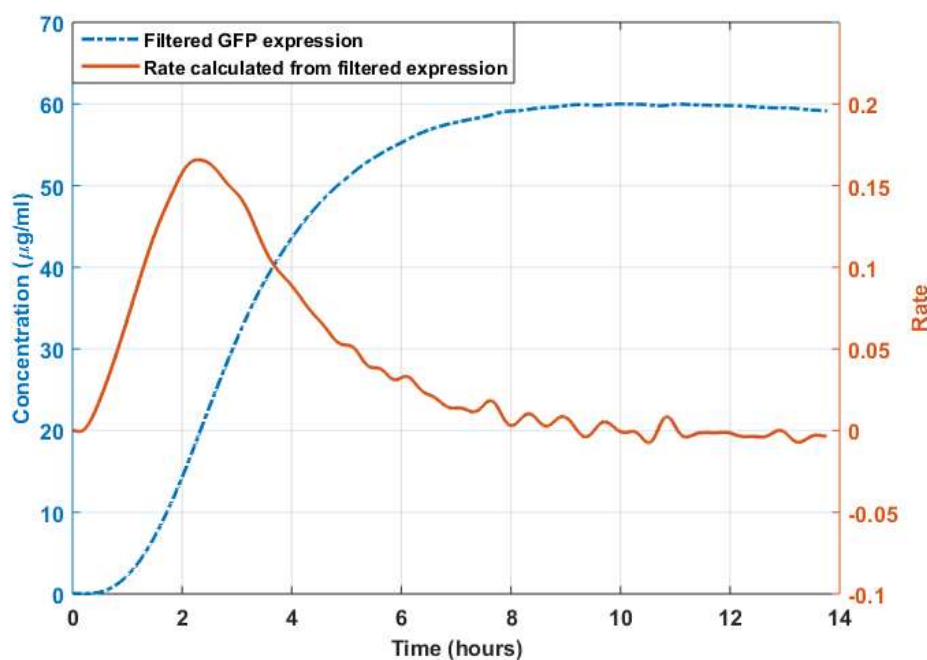


Figure 5.30: Filtered and delay corrected expression plot using Hamming window and corresponding rate plot

#### 5.4 Use of GFP Sensor in Purification Process

GFP expressed in a bioreactor has a significant amount of impurities. These are eliminated by purifying the protein using column chromatography. An automated purification system was developed for purification of GFP as shown in Figure 5.31.

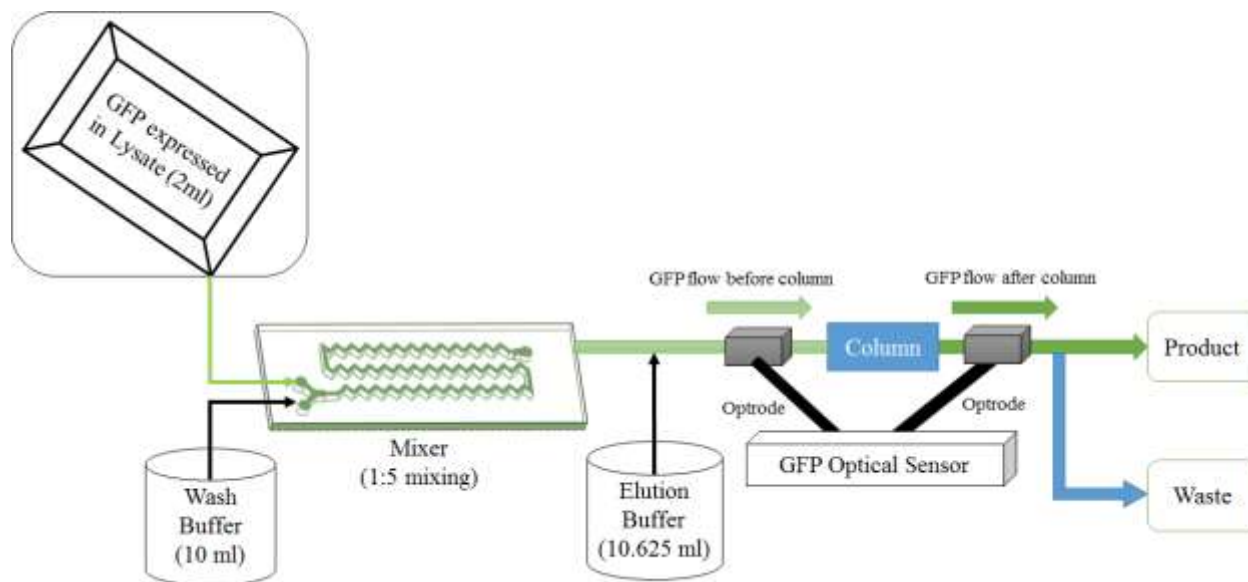


Figure 5.31: Block diagram illustrating purification automation

The chromatography column used for purification was a 1 ml IMAC HisPur™ Cobalt Chromatography Cartridge (90093, ThermoFisher). As seen in Figure 5.31, the GFP expressed in the bioreactor cassette was withdrawn and mixed with the wash buffer. The mixer was designed to ensure homogeneous mixing of the lysate and wash buffer. Then, the mixture is loaded in the IMAC column. The column walls are constructed of tetradentate chelating agarose resin charged with divalent cobalt ( $\text{Co}^{2+}$ ) for obtaining high-purity his-tagged proteins with no metal contamination [36]. When the mixture is loaded, the GFP binds to the column walls and any other impurities in the lysate are washed away using the wash buffer. After the washing process, the elution buffer is passed through the column. The elution buffer picks up the purified GFP from the column. The purified GFP is deposited in the product vial.

The GFP sensor was positioned in the system such that each optrode was reading data at either ends of the column. Theoretically, it is expected that the GFP profile before and after the column should be similar as shown in Figure 5.32

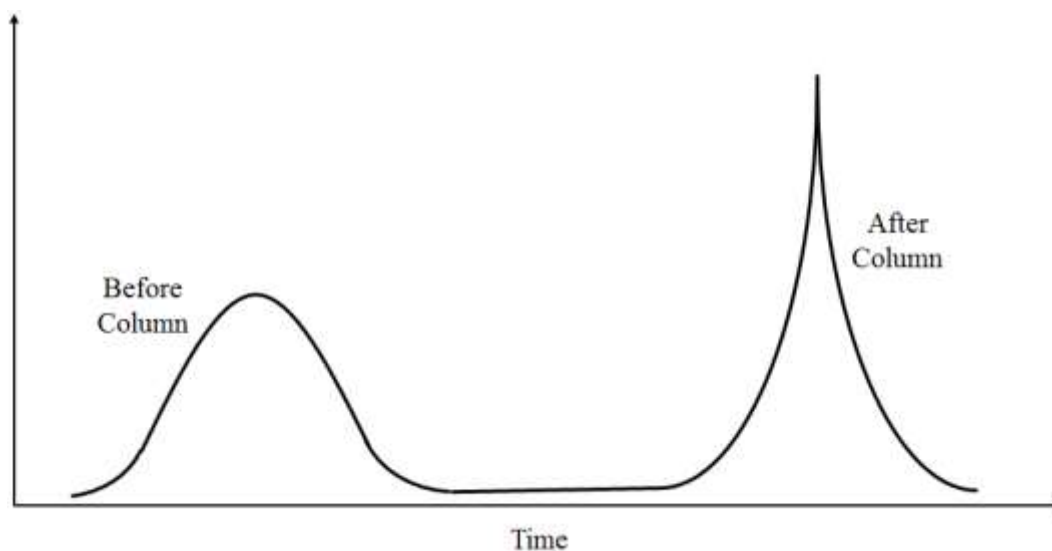


Figure 5.32: Ideal profiles of GFP before loading on column and after elution

Before the column, the GFP contains impurities, thereby diminishing its fluorescent intensity. The GFP sensor should ideally detect a profile that resembles a Gaussian distribution. After the column, the GFP is in its purest form in the elution buffer resulting in a much higher fluorescent intensity. The GFP sensor should detect a profile resembling the Laplacian distribution. Theoretically, the areas under both curves should be identical, implying that the same amount of GFP enters and leaves the column, varying only in fluorescent intensity.

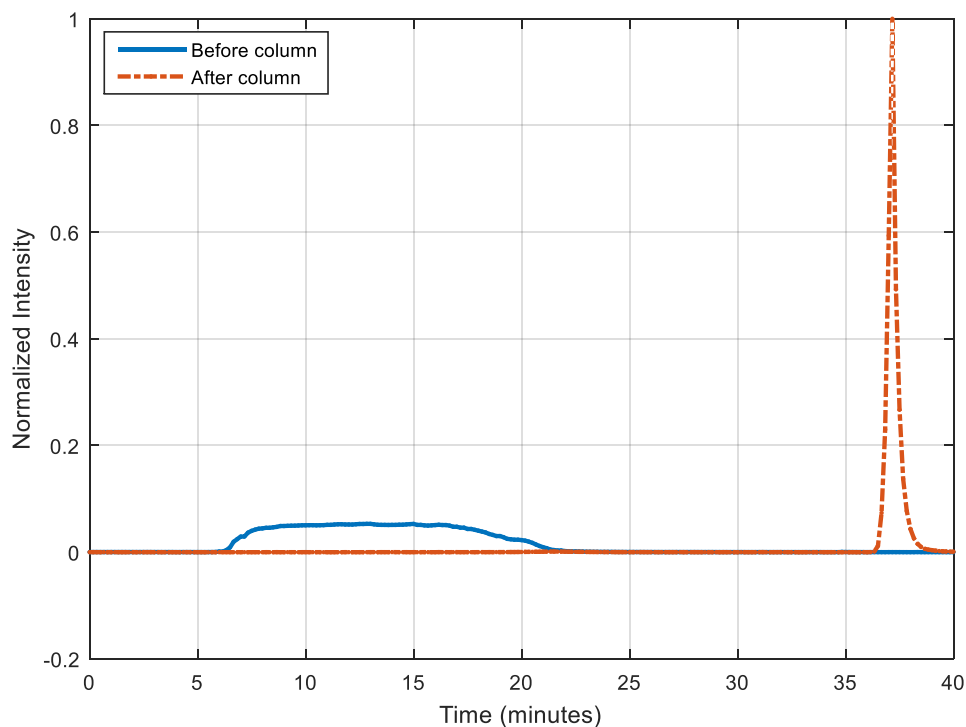


Figure 5.33: Purification data collected from GFP optical sensor

This data was collected from the purification automation system on August 28, 2015. As seen from Figure 5.33, the profiles for GFP fluorescent intensity detected before and after the columns resemble Gaussian and Laplacian distributions respectively. The areas under the Gaussian curve is 3.79, and that under the Laplacian curve is 2.99. Hence it can be concluded that the areas are almost equal. The inequality results due to the use of 2 optrodes and the non-ideal nature of both their optical equipment.

Figure 5.34 depicts another profile from a GFP purification experiment conducted in the DARPA purification system.

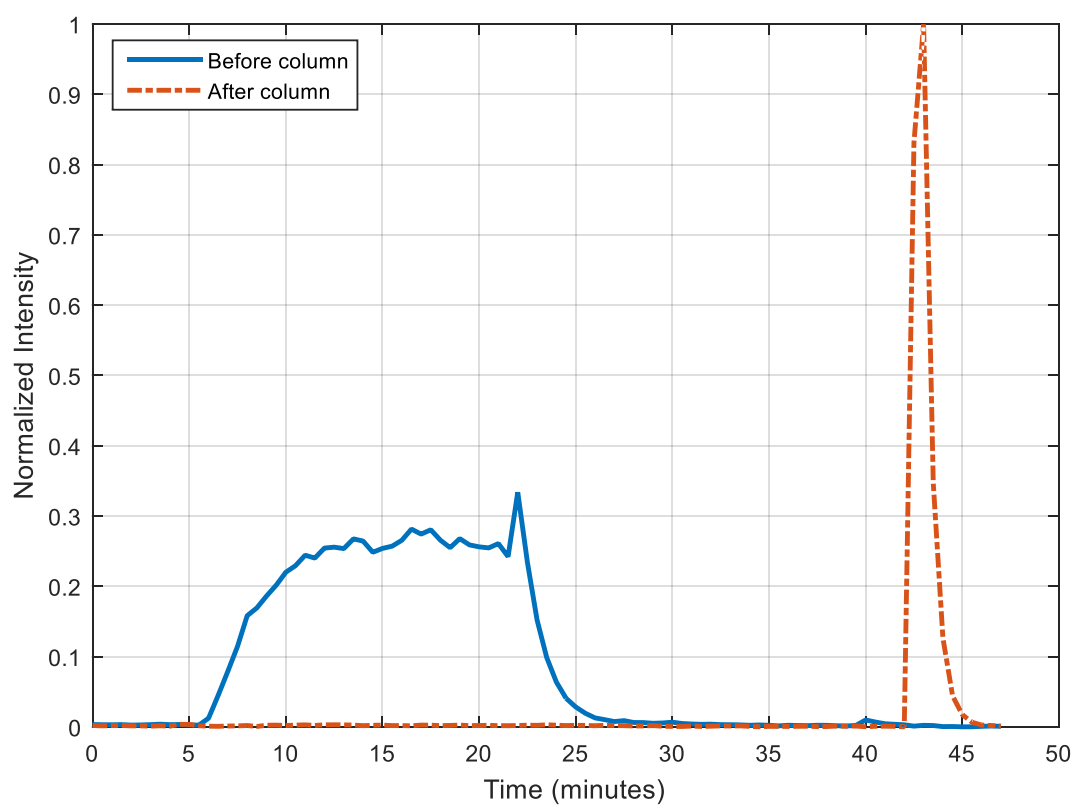


Figure 5.34: Purification data collected from GFP optical sensor, area before column = 3.93, area after column = 2.5

The GFP optical sensor was used by the Ohio State University (OSU) team for real-time tracking of purification. From the data that they collected, the sensor delivered the data as expected.



## ***5.5 Summary***

BASS was verified to be used in real-time monitoring of GFP. The system was calibrated, and validated in a GFP expression experiment. A fixed length extension for the optrode was modelled in MATLAB, and implemented. It addressed the anomalies arising due to movement of optrode along the length of vessel. Rate analysis was investigated as a tool to interpret and optimize GFP reactions. Signal processing techniques for filtering high frequency noise in expression and rate signal were studied. A moving average filter was used for online filtering of rate signal, and a Butterworth filter and Hamming window filter were used for offline processing of expression data. BASS was also used to monitor GFP before and after the protein purification process.

## Chapter 6. UV ABSORBANCE SENSOR SYSTEM

Protein concentration quantification is essential for all protein expression and purification techniques. Online measurement of protein concentration is important, especially in flow-injection analysis or as a detector on the output of a chromatographic column [37], [38], [39], [40], [41]. Often, concentration is determined from optical absorption measurements of the protein in the UV range [42], [33]. The ratio of absorbance at 260 nm versus 280 nm is commonly used to assess DNA contamination of protein solutions, since proteins (in particular, the aromatic amino acids) absorb light at 280 nm, and DNA and RNA absorb maximally at 260 nm [43], [44]. Table 6.1 presents 260 nm: 280nm ratio corresponding to percentile nucleic acid contamination in protein.

Percentage Protein	Percentage Nucleic Acid	260 nm:280 nm ratio
100	0	0.57
95	5	1.06
90	10	1.32
70	30	1.73

Table 6.1: Percentage nucleic acid contamination in protein [44]

The optical sensor is modified to enable the measurement of the same. The blue and violet LEDs on the sensor are replaced with 260 nm and 280 nm LEDs, and the Si-photodiode is replaced with a UV sensitive photodiode. This sensor will be referred to as the UV absorbance sensor. Experiments are conducted to validate the sensor.

Another method is devised to calculate UV absorbance using the same Si-photodiode used for pH, DO, and GFP measurements. Quantum dots are used to convert unabsorbed UV light to visible range red light, so that the Si-photodiode can detect the same. This sensor would be termed as the QD sensor. A dual channel sensor is developed such that one sensor is a standard UV absorbance sensor and the other is a QD sensor. Simultaneous measurements with both the sensors are

conducted to enable use of the same signal conditioning circuit for the signals generated. A comparative analysis reveals that the QD sensor contributes lesser noise to the measurements.

### ***6.1 UV Absorbance Sensor***

The optical design and construction of the UV sensor (named AB1) is described in Section □. A flow through cuvette was made in the lab with quartz plates of 1mm thickness. The actual electronics for the system are not changed. pH mode was used for measurement of UV absorption.

AB1 is calibrated by using a protein called Albumin from bovine serum (A3311, Sigma Life Science) or BSA. The BSA was serially diluted from a highest concentration of 5 mg/ml and a lowest concentration of 0.04 mg/ml. BSA was 1:1, 1:2, 1:4, etc. times serially diluted. These samples were measured in the sensor in a home-made quartz cuvette. A PMMA sheet was cut in the desired cuvette shape and quartz walls were attached on it. AB1 was operated at 25 mA with 3 second intervals between sample measurements.

DI (deionized) water was used as the blank. Then, the sensor was used to measure the serially diluted protein samples, and their corresponding absorbance was recorded. Calibration curves corresponding to UV absorbance at 260 nm and 280 nm were generated from this data.

The concentrations of the serially diluted BSA samples were also measured on a lab-grade spectrophotometer (HP 8453 UV-Vis spectrophotometer). These readings were considered as standards. The same quartz cuvette that was used with the absorbance sensor was used to take measurements. Correlation curves were generated for absorbance sensor and spectrophotometer measurements as shown in the Figure 6.1 and Figure 6.2.

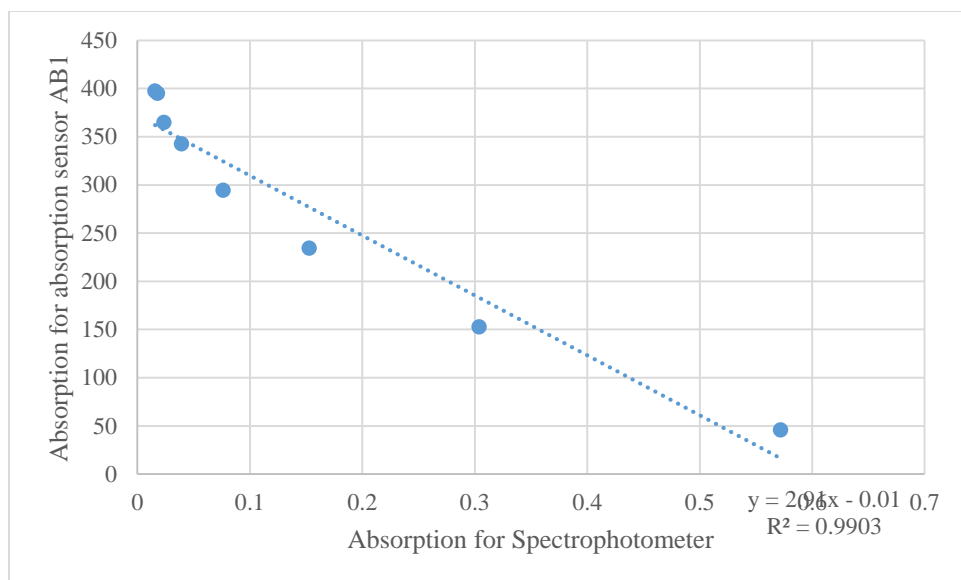


Figure 6.1: Correlation for UV absorbance at 260nm for AB1 and spectrophotometer

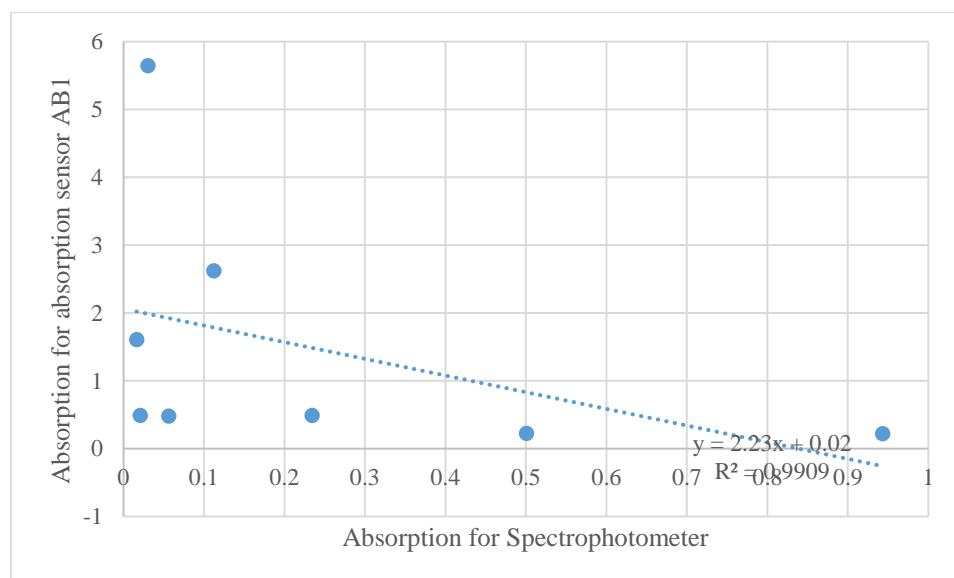


Figure 6.2: Correlation for UV absorbance at 280nm for AB1 and spectrophotometer

Correlations for UV absorbance at 260 nm and 280 nm for AB1 and the spectrophotometer are 0.9903 and 0.9909 respectively. Average raw voltage errors were  $\pm 0.75$  and  $\pm 1.33$  for 260 nm and 280 nm respectively. Thus, the absorbance sensor is validated.

The ratio of 260 nm to 280 nm for the serially diluted samples of BSA are as shown in Table 6.2.

<b>Concentration (mg/ml)</b>	<b>Ratio for spectrophotometer</b>	<b>Ratio for UV sensor AB1</b>
5	0.61	0.78
2.5	0.61	0.77
1.25	0.65	0.75
0.625	0.68	0.82
0.31	0.70	0.71
0.16	0.77	0.76
0.08	0.86	0.40
0.04	0.96	0.78

Table 6.2: 260 nm:280 nm ratio for serially diluted BSA samples using spectrophotometer and AB1 UV sensor

From Table 6.1 and Table 6.2, it is evident that the BSA protein samples are more than 95% pure. The ratios for the spectrophotometer and the absorbance sensor vary by approximately 0.1. Thus, the UV absorbance sensor is useful in determining protein purity. In future, multiple UV systems will be standardized using the same standardization procedure used for pH measurements.

The UV absorption sensor was fairly expensive due to the high-cost of the UV LED and UV photodiode. A low-cost sensor could be implemented if a quantum dot plate is used as a wavelength convertor. A comparative study is conducted for the same as follows.

## ***6.2 Comparative Analysis of QD Sensor and UV Sensor***

Same procedure for calibration and correlation was used for the dual-channel QD-UV sensor (AB0). BSA was serially diluted. DI (deionized) water was used as the blank. Then, the sensor was used to measure the serially diluted protein samples, and their corresponding absorbance was recorded. Calibration curves corresponding to the QD and UV sensors were generated from this data.

The concentrations of the serially diluted BSA samples were also measured on a lab-grade spectrophotometer and were considered as standards. The same quartz cuvette that was used with the UV absorbance sensor was used to take measurements. A calibration curve from the spectrophotometer measurements was also generated, and a correlation for calibration curves for both systems was calculated.

The calibration results for the spectrophotometer and absorbance sensors are presented in Figure 6.3. For the spectrophotometer, readings were taken at 280 nm only. For the absorbance sensor, measurements were taken every 10 seconds for 5 minutes continuously for each protein sample, and these readings were averaged.

The calibration data is presented after calculating the absorbance. It is observed that the spectrophotometer curve (which is used as a standard), exhibits highest sensitivity. The UV sensor exhibits slightly smaller sensitivity, and the QD system shows even lower sensitivity. Linearity in each case is better than 0.99. It is worth noting that the average absorbance noise for the spectrophotometer was  $\pm 0.2 \times 10^{-3}$  whereas for the QD sensor and UV sensor, it was  $\pm 0.55 \times 10^{-3}$  and  $\pm 1.12 \times 10^{-3}$  respectively. Thus, the noise introduced due to the UV sensor is twice that of the noise introduced by the QD sensor while the sensitivity is only 40% better. The correlation between the absorbance data from the spectrophotometer with the QD sensor and UV sensor was better than 0.99 in both cases.

The calibration curves for both sensors can be adjusted to the standard curve of the spectrophotometer by use of coefficients. After this adjustment, the noise of the measurement of the QD sensor is still lower than the noise of the UV sensor. Therefore, it is expected that the use of the QD system in the low-cost portable equipment would yield better precision.

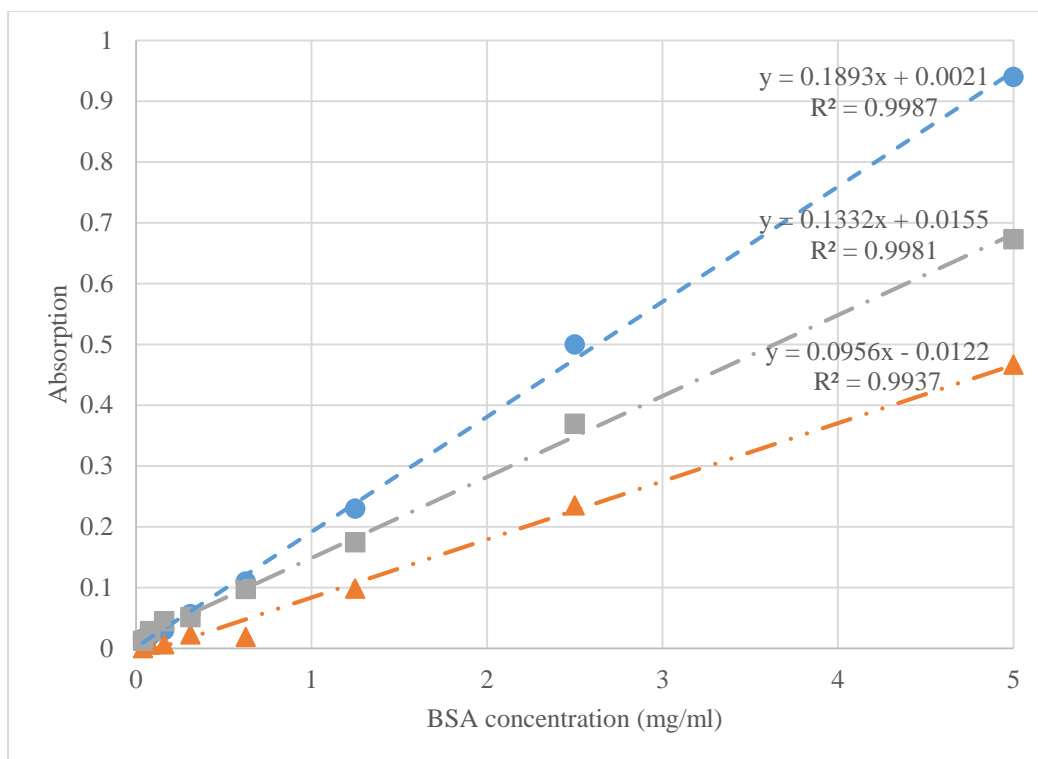


Figure 6.3: Absorbance of BSA as measured on lab-grade spectrophotometer, and UV photodiode, QD-Si-photodiode equipped sensors (standard deviation data shown in text below).

●-Spectrophotometer, ▲-QD sensor, ■-UV sensor

The raw voltage data for QD and UV sensor are as shown in Figure 6.4. The average standard deviation calculated for the QD sensor was  $\pm 0.12$  whereas for the UV sensor, the noise was  $\pm 0.52$ . The maximum and minimum standard deviations for the QD sensor were  $\pm 0.23$  and  $\pm 0.03$  respectively; whereas the same for the UV sensor were  $\pm 1.17$  and  $\pm 0.26$  respectively. It is observed from both figures that more noise was introduced in the UV sensor at lower concentrations of the protein solution. The correlation between the calibration data from the spectrophotometer and the QDs absorbance sensor was 0.992. For the UV photodiode sensor, correlation was 0.98. However, the QD sensor is less noisy and more precise as compared to the UV sensor.

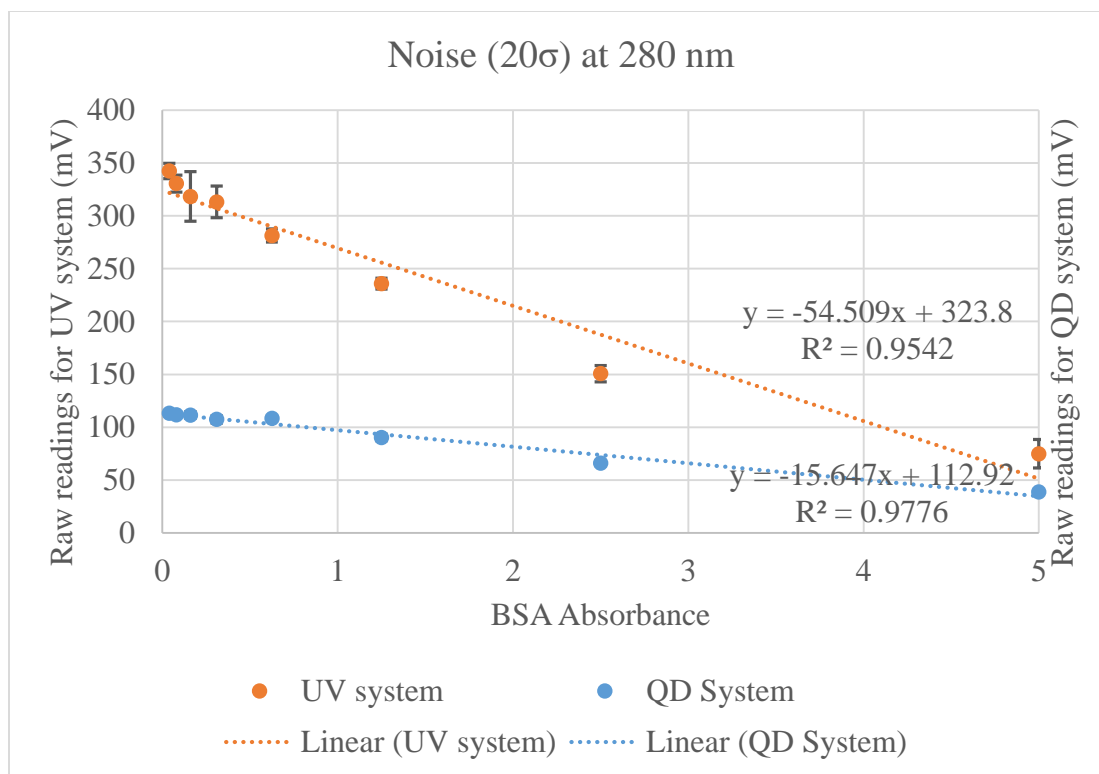


Figure 6.4: Calibration of raw voltage data of BSA as measured on QD sensor

The sensor system was also tested for aging, to check how continuous exposure to UV light affects the components. Both UV and QD sensors were kept running for 44 days. Data was collected every 10 seconds.

It was observed that the UV sensor maintains a constant reading at ~ 610 mV, however, the QD sensor bleaches significantly that causes a drop in the measured signal by around 50 % over a course of 44 days. The bleaching is due to immobilization of the quantum dots in silicone, which causes for high oxygen diffusion. The short term bleaching was ~5% per hour and ~20% per day (worst case). After 20 days of bleaching, it dropped to 0.04% per hour and 2.1% per day. The slow drift should not be a problem, any lab-grade spectrophotometer needs to be frequently recalibrated due to the aging of the UV lamp. Similarly, the QD sensor can either be recalibrated, or it can be pre-bleached to decrease drift during use. Better methods need to be established to encapsulate quantum dots using materials resulting in low oxygen diffusion.



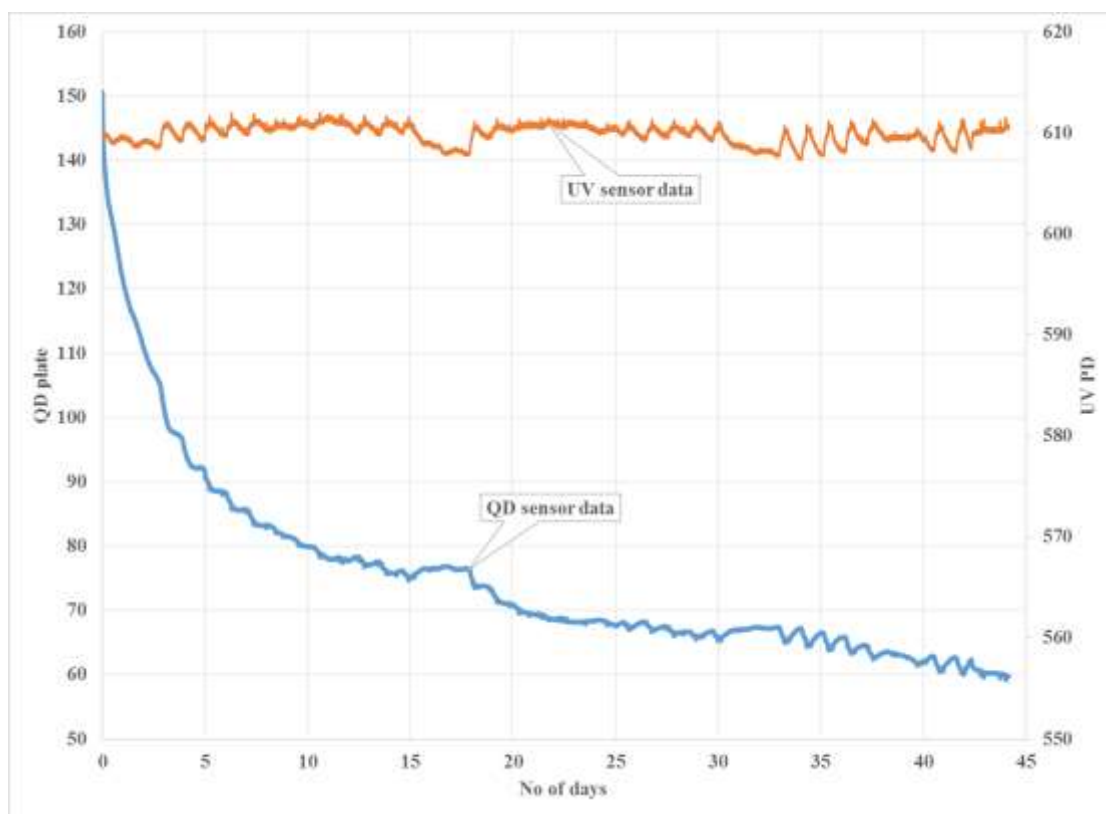


Figure 6.5: Aging data for both, QD and UV sensors

Above results suggest that both the QD and UV sensors are capable of measuring UV absorbance in a regular or flow-through cuvette. Such sensors can find use in on-line determination of protein concentration, e.g. liquid chromatography, flow injection analysis, etc. The QD sensor can find use in situations where low-cost, low-noise measurements are required. The UV sensor would be more useful for long-term monitoring (days).

### ***6.3 Summary***

A UV absorption sensor was developed by modifying the electronics and optics in BASS. UV absorbance is a well-known tool for quantifying proteins. BASS was calibrated with BSA protein samples of varying concentrations and verified against a lab-grade spectrophotometer for 260 nm and 280 nm respectively. To make this system low-cost and less noisy, quantum dots were used as wavelength convertors to convert UV light to visible range red light. A comparative study on the QD and UV sensor proved that the QD sensor contributes to lower signal to noise ratio of the system.

## Chapter 7. CONCLUSION

### 7.1 Summary

This dissertation describes the design, construction, implementation, and validation of an opto-electronic Bioprocess Analysis Sensor System (BASS) with common instrumentation for measurement of bioprocess variables pH and DO (Dissolved Oxygen), real-time tracking of GFP (Green Fluorescent Protein), and measurement of UV absorption. BASS is intended for, but not limited to, real-time monitoring of in-vitro protein production.

Theoretical equations governing system design are derived in **Chapter 2**. These comprise the calibration equations for pH and DO, instrumentation transfer functions, i.e., equations defining a mathematical representation for input-output relation of system instrumentation, and describe the concept of standardization for multiple sensor systems. Instrumentation transfer functions were derived from the theoretical calibration equations. These transfer functions facilitated the common instrumentation hardware design of the sensor system. Standardization was explained as a method to generate equivalent readings for multiple copies of the same sensor. BASS was also used as an UV absorption sensor by modifying the system design, for which two methods were proposed. The first would use a UV LED-UV photodiode pair to detect UV absorbance. The second method would use quantum dots to convert UV light into red light, so that the preexisting Si-photodiode would detect the UV absorbance signal.

Based on this theoretical background, the opto-electronic sensor system was designed. The hardware and optical elements in BASS were discussed in detail in **Chapter 3**. Software was developed for controlling, reading, displaying, and interpreting data from the sensor system components. Modifications made to BASS to implement an UV absorption sensor were also described and illustrated.

After the sensor system was implemented, measurements of the multiple variables were validated. pH and DO were the first variables that were tested for calibration, standardization, and

in actual bioprocesses as described in **Chapter 4**. BASS was used to measure pH and DO using chemical patch sensors. These patch sensors were composed of parameter (pH/DO) sensitive dyes immobilized in a polymer/silicone matrix. Upon excitation with specific wavelengths, fluorescence emission intensities of the dye change based on the amount of parameter (pH/DO) in the process. The system was validated for calibration of pH and DO in solutions with known pH/DO concentration. Once the calibrations were verified, pH and DO were measured in two bioprocesses, one for growth of E. Coli bacteria, and the other for producing the protein EPO. A statistical analysis of measurements for variation in calibration of pH and DO was later performed that determined a mean calibration equation for pH and DO.

BASS measures green fluorescence upon excitation of the bioprocess with blue light. The same principle is used on a standard lab-grade fluorescence spectrometer to measure Green Fluorescent Protein (GFP). Hence, the BASS common instrumentation was used to measure GFP production in real-time as explained in **Chapter 5**. Various calibration methods were tried and tested. A fixed-length extension (FLE) for the optrode was modeled and implemented to reduce anomalies introduced in the signal due to sensor movement. Protein expression rate analysis was performed on the expression data collected. The rate analyses were in real-time as well as post-process. Methods for the same were developed using various low-pass filters (e.g., moving average filter, Butterworth filter, Hamming window filter, etc.) to reduce measurement error. BASS was used to track the GFP purification process as well.

On modifying the instrumentation of BASS, a UV absorption sensor could be constructed as explained in **Chapter 6**. Two approaches were taken to build the absorption sensor, one using UV LED - quantum dots-Si photodiode, and the other using UV LED - UV photodiode pair. A comparative study was done to determine which method works better for UV absorption.

Thus, a sensitive, selective, portable, and robust bioprocess analysis sensor system with common instrumentation for monitoring multiple variables was developed and studied in this dissertation.

## 7.2 Conclusions

BASS was researched, implemented, and validated systematically, following a sequential process to confirm its functions. Each chapter in this dissertation discusses and presents these steps taken for verification.

Instrumentation transfer functions derived from theoretical calibration equations govern the system design. The software component of BASS is capable of automatic detection of the system type – single or dual fiber, the type of patch sensor, whether the patch is present and operational or not (e.g., missing or bleached), etc. Several optoelectronic sensor system boards can be standardized so the electronics generates the same measurement from the same chemical sensor. The system was stable and was not susceptible to bio-fouling.

The opto-electronic transducer, together with the chemical patch sensors, (all together known as BASS) is capable of monitoring pH and DO with resolution of 0.07 pH units and ~2% (average across the entire range) of oxygen saturation, respectively. The sensor calibration does not drift for at least 25 hours.

If the optoelectronics was used without the chemical patch sensors, it is capable of monitoring the changes in the media fluorescence, i.e., the production of green fluorescent protein (GFP). It is possible to track real-time production of GFP using BASS. Calibration and verification of GFP expression monitoring in real-time demonstrated that even though the sensor tracks the GFP expression profile accurately, it estimates GFP concentration with a  $\pm 12.4\%$  error. The practical implementation of the fixed-length extension (FLE) for the optrode (modelled in MATLAB) showed that there is ~0.6% error introduced when it is used, as opposed to a ~33.33% error when not used. For real-time rate analysis, the moving average filter is used as a smoothening filter. For post-processing of data, a more complex IIR Butterworth filter or a FIR Hamming-window filter is used for smoothening purposes. The filters are selected based on the amount of error in the signal. BASS is also used to track protein purification in real-time.

Upon modifying the instrumentation for BASS, a UV absorption sensor was developed. Initially, common instrumentation was modified such that 260 nm and 280 nm UV LEDs replaced the blue and violet LEDs, and a UV sensitive photodiode replaced the Si-photodiode. Upon calibrating with BSA protein samples, it was observed that the sensor has a 0.99 correlation with

a standard lab-grade spectrophotometer. The ratio of UV absorbance logged at 260 nm to 280 nm concluded that the protein samples were more than 95% pure.

To make the UV sensor low-cost, another method was developed to measure UV absorption. Quantum dots were used to convert UV light to red light, thus being detectable by the Si-photodiode. A comparative study of the UV sensor and QD sensor revealed that both have a 0.99 correlation with the standard lab-grade spectrophotometer. The UV sensor is 40% more sensitive than the QD sensor, but contributes to twice the noise as opposed to the QD sensor. Upon testing the sensor for aging over 44 days, it was observed that the UV sensor is more stable than the QD sensor. Thus, the UV sensor is more useful for measuring data over longer periods of time (days).

Thus, the bioprocess analysis sensor system (BASS) was researched, designed, developed, and validated. The ability for standardization of the sensor and the auto-detection capabilities allow for its mass deployment for multipoint or multi-process monitoring.

### ***7.3 Future Work***

An opto-electronic common instrumentation called Bioprocess Analysis Sensor System (BASS) has been developed, implemented, and verified for measurement of multiple variables (pH, DO, GFP, UV absorption). Though the sensor has been tried and tested in multiple settings, there is still possibility of improvement.

Other variables, apart from the ones discussed in this dissertation, can be measured with this sensor system as well. The common instrumentation for BASS was used for measuring micromolar levels of glucose in a solution. This worked by exciting the glucose binding protein (GBP) with violet light to detect green emissions of the GBP. This glucose measurement sensor is being developed further in the CAST lab.

For pH and DO measurements, more experimental effort is needed to generate a mean calibration equation for both parameters. More data needs to be generated and analyzed with a permutation and combination of multiple patch sensors with the common instrumentation. The temperature coefficient derived in this dissertation for DO is premature and needs to be developed further.

A more efficient GFP calibration and real-time monitoring method needs to be established, to decrease error in the signal detected. The calibration and verification was done only once for this dissertation. Multiple runs need to be conducted in order to authenticate the readings for BASS.

The UV absorption sensor is still quite premature and more work needs to be done to establish a valid procedure to operate the same. For the quantum dots, a more appropriate method for their immobilization needs to be developed. The mechanical design needs to be tried and tested for validation.

## APPENDIX A. BIOLOGICALLY DERIVED MEDICINES ON DEMAND (Bio-MOD)

Figure A.1 presents the Bio-MOD project. The mini bioreactor in the top right corner houses the protein expression process. Buffer and reaction mixes are loaded using a pump. The reactor then expresses the target protein in a span of approximately 4 hours. Once this protein is expressed, it needs to be purified, due to presence of other cell debris along with the protein. Purification is a two-step process involving capturing and polishing of the proteins. After this, a quality control micro-fluidic chip would determine if the derived protein is usable. Once this is validated, the product is available for use in the product vial.

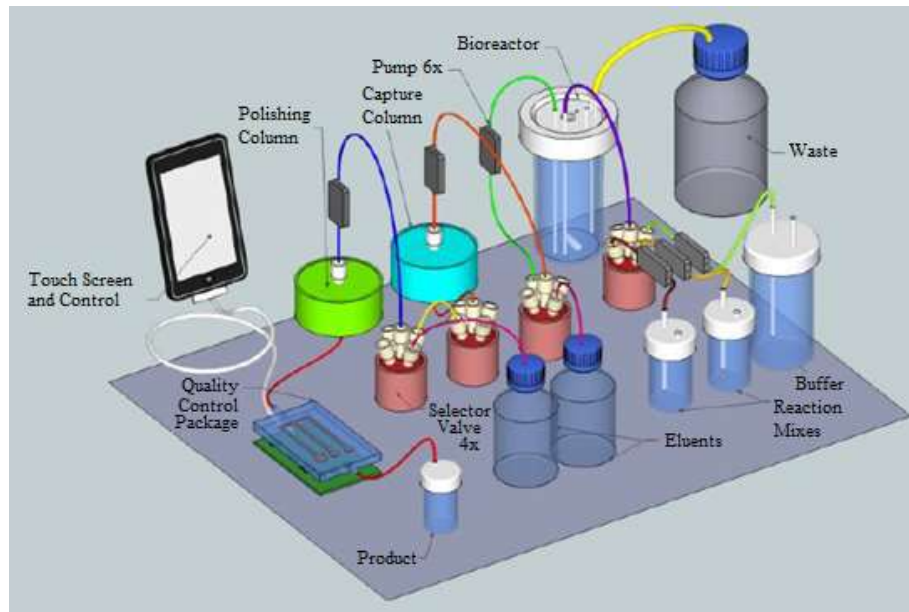


Figure A.1: Illustration of Bio-MOD in a suitcase [8]



The Bio-MOD system consists of 2 parts: protein expression and protein purification. The proposed device will produce, purify, and quantitatively determine the purity of the ready-for-delivery therapeutic protein in a few hours using only a few liters of water (and though the technology is being researched and developed for DARPA, it could eventually be produced for the civilian patient population) [8].

### ***A.1 Cell-free protein expression***

Proteins are synthesized and regulated depending on the functional need of the cell [9]. Complete synthesis of proteins can be summarized as transcription and translation. The DNA contains the ‘source code’ for protein to be expressed. The transcription process enables the decoding of this code to produce messenger RNA (mRNA). The process of translation then synthesizes the protein based on the sequence specified in the mRNA. Figure A.2 is a simplified illustration of the process of transcription and translation ultimately resulting in the expression of target protein.

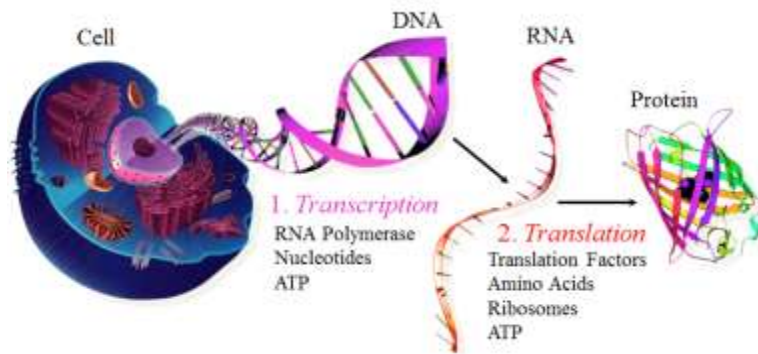


Figure A.2: Transcription and translation resulting in protein expression

Cell-free protein expression is the in-vitro synthesis of protein using translation-compatible extracts of whole cells [9]. To achieve this, the cells are lysed, i.e., they are opened up and, except for the cell wall and nucleus, all other organelles like RNA polymerase, regulatory protein factors, transcription factors, ribosomes, and tRNA, are used as shown in Figure A.3 [45]. This cell-free system is referenced as lysate. When supplemented with cofactors, nucleotides and the specific gene template (genetically engineered DNA for target protein), the lysate can synthesize proteins

of interest in a few hours [9]. The expression team has successfully expressed Streptokinase (SK), Erythropoietin (EPO), GFP, and Granulocyte-colony stimulating factor (G-CSF or GCSF).

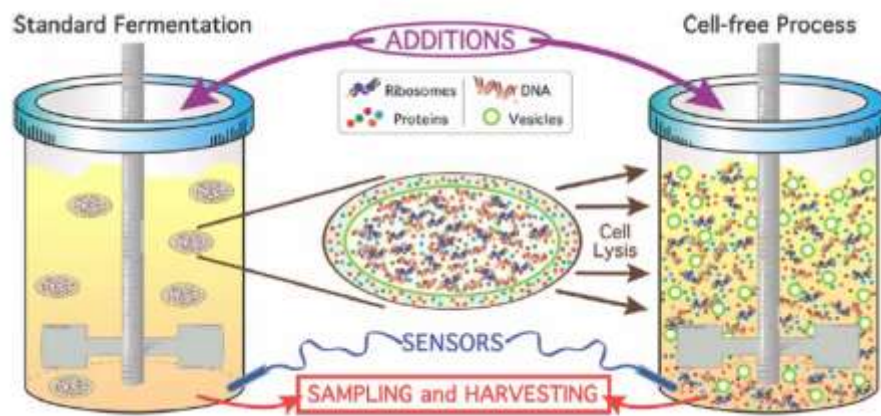


Figure A.3: Illustration of cell-free protein expression [45]

Cell-free protein expression has a number of advantages over traditional in-vitro systems like;

1. Fast synthesis of recombinant proteins without need of cell culture,
2. Enabling protein labeling, as well as expression of proteins that undergo rapid proteolytic degradation by intracellular proteases,
3. Ease of expression of many different proteins simultaneously (e.g., testing protein mutations by expression on a small scale from many different recombinant DNA templates) [9].

## A.2 Protein Purification

Protein purification involves purifying the protein of interest from rest of the cell debris, and crude lysate. Affinity chromatography (also called affinity purification) is used in this case. It makes use of specific binding interactions between different molecules. A particular ligand is chemically immobilized or “coupled” to a solid support so that when a complex mixture (the impure lysate) is passed over the column, those molecules having specific binding affinity to the ligand become bound (the target protein). After the other sample components are washed away, the bound molecule detaches from the support, resulting in its purification from the original sample. [15]. Figure A.4 illustrates the function of a purification column based on affinity chromatography.

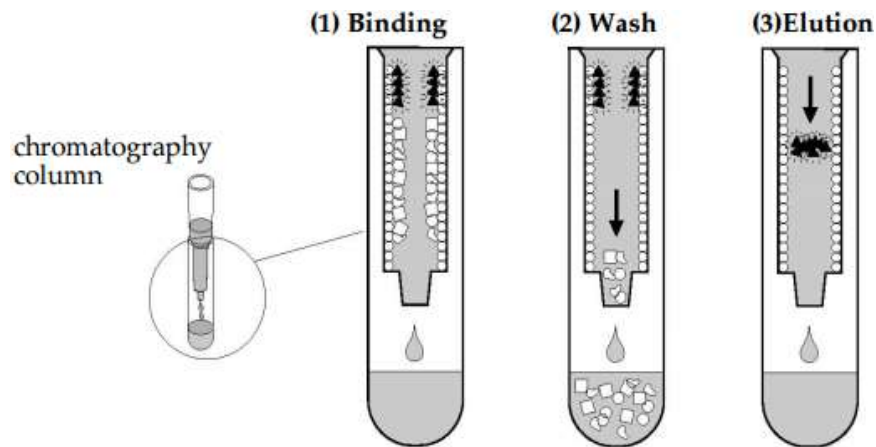


Figure A.4: Procedure for affinity chromatography

## APPENDIX B. SENSOR HARDWARE DESIGN

### *B.1 Micro-controller Functions*

Table B.1 lists the main functions that the micro-controller performs and their corresponding hexadecimal values

Hexadecimal number	Function
20, 24	Measure pH1 and pH 2
21, 25	Measure DO1 and DO2
42	Measure and store offsets
30, 34	Change brightness for blue LEDs 1 and 2 for pH
31, 35	Change brightness for blue LEDs 1 and 2 for DO
32, 36	Change brightness for violet LEDs 1 and 2
33, 37	Change brightness for red LEDs 1 and 2

Table B.1: Micro-controller functions and the hexadecimal values associated with them

### *B.2 Beam Combiner*

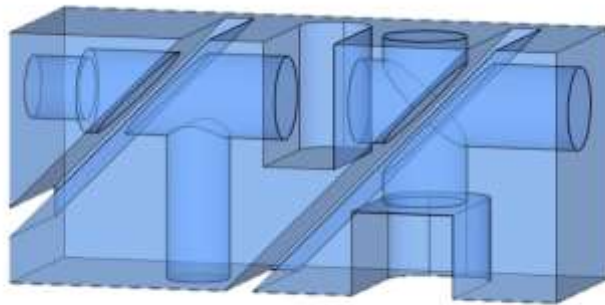


Figure B.1: 3-dimensional diagram of beam combiner

### B.3 Board Schematics

The detailed board schematics for the optical sensor are as shown in Figure B.2. These schematics were drawn in Eagle. The printed circuit board was also designed in Eagle.

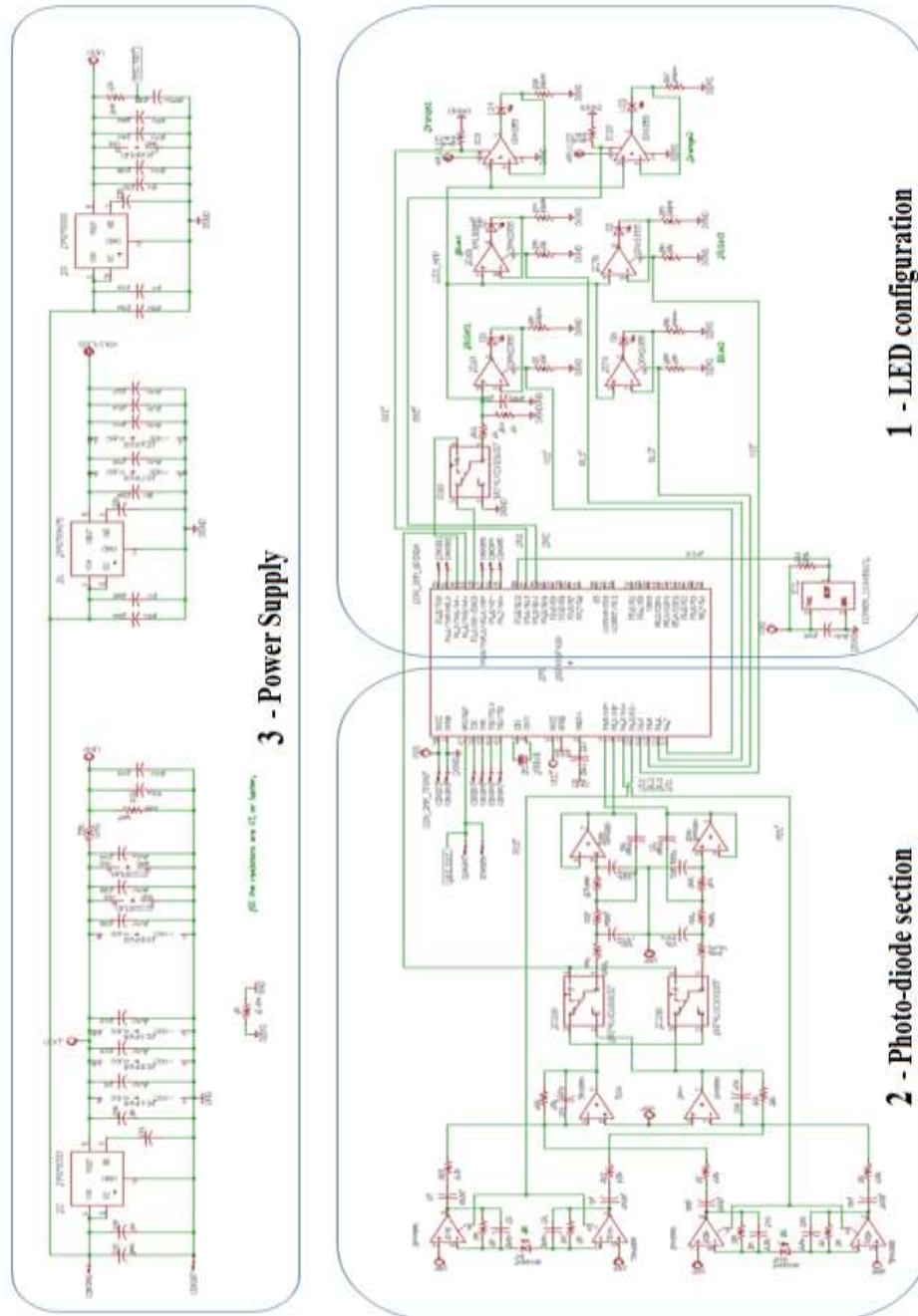


Figure B.2: Board schematics

#### *B.4 Patch Sleeve*

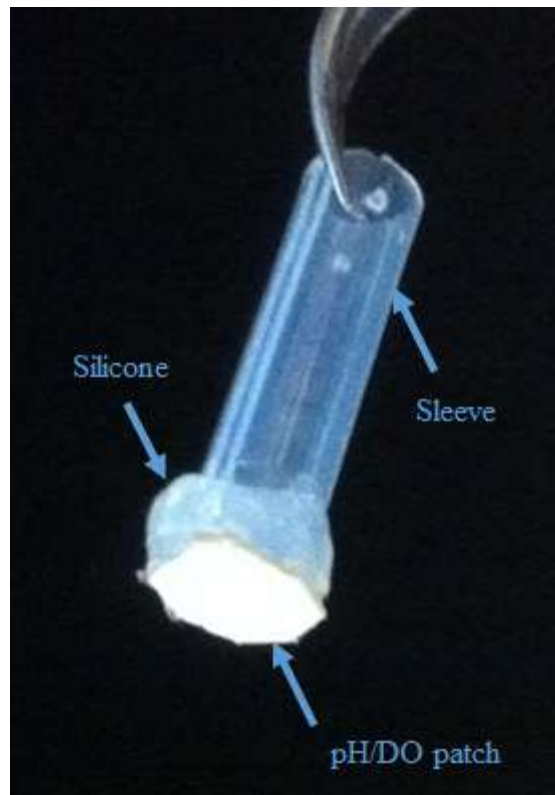
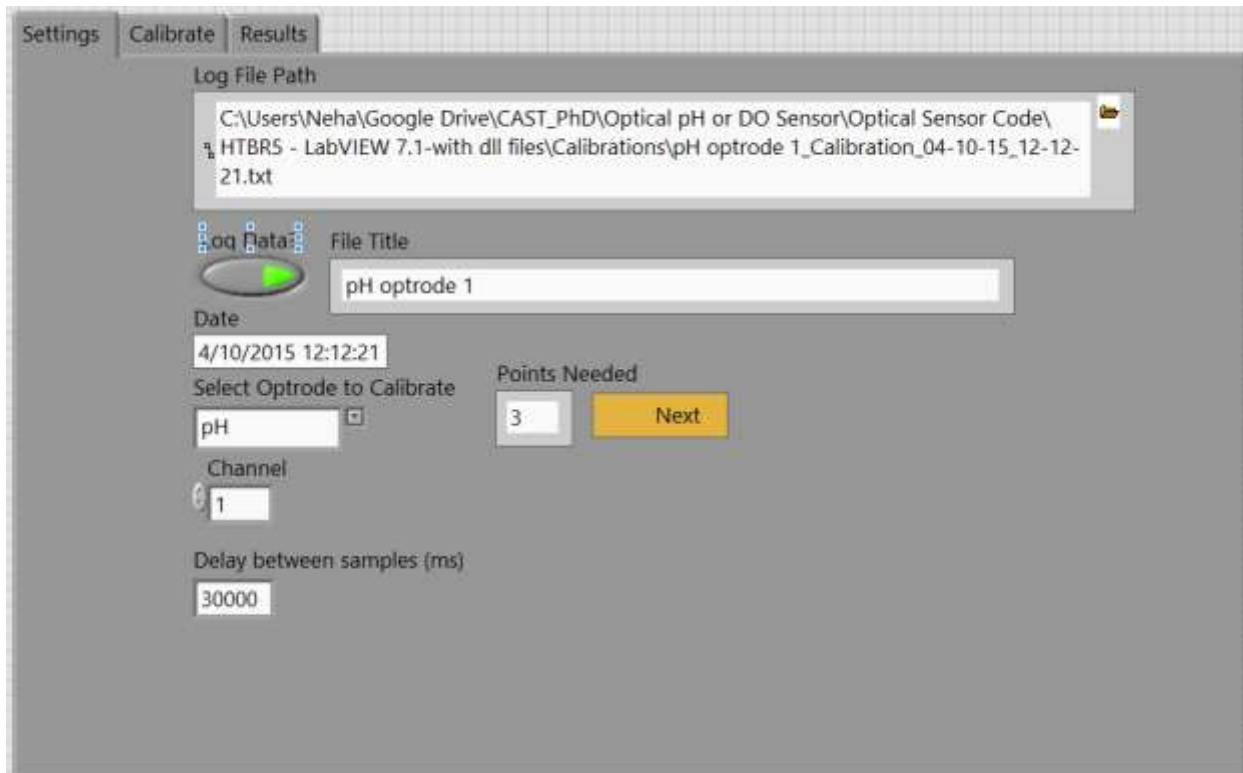


Figure B.3: Patch sleeve

## APPENDIX C. SENSOR SOFTWARE CODE

### *C.1 Calibrate Visual Interface*



The screenshot shows the 'Settings' tab of the 'Calibrate' visual interface. It contains the following fields and controls:

- Log File Path:** A text box containing the path `C:\Users\Neha\Google Drive\CAST_PhD\Optical pH or DO Sensor\Optical Sensor Code\HTBRS - LabVIEW 7.1-with dll files\Calibrations\pH optrode 1_Calibration_04-10-15_12-12-21.txt`.
- File Title:** A text box containing `pH optrode 1`.
- Date:** A date/time field showing `4/10/2015 12:12:21`.
- Select Optrode to Calibrate:** A dropdown menu with `pH` selected.
- Points Needed:** A numeric field with `3` and a yellow `Next` button.
- Channel:** A numeric field with `1`.
- Delay between samples (ms):** A numeric field with `30000`.

Figure C.1: Settings tab on Calibrate VI

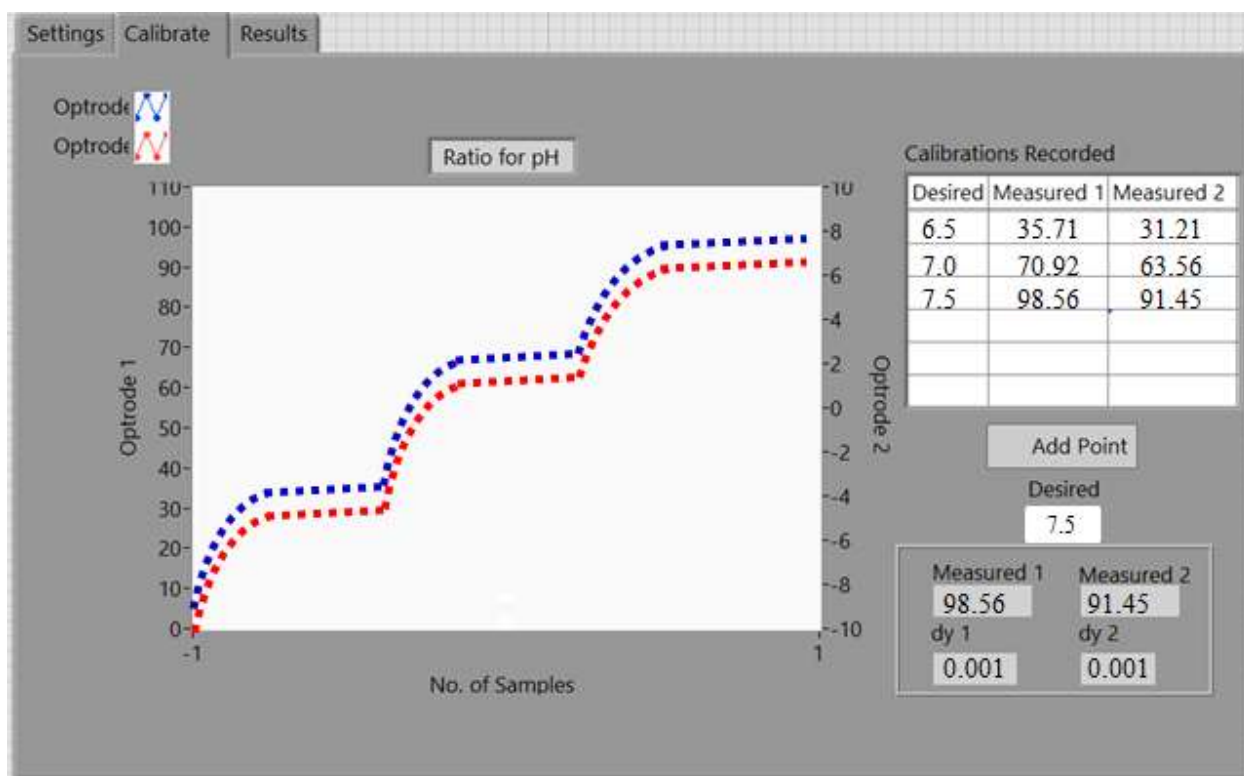


Figure C.2: Calibrate tab on Calibration VI



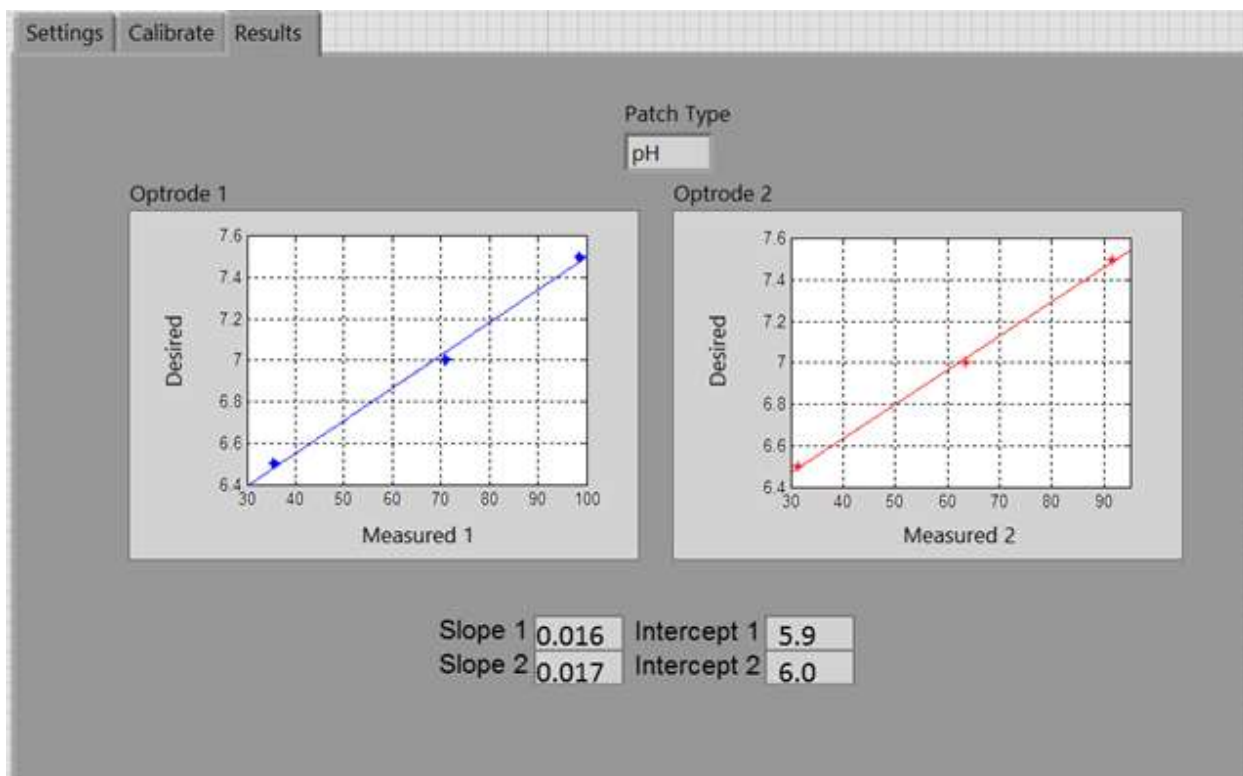


Figure C.3: Results tab on Calibration VI

## C.2 System Interpretation and Data Logging Software (SIDL)

### C.2.1 pH and DO measurements:

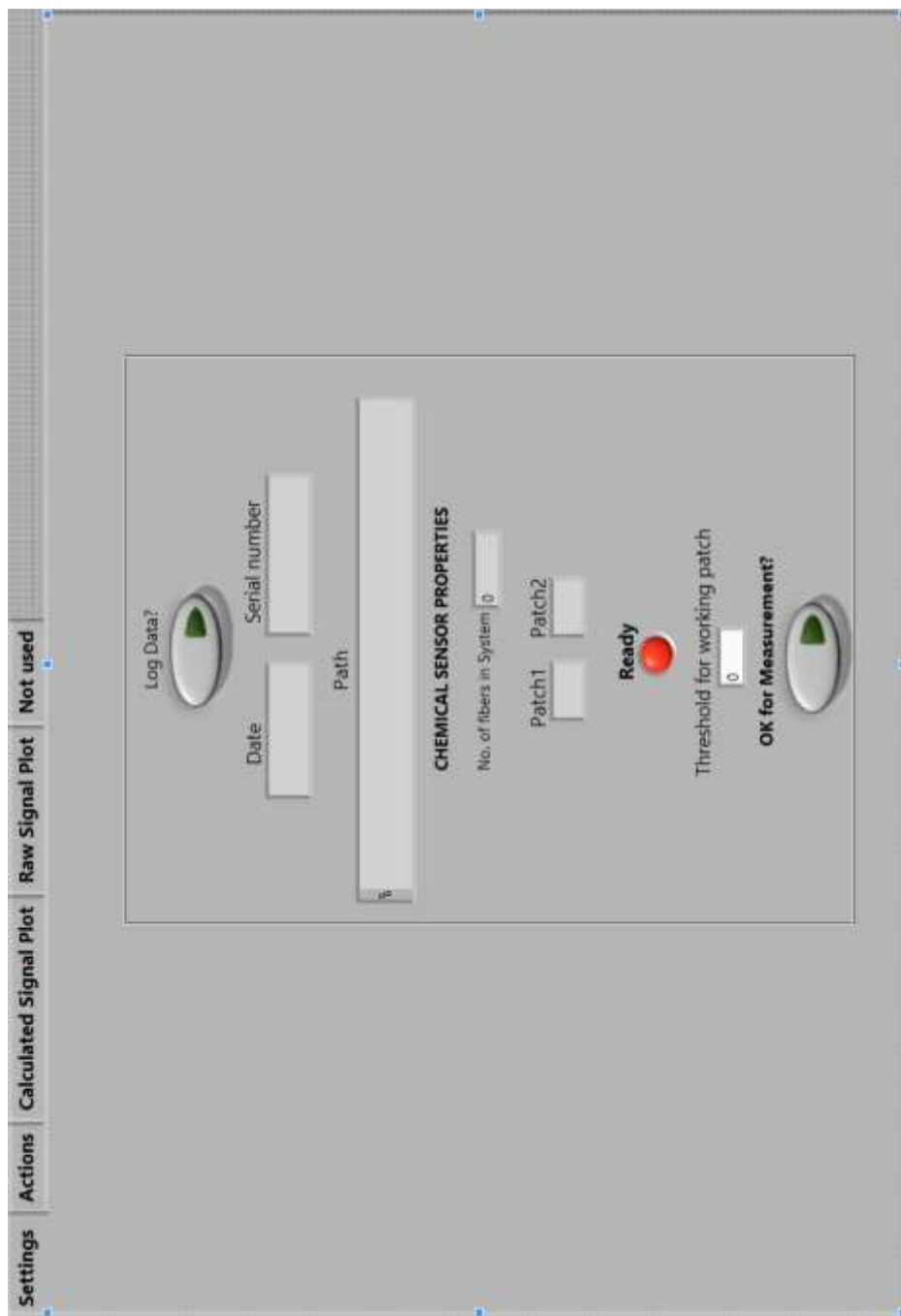


Figure C.4: Settings tab on SIDL VI

Settings

Actions

Calculated Signal Plot

Raw Signal Plot

Not used

Optrode 1

Patch 1 Type

pH

Patch 1 Condition

Patch OK

Measure raw pH 1/DO 1

Measurements 1 (raw)

0	Blue IP
0	Blue QD
0	Violet IP
0	Violet QD

Slope 1

3.02

Intercept 1

6.51

pH 1

0

Optrode 2

Patch 2 Type

DO

Patch 2 Condition

Patch OK

Measure raw pH 2/ DO 2

Measurements 2 (raw)

0	Blue IP
0	Blue QD
0	Red IP
0	Red QD

Blue Phase 2

0.0

Red Phase 2

NaN

Phase Difference 2

NaN

Phase Diff Offset 2

0.1

DO 2 Calibration Code

174511536886

A 2

11.53

B 2

68.86

TanPhi0

1.745

% DO 2 Concentration

NaN

Channel

1

Single Fiber System

Delay between samples (ms)

0

Measure continuously

Figure C.5: Actions tab on SIDL VI

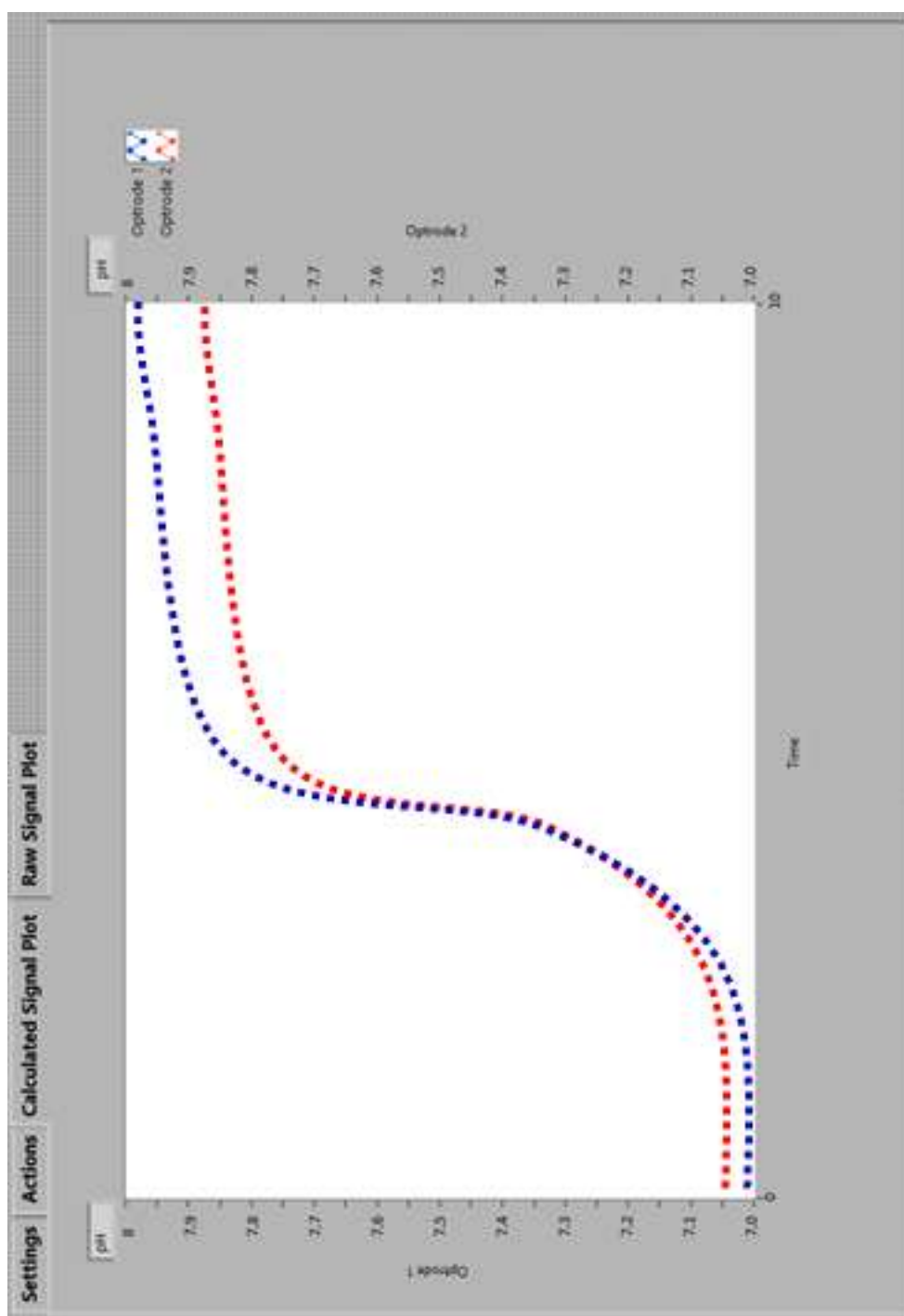


Figure C.6: Calculated Signal tab on SIDL VI

## C.2.2 GFP Rate Analysis VI

The screenshot shows the 'Data' tab of the GFP Rate Analysis VI. The interface is divided into three main sections. On the left, there is a 'Log Data?' section with a green arrow button, a 'Date' field, a 'Serial number' field, and a 'Path' field. Below these is a 'Ready' indicator with a red dot and a 'OK for Measurement?' button with a green arrow. The middle section is for 'Optrode 1', featuring a 'Sensor 1 Type' dropdown, a 'Measure raw GFP 1' button, and a 'Measurements 1 (raw)' table with four rows of input fields. The right section is for 'Optrode 2', featuring a 'Sensor 2 Type' dropdown, a 'Measure raw GFP 2' button, and a 'Measurements 2' table with four rows of input fields.

Figure C.7: Data tab on GFP VI



Figure C.8: Calculated Signal tab on GFP VI

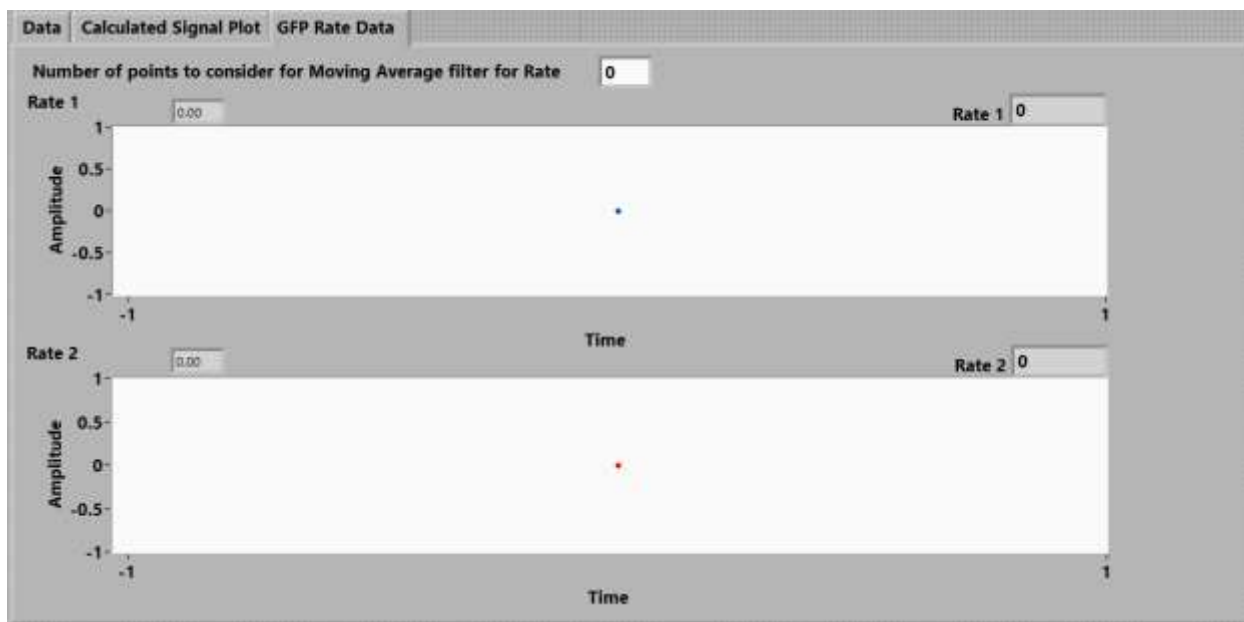


Figure C.9: GFP data rate tab on GFP VI

## APPENDIX D. MATLAB CODE FOR GFP DATA PROCESSING

### D.1 GFP Fixed Length Extension Model

```
% Code for GFP-FLE model
% Code developed by Neha Sardesai
% 8 April 2015

clc; clear all;
l = 0:0.01:50; % mm
conc = 0.500; % micro-gm/micro-l
epsilon = 0.021; % mm2/mole
Q = 0.77; % Quantum yield
rad = 1; % 1 mm
Iex = 10.^(-conc.*l.*epsilon); % Excitation
Iem = Q.*Iex.*(sqrt(l.^2 + rad.^2) - l)./(2.*sqrt(l.^2 + rad.^2)); % Emission
figure; plot(l, Iex, l, Iem, 'LineWidth', 2);
xlabel('Length'); ylabel('I_{em}'); grid on;

L = 0.1; n = 1:100;
h1 = L: 0.01: sqrt(L.^2 + (rad.^2 + (L./sqrt(3)).^2).^2);
R1 = sqrt(rad.^2 + h1.^2);
s1 = 0:rad/(numel(R1)-1):rad; s2 = -fliplr(s1); S = horzcat(s2, s1);
for i = 1:numel(n)
    h(i,:) = n(i).*h1;
    R(i,:) = sqrt(rad.^2 + h(i,:).^2);
    len(i,:) = ((R(i,.)-h(i,))./(R(i,)));
    Iems1(i,:) = Q.* 10.^(-conc.*n(i).*L.*epsilon).*((R(i,.)-
h(i,))./(2.*R(i,)));
end

Iem_top = sum(Iems1); Iem_bottom = fliplr(Iem_top); Iem_total =
horzcat(Iem_bottom, Iem_top); Iem_top(1)
```

```

figure; plot(s1, Iems1(1,:), 'LineWidth', 2); xlabel('Length');
ylabel('I_{em} per slice'); grid on;
figure; plot(s1, Iems1, 'LineWidth', 2); xlabel('Length'); ylabel('I_{em} per
slice'); grid on;
figure; plot(S, Iem_total, 'LineWidth', 2); xlabel('Length along fiber
(mm)'); ylabel('I_{em}'); grid on;

```



## D.2 GFP Signal Processing using Digital Filters

```
% Code for Filtered Rate Analysis
% Code developed by Neha Sardesai
% 10 September 2015

% Get Data
clc; clear all;
file = 'IdealGFP_Data'; Data = xlsread(file); time = Data(:,3); Ideal =
Data(:,6); Rate = Data(:,8);
file1 = 'GFPrun5_FilteredRate';
figure;
[AX,H1,H2] = plotyy(time, Ideal, time, Rate); grid on;
set(AX(1),'YLim',[0 70]); set(AX(1),'YTick',[0:10:70]);
set(AX(2),'YLim',[0 2]); set(AX(2),'YTick',[0:0.2:2]);
xlabel('Time (hours)','fontsize',12,'fontweight','b'); ylabel('Concentration
(\mug/ml)','fontsize',12,'fontweight','b');
set(AX(1),'fontsize',12,'fontweight','b');
set(AX(2),'fontsize',12,'fontweight','b');
set(get(AX(2),'Ylabel'),'string','Rate','fontsize',12,'fontweight','b')

%Butterworth Filter
[b, a] = butter(3, 0.06, 'low');
Butter_Ideal = filter(b, a, Ideal);

%Hamming Window
bb = fir1(100, 0.06);
Hamming_Ideal = filter(bb, 1, Ideal);
figure; plot(time, Ideal, time, Hamming_Ideal, 'LineWidth', 2); grid on;
title('Hamming');

%Delay Correction
for i = 1: (numel(Ideal) - 11)
    Ideal_B_corrected(i) = Butter_Ideal(i+11);
end
```

```

for i = 1: (numel(Ideal) - 50)
    Ideal_H_corrected(i) = Hamming_Ideal(i+50);
end

sheet = 1; xlrangel = 'A1'; xlrangle2 = 'B1';
xlswrite(file1, Ideal_B_corrected', sheet, xlrangel);
xlswrite(file1, Ideal_H_corrected', sheet, xlrangle2);

Data1 = xlsread(file1);
fr_b = Data1(:, 4); fr_h = Data1(:, 5);

figure; plot(time, Ideal, time, Butter_Ideal, 'LineWidth', 2); grid on;
figure; plot(1:numel(fr_b), fr_b, 1:numel(Ideal), Ideal, 'LineWidth', 2);
grid on;
figure; plot(time_OptS, fr_h, time_OptS, FR, 'LineWidth', 2); grid on;
figure; plot(time_OptS, fr_h, time_OptS, fr_b, 'LineWidth', 2); grid on;
figure;
[AX,H1,H2] = plotyy(time(1:131), Ideal_H_corrected, time(1:170), fr_h); grid
on;
set(AX(1), 'YLim', [0 70]); set(AX(1), 'YTick', [0:10:70]);
set(AX(2), 'YLim', [-0.1 2]); set(AX(2), 'YTick', [-0.1:0.5:2]);
xlabel('Time (hours)', 'fontsize', 12, 'fontweight', 'b'); ylabel('Concentration
(\mug/ml)', 'fontsize', 12, 'fontweight', 'b');
set(AX(1), 'fontsize', 12, 'fontweight', 'b');
set(AX(2), 'fontsize', 12, 'fontweight', 'b');
set(get(AX(2), 'Ylabel'), 'string', 'Rate', 'fontsize', 12, 'fontweight', 'b')

```

### D.3 GFP Purification Monitoring

```
% Calculate area under curve for Purification Automation
% Code written by Neha Sardesai
% 1 September 2015

clc; clear all;
file = 'Run2_GFP'; sheet = 'Sheet1';
Data = xlsread(file, sheet); [r, c] = size(Data);
time = Data(:,1); GFP1 = Data(:, 7); GFP2 = Data(:, 6);
GFP2_2 = 2.1.*GFP2;
GFP1norm = GFP1./max(GFP2_2); GFP2norm = 2.1*GFP2./max(GFP2_2);

figure; plot(time, GFP1, time, GFP2, 'LineWidth', 2); grid on;
figure; plot(time, GFP1norm, time, GFP2norm, 'LineWidth', 2); grid on;

upstream = trapz(GFP1norm(1:numel(time)))
downstream = trapz(GFP2norm(1:numel(time)))
```

## Chapter 8. BIBLIOGRAPHY

- [1] A. Gupta and G. Rao, "A study of oxygen transfer in shake flasks using a non-invasive oxygen sensor," *Biotechnology and Bioengineering*, vol. 84, no. 3, pp. 351-358, 2003.
- [2] X. Ge, Y. Kostov, L. Tolosa and G. Rao, "Study on low-cost calibration-free pH sensing with disposable optical sensors," *Analytica Chimica Acta*, vol. 734, pp. 79-87, 2012.
- [3] H. R. Kermis, Y. Kostov, P. Harms and G. Rao, "Dual Excitation Ratiometric Fluorescent pH Sensor for Noninvasive Bioprocess Monitoring: Development and Application," *Biotechnology Progress*, vol. 18, no. 5, pp. 1047-053, 2002.
- [4] D. I. C. Wang, "Sensors for Bioprocess Monitoring and Control," in *Bioproducts and Bioprocesses 2*, Springer, 1993.
- [5] N. Sardesai, G. Rao and Y. Kostov, "Versatile common instrumentation for optical detection of pH and dissolved oxygen," *Review of Scientific Instruments*, vol. 86, no. 7, 2015.
- [6] M. Pohlscheidt, . S. Charaniya, C. Bork, M. Jenzsch, T. L. Noetzel and A. Luebbert, "Part V: Process Analytical Technologies (PAT)," in *Upstream Industrial Biotechnology: Equipment, Process Design, Sensing, Control, and cGMP Operations, Volume 2*, John Wiley & Sons, Inc., 2013, pp. 1471-1491.
- [7] Y. Kostov, P. Harms, L. Randers-Eichhorn and G. Rao, "Low-cost microbioreactor for high-throughput bioprocessing," *Biotechnology and Bioengineering*, vol. 72, no. 3, pp. 346-352, Feb 2001.
- [8] Univeristy of Maryland Baltimore County, Ohio State University, Thermo Scientific Inc., Pfizer Inc., Latham BioPharm Group Inc., "Casting biologics on demand," June 2015.
- [9] ThermoFisher Scientific, "Overview of protein expression," 2016. [Online]. Available: <https://www.thermofisher.com/us/en/home/life-science/protein-biology/protein-biology-learning-center/protein-biology-resource-library/pierce-protein-methods/overview-protein-expression-systems.html>. [Accessed 23 February 2016].
- [10] C. Challener, "Improving PAT for Biologics with Online Spectroscopy and Multivariate Data Analysis," *BioPharm International*, vol. 27, no. 12, 2014.
- [11] W. Whitford and C. Julien , "Analytical Technology and PAT," *Bioprocess International*, 2007.
- [12] N. Sardesai, G. Rao and Y. Kostov, "Universal optical platform for monitoring of bioprocess variables," in *SPIE Sensing Technology+ Applications*, Baltimore, 2015.
- [13] D. G. R. D. Y. K. Neha Sardesai, "Versatile platform for optical detection of pH and dissolved oxygen," *Review of Scientific Intruments* , vol. 86, no. 7, 2015.
- [14] M. Zimmer, *Illuminating Disease: An Introduction to Green Fluorescent Proteins*, Oxford University Press, January 13, 2015.
- [15] ThermoFisher Scientific, "Overview of Affinity Purification," [Online]. Available: <https://www.thermofisher.com/us/en/home/life-science/protein-biology/protein-biology->

- learning-center/protein-biology-resource-library/pierce-protein-methods/overview-affinity-purification.html. [Accessed 23 February 2016].
- [16] T. Owen, Fundamentals of UV-visible spectroscopy: A Primer, Hewlett-Packard, 1996.
  - [17] Walker, John M; Raply, Ralph;, Molecular Biology and Biotechnology, The Royal Society of Chemistry, 2009.
  - [18] R. G. L. J. T. L. Lam H, "Dual Optical Sensor for Oxygen and Temperature Based on the Combination of Time Domain and Frequency Domain Techniques," *Talanta.*, vol. 84, no. 1, pp. 65-70, 2011.
  - [19] C. Lu, C. R. Abano, W. E. Bentley and G. Rao, "Differential rates of gene expression monitored by green fluorescent protein," *Biotechnology and Bioengineering*, vol. 79, no. 4, pp. 429-437, 2002.
  - [20] J. R. Lakowicz, Principles of Fluorescence Spectroscopy, Springer US, 2006, pp. 277-330.
  - [21] G. Rao, Y. Kostov, H. Kermis and P. Harms, "Fluorescent dye comprising 6-methacryloyl-8-hydroxy-1,3-pyrene disulfonic acid for use in systems and methods which non-invasively and continuously monitor pH". USA Patent 10/609,720, 2005.
  - [22] X. Wang and O. S. Wolfbeis, "Optical methods for sensing and imaging oxygen: materials, spectroscopies, and applications," *Chemical Society Reviews*, vol. 43, no. 10, pp. 3666-3761, 2014.
  - [23] R. Carswell and A. R. Khoie, "Optical oxygen sensor based on RUDPP fluorescence quenching," in *Proceedings of the SPIE - The International Society for Optical Engineering*, 1996.
  - [24] C. L. Amick, *Fluorescent Lighting Manual*, McGraw-Hill Book Company, 1942.
  - [25] M. L. Meade, Lock-in Amplifiers: Principles and Applications., Peter Peregrinus Ltd on behalf of Institution of Electrical Engineers, 1983.
  - [26] S. A. L. L. E. F. P. T. Ö. V. K. K. Fu S, "Generalized lock-in amplifier for precision measurement of high frequency signals," *Review of Scientific Instruments*, vol. 84, no. 11, 2013.
  - [27] J. N. Miller, "Correction of excitation and emission spectra," in *Standards in Fluorescence Spectrometry, volume 2 of Techniques in Visible and Ultraviolet Spectrometry*, Netherlands, Springer, 1981, pp. 49-67.
  - [28] A. I. Ekimov and A. A. Onushchenko, "Quantum size effect in three dimensional microscopic semiconductor crystals," *JETP Lett.*, vol. 34, no. 6, p. 345–349, 1981.
  - [29] C.-P. Huang, Y.-K. Li and T.-M. Chen, "A highly sensitive system for urea detection by using CdSe/ZnS core-shell quantum dots," *Biosensors and Bioelectronics*, vol. 22, p. 1835–1838, 2007.
  - [30] "CdSeS/ZnS alloyed quantum dots," Sigma Aldrich.
  - [31] *BPW34S Si-PIN photodiode*, Osram opto Semiconductors.
  - [32] J. R. Lakowicz, Principles of Fluorescence Spectroscopy, Springer, 2006.

- [33] J. E. Noble and M. J. A. Bailey, "Quantitation of Protein," in *Guide to Protein Purification*, Elsevier Inc., 2009, pp. 93-96.
- [34] *2000 $\mu$ m with 1 Fiber, Optical Grade Plastic Light Guide Datasheet*, Edmund Optics.
- [35] "Microscopyu.com," 2015. [Online]. Available: <https://www.microscopyu.com/articles/livecellimaging/fpintro.html>. [Accessed 16 May 2015].
- [36] ThermoFisher Scientific, "HisPur™ Cobalt Chromatography Cartridges, 1 mL, catalog number - 90093".
- [37] Heftmann, E., *Chromatography: Fundamentals and applications of chromatography and related differential migration methods - Part A: Fundamentals and techniques*, Elsevier Inc., 2004.
- [38] B. J. Olson and J. Markwell, "Assays for Determination of Protein Concentration," in *Current Protocols in Protein Science*, John Wiley and Sons, Inc., 2007.
- [39] J. Ruzicka and E. H. Hansen, *Flow Injection Analysis*, John Wiley and Sons, 1988.
- [40] J. B. Murphy and M. W. Kies, "Note on spectrophotometric determination of proteins in dilute solutions," *Biochimica et Biophysica Acta*, vol. 45, pp. 382-384, 1960.
- [41] H. Edelhoch, "Spectroscopic Determination of Tryptophan and Tyrosine in Proteins," in *Biochemistry*, 1967, ACS Publications, pp. 1948-1954.
- [42] G. Wider and L. Dreier, "Measuring protein concentrations by NMR spectroscopy," *American Chemical Society*, vol. 128, no. 8, pp. 2571-2576, 2006.
- [43] E. Layne, "Spectrophotometric and Turbidimetric Methods for Measuring Proteins," in *Methods in Enzymology* 3, 1957, pp. 447-455.
- [44] "Nucleic acid quantitation," Wikipedia, 15 March 2016. [Online]. Available: [https://en.wikipedia.org/wiki/Nucleic\\_acid\\_quantitation](https://en.wikipedia.org/wiki/Nucleic_acid_quantitation).
- [45] J. R. Swartz, "Transforming biochemical engineering with cell-free biology," *AIChE*, vol. 58, no. 1, pp. 5-13, 2012.

